12-2019

Photosystem I Incorporation into Metal Organic Frameworks for Advanced Bio-hybrid Photoactive Materials

Tyler Bennett
University of Tennessee

Recommended Citation

Bennett, Tyler, "Photosystem I Incorporation into Metal Organic Frameworks for Advanced Bio-hybrid Photoactive Materials. " PhD diss., University of Tennessee, 2019.
https://trace.tennessee.edu/utk_graddiss/5955

To the Graduate Council:

I am submitting herewith a dissertation written by Tyler Bennett entitled "Photosystem I Incorporation into Metal Organic Frameworks for Advanced Bio-hybrid Photoactive Materials." I have examined the final electronic copy of this dissertation for form and content and recommend that it be accepted in partial fulfillment of the requirements for the degree of Doctor of Philosophy, with a major in Chemical Engineering.

Bamin Khomami, Major Professor

We have read this dissertation and recommend its acceptance:

Dibyendu Mukherjee, Paul Frymier, Craig Barnes

Accepted for the Council:

Dixie L. Thompson

Vice Provost and Dean of the Graduate School

(Original signatures are on file with official student records.)

Embedding and Photoactivating Photosystem I in Unique Organic-Inorganic Matrices

A Dissertation Presented for the
Doctor of Philosophy
Degree
The University of Tennessee, Knoxville

Tyler Hamilton Bennett
December 2019

ACKNOWLEDGEMENTS

There are truly too many people to thank to fit on this page. Throughout this long journey there have been many voices of encouragement and guidance. I believe that my greatest accomplishment here is by no means the work you are now reading, but rather it is having learned to fail in every sense of the word and no longer be destroyed by the fear of that failure. And so I have found myself free to pursue in joy all the wonders of discovery. I cannot thank enough Prof. Bamin Khomami and Prof. Dibyendu Mukheree for the time when I had given up on myself, and they picked me up with compassion, grace, mercy, and vision. I have been blessed and shaped by their insight, creativity, passion, and ambition.

A great thanks to my labmates Dr. Hanieh Niroomand, Dr. Sheng Hu, Dr. Ali Davari, Erick Ribeiro, and especially Ravi Pamu, who has become like a brother to me. Additionally, I would thank all collaborating undergraduates along the way who worked beside me, including Hannah Haines, Neil Brown, Kiman Park, and Madison Sherrod.

Special thanks to Dr. John Dunlap (Advanced Microscopy and Imaging Center at the University of Tennessee, Knoxville) and Michael Vaughn (BioLogic USA) for their scientific and technical assistance. I gratefully acknowledge the financial support provided by the University of Tennessee Sustainable Energy Education and Research Center (SEERC) that made this work possible.

Above all others who walk this earth, I am most grateful for my beloved wife Morgan, who has seen my worst and loved me best. I could not have finished this race without her and her continual help and encouragement.

ABSTRACT

The transmembrane photosynthetic protein complex Photosystem I (PSI) possesses remarkable photoactive electrochemical properties which make it highly sought after for incorporation into biohybrid photovoltaic devices. In the pursuit of all such endeavors, three main factors must always be kept in view: understanding the direct redox transfer steps, three-dimensional coordination and stabilization of PSI aggregates, and interfacial connectivity with conductive pathways. This thesis presents steps taken to further these three concepts, contributing to the research community what may help utilize the great potential of PSI.

First is presented detailed electrochemical investigations into the role of dissolved O_2 as a catalyst for methyl viologen (MV) to scavenge photoactivated electrons from PSI monolayers. These measurements, apart from demonstrating the ability of dissolved O_2 in the electrolyte medium to act as a direct electron scavenger, also reveal that the dissolved O_2 forms a complex intermediate species with MV which plays the essential role in mediating redox pathways for unidirectional electron transfer processes.

Second, a novel 3D architecture is described to organize and stabilize PSI in the myriad of harsh conditions in which it needs to function. PSI is encapsulated in a highly stable nanoporous metal–organic framework, ZIF-8, denoted here as PSI@ZIF-8. The ZIF-8 framework provides a unique scaffold with a robust confining environment for PSI while protecting its precisely coordinated chlorophyll networks from denaturing agents. Pump–probe spectroscopy confirms the photoactivity of the PSI@ZIF-8 composites even after exposure to denaturing agents and organic solvents. This work provides greater fundamental understanding of confinement effects on pigment networks, while significantly broadening the potential working environments for PSI-integrated bio-hybrid materials.

Finally, inspired by our successful encapsulation of PSI@ZIF-8, cations from this precursor are used to form charge transfer complexes with the extremely strong organic electron acceptor TCNQ. This PSI-Zn-H_2mim-TCNQ charge transfer salt complex was dropcast on ITO as dense films. Through voltammetric cycling and the exchange of Zn^{2+} and H_2mim^+ cations, electrochemical annealing of the film increases electrical connectivity and electron conductivity that enabled PSI embedded charge transfer film to generate an order of magnitude greater photocurrents.

TABLE OF CONTENTS

LIST OF TABLES

LIST OF FIGURES

CHAPTER 1

INTRODUCTION

1.1 Photosynthesis overview

Photosynthesis is the process by which plants, algae, and certain bacteria convert sunlight into usable chemical energy. This stored energy takes the form of carbohydrates, which are then further used to power the formation of every biological molecule, protein, and structure, as well as fuel the motion of every living thing. While certain bacteria employ anaerobic photosynthesis with an alternate electron source, such as H_2S,[1] the vast majority of photosynthetic activity is aerobic in nature, releasing the oxygen necessary for all other respiratory animals and organisms to function. The substance of all carbohydrates and organic matter comes from the combination of CO_2 and H_2O.[2]

$$CO_2 + H_2O \longrightarrow CH_2O + O_2$$

In order for this net reaction to take place, energy must be invested to first split both reactants for the subsequent combination.[3]

$$2H_2O \longrightarrow 4H^+ + 4e^- + O_2$$

$$CO_2 + 4H^+ + 4e^- \longrightarrow CH_2O + O_2$$

The water splitting is performed by Photosystem II as a direct photochemical reaction. That is, light must be continuously absorbed to provide energy at the time of reaction. In contrast, carbon dioxide reduction is part of the light-independent Calvin cycle (dark reactions) that may occur at any time within the photosynthetic organism because it is directly catalyzed by precursor molecules (namely, ATP and NADPH). Specifically, NADPH is formed when the other light-activated photosynthetic protein complex, Photosystem I (PSI) absorbs sunlight and pumps electrons for the reduction of $NADP^+$ to NADPH. It is this light-harvesting complex, PSI, on which this present thesis is focused in an effort to explore its fundamental electron shuttling properties as well as its incorporation into suitable organic/inorganic frameworks that can enable efficient charge transport interfaces in diverse engineering materials for fabricating photo anodes and photoelectrochemical devices.

1.2 Structure and function of Photosystem I

Within photosynthetic organisms, both Photosystem I (PSI) and Photosystem II (PSII) are housed within the thylakoid membrane.[4-5] They work in tandem to power the cascading reactions of photosynthesis. In cyanobacteria (sometimes referred to as blue-green algae), the thylakoid membranes coordinate and orient these photosystems to establish transmembrane potentials that drive redox reactions and transport. PSI found in the cyanobacteria *Thermosynechococcus Elongatus* weighs 1068 kDa and occurs in the trimeric form[6-7] pictured in Figure 1.1.

Each of the three monomers is a supramolecular complex structure organized with 12 protein chain subunits, which coordinate 96 chlorophylls, 22 carotenoids, 2 phylloquinones, and 3 Fe_4S_4 clusters.[6] Chlorophyll is the primary light absorbing molecule, which gives rise to the characteristic green color of leaves due to strong absorption in the blue (440 nm) and red (680 nm) regions. This broad visible light absorption (Figure 1.2) allows PSI to be photoactive over 53% of the solar spectrum.

The aforementioned chlorophyll network uses an incoherent energy transfer mechanism to funnel energy from all absorbed light to a special pair of chlorophylls (called P_{700}), which initiate a charge separation process pictured in Figure 1.3. Upon excitation by light, this dimer goes from ground state (E_m = +430 mV vs standard hydrogen electrode, SHE) to an excited state, P_{700}^* (E_m = -1400 mV). The first electron transfer step is to the chlorophyll molecule A_0 (E_m = -1000 mV), then to the phylloquinone A_1 (E_m = -800 mV), and finally to the three iron-sulfur clusters F_X, F_A, and F_B (E_m = -705, -580, and -530 mV respectively). Once the electron has reached the terminal F_B^-, the soluble electron scavenger ferredoxin docks at the stromal side of PSI to accept this electron and oxidize F_B^- back to F_B. To complete this circuit and allow continuous electron transport, a soluble electron donor such as plastocyanin docks at the luminal side to reduce P_{700}^+ (E_m = +490 mV) back to P_{700}.[8-10]

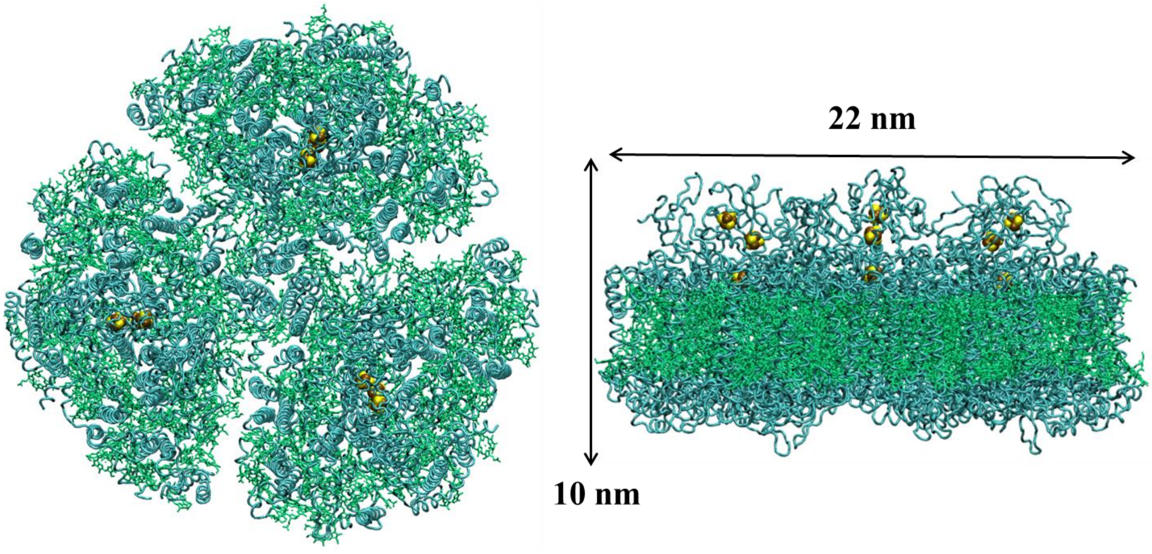

Figure 1.1 A top-down (left) and side (right) view of the trimeric Photosystem I complex found in the cyanobacteria *T. Elongatus.*

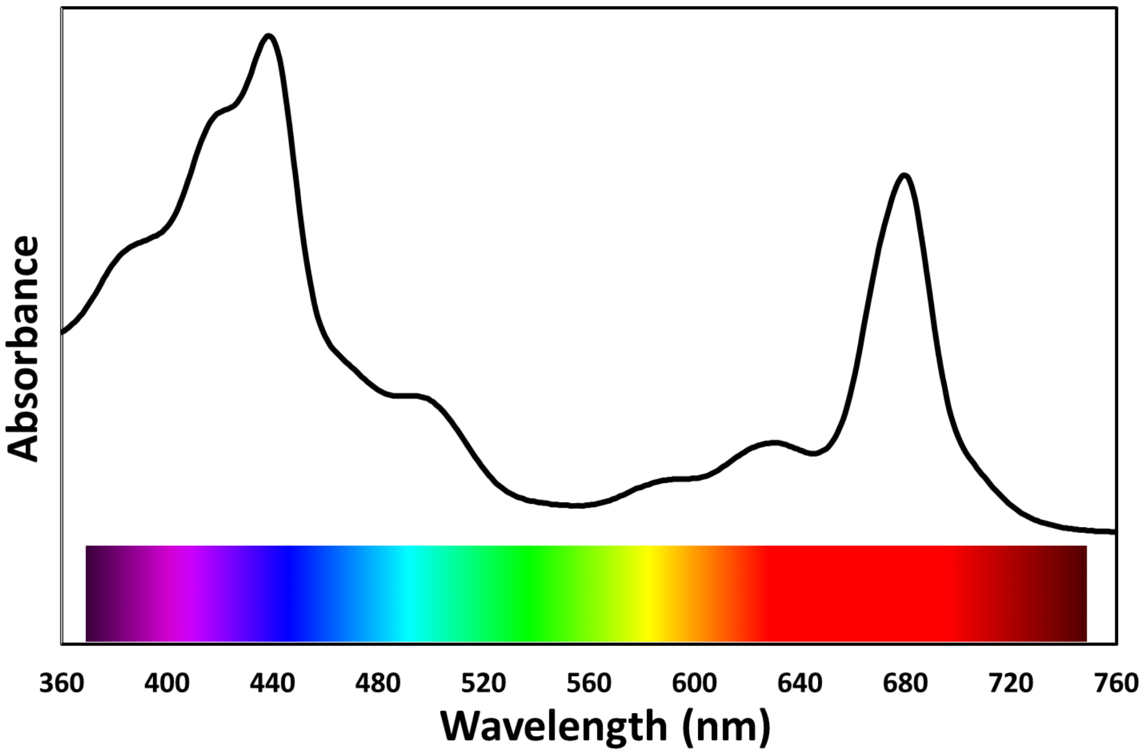

Figure 1.2 Absorption spectrum of the chlorophyll network coordinated in Photosystem I, with peak values at 440 nm and 680 nm.

Several observations about this photoactivated energy transfer process have made PSI an ideal candidate both for fundamental investigations and practical applications in the fabrication of biohybrid devices. As mentioned previously, PSI is light-activated throughout the entirety of the visible spectrum. The conversion of photons absorbed anywhere in the chlorophyll network to the critical charge separation event happens at nearly ~100% quantum efficiency[7] and extremely quickly. In fact the first electron transfer occurs on the femtosecond (10^{-15}) time scale, proceeded by subsequent transfers in picoseconds (10^{-12}), thereby allowing the electron to reach the terminal iron-sulfur clusters finally in nanoseconds (10^{-9}).[11] The terminating Fe-S clusters play an important role in the electron transport chain in stabilizing this charge separation and preventing the electron recombination, thereby leading to a remarkable electron lifetime measured up to milliseconds (10^{-3}).[12]

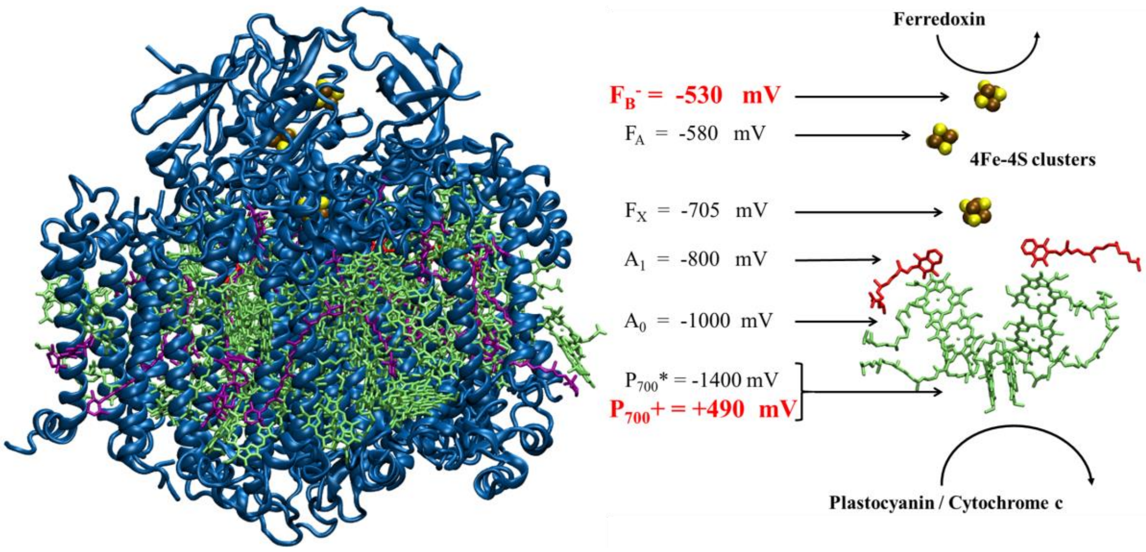

Figure 1.3 On the left, side view one PSI monomer with protein backbone in blue and chlorophyll network in green. On the right, schematic of the embedded electron transfer pathway from the luminal to stromal side. Potentials are vs SHE.

1.3 Photosystem I in biohybrid devices

The robust structural and photoactive electrochemical properties of PSI have drawn extensive interest in incorporating this transmembrane protein complex into a myriad of biohybrid photovoltaic, photocatalytic, or bioelectronic devices.[13-27] While the history of these PSI endeavors is deep and wide, we will be taking a guided look at three of the fundamental concepts that govern such research and are relevant to the scope of the current thesis. These efforts include studies on the direct redox transfer steps, long range coordination and stabilization of PSI aggregates, and interfacial connectivity with conductive pathways.

The first critical step towards producing sustainable photocurrent requires systematic assembly of PSI complexes on specific substrates to enable rapid electron transfer from the lumenal to the stromal side of PSI. A single monolayer of PSI is attached to a conductive substrate and used in a wet cell, where the electrode surface contacts one side of the PSI and a soluble electron donor or scavenger contacts the opposite side. A common attachment method has been PSI monolayers attached to gold electrodes[28-32] through self-assembled monolayer functionalization. To this end, a variety of surfaces have been used in the past, including doped GaAs,[17] carbon nanotubes,[15, 33-34] metal oxide nanowires,[35] or plasmonic nanostructures.[36-38] The protein may stay attached through hydrogen-bonding to various terminal groups (OH, COOH, NH_3) via physisorption, or be covalently bound to site specific chemistry through genetic mutations.[15, 33, 39] While each of these surfaces provides unique conductive or semi-conductive behavior, the critical bottle-neck in regards to the interfacial electron transfer via soluble mediator uptake remains the same, namely the discrete charge transport steps from surface to protein and protein to solution. Therefore, for studying this interaction, a simple construct is often chosen. Systematic and rapid surface assembly of photosynthetic protein complexes, including PSI,[40-44] on alkanethiolate SAM/Au substrates have proven to be a simple and highly reproducible method for creating uniform and dense monolayer of these proteins without denaturing them.[28, 41, 45]

For current to flow through PSI immobilized on electrode surfaces, a soluble mediator must diffuse to, dock on, and exchange electrons with PSI, then diffuse away to be replaced. It is believed that the steric hindrance of that docking and the potential difference of the redox step are the limiting factors that will determine the kinetics of transfer. In the past, numerous studies have constructed PSI substrates in conjunction with electron scavengers such as methyl viologen (MV) in an electrolyte medium to complete the wet cell circuit.[42, 46-48] MV has been the most widely used, in part because of its stability, prolific usage through literature (and thus suitable for comparing other construct factors), well-posed redox potentials, and its supposedly well-understood interaction in PSI electron chain disruption.[49]

A large array of both acceptors and donors have continued to be tested in new concentrations and combinations[32, 47-48, 50] in order to understand and optimize this facet of biohybrid devices. Specifically, one study even investigated 14 different soluble electron donors or scavengers and found that the choice of mediator affected the photocurrent by multiple orders of magnitude.[47] Unfortunately, no definitive pattern emerged by which to predict the suitability of a mediator. While there is a slight trend in behavior over the midpoint potential of the mediator, it has not been the case that the mediator most closely matched to the F_B^- (E_m = -530 mV) or P_{700}^+ (E_m = +490 mV) produced the highest current, nor did the greatest potential difference between PSI and a given sacrificial mediator. Steps towards optimizing the redox transfer both to and from PSI have been taken by several groups, including via integration with naturally tuned biological catalysts such as cytochrome c_6.[51] Additionally, the rational design and synthesis of specifically tuned redox mediator systems has shown great promise.[52]

While on one hand this understanding of fundamental electrochemical interactions must be furthered, large-scale implementation of PSI-based devices also requires large amounts of PSI to be coordinated on the electrode surface. Because of the weak optical absorption of a single PSI monolayer (only 0.34% of incident light at 680 nm)[53] many layers must be deposited to absorb significant light. The simplest of multi-layered PSI constructs consists of merely depositing large amounts of protein in a thick film, which is held together by hydrophobic interactions as the film dries.[54] This technique has been successfully combined with a variety of highly active surfaces including p-doped silicon,[55] and graphene.[23, 56-57] While the photocurrents of such devices have orders of magnitude improvement over monolayers, the currents still fall far short of PSI's large untapped potential and, hence, the need to understand the electron flow within the PSI multilayers becomes apparent.[17]

Rather than rely on the slow diffusion kinetics throughout the multilayer films, groups have increasingly been exploring structures that can provide stability as well as facilitate efficient charge transport. Among these have been mesoporous electrodes,[20] hydrogels,[50] conductive polymers,[58-60] or even combinations of DNA binders.[61] Two primary factors are at play here to explain the further enhancement of photocurrents in these case studies. First is to note that the extraordinary charge separation properties of PSI are due to its uniquely coordinated chlorophyll network, and therefore any disruptions to its structure affect the coherent and incoherent energy transfer.[62] It has been shown that such stabilizing effects on the structure of PSI are greatly beneficial to its function,[63] as also confirmed by our group's previous work incorporating PSI into lipid bilayers[64-65] that mimic the native PSI thylakoid membrane. Secondly, conductive additives allow greater electron flow by creating pathways for long range electron transport that stymies recombination within the PSI network. As research groups attempt to precariously balance between bulk conductivity and sufficient PSI interfacing, there has even been photocurrent produced in entirely dry cells devoid of shuttling mediators.[66]

1.4 Looking toward new materials

Towards this end of increased stabilization, this thesis here presents the concept of incorporating PSI into a unique metal organic framework (MOF). MOFs are rapidly emerging as a new class of materials that comprise highly organized crystalline structures made from inorganic (metal) nodes connected by organic linkers. Such networked structures are tunable with near infinite possible combinations of nodes and linkers. Furthermore, MOF structures are highly permeable with pore sizes ranging from 0.3 to 10 nm[67] and large free volumes (over 90%)[68] and surface areas (over 10,000 m^2/gm).[69] Currently, there exist over 20,000 MOFs that have been characterized,[70] and the field is rapidly growing. Thus far, MOFs have been systematically implemented for gas storage,[71] fluid separations,[72] sensing,[73] catalysis,[74] luminescence,[75] and photovoltaics.[76] Specifically, Zeolitic Imidazolate Framework (ZIF-8) is a MOF structure comprised of zinc (metal node) and 2-methylimidazole (organic linker) that offers 11.4 Å cavities gated by 3.4 Å apertures.[77] With an optical band gap of 5.5 eV (λ = 225 nm)[78] this semiconductor framework is transparent in the visible region (380 nm to 740 nm)[79] which is a key optical property needed for suitable PSI encapsulation to ensure its photochemical functionality. Critically, ZIF-8 is set apart from the vast majority of other MOFs in that can be synthesized in water at room temperature and pH < 11,[80] whereas most MOF synthesis requires organic solvents, high pressure and temperature, or extreme acidic conditions. ZIF-8 is highly stable in a wide range of solvent conditions (aqueous, organic solvents, or high alkalinity),[77] and in temperatures over 200˚ C.[80] Past studies have demonstrated that ZIF-8 has the capacity to lend these harsh environment resistant properties to small proteins embedded inside them, thereby protecting them from denaturation under extreme conditions.[81-83] Specifically, encapsulated enzymes have been shown to retain and, in a small number of cases, even enhance their activities.[84-87] This enhancement is not yet fully understood, but has been attributed to the physical confinement of an active conformation and/or interactions between the active site and the metal nodes of the framework. Fundamental understanding on the effects of such MOF encapsulation on the functional behaviors of large membrane proteins is still an open question. Hence, we report ZIF-8 crystal structures grown via heterogeneous nucleation on PSI acting as the seeding agent, which allows us to encapsulate the photocatalytic protein within the zeolitic structure to create encaged PSI@ZIF-8 composites.

Towards the end of increased PSI interfacing with a redox-active conductive polymer, we propose a new approach which may increase the options for all three of the aforementioned fronts for photocurrent enhancements from PSI constructs, namely through the formation of a TCNQ-based charge transfer salt. TCNQ, or 7,7,8,8-tetracyanoquinodimethane, is well known as an extremely strong organic electron acceptor, with an electron affinity of 2.88 eV,[88] and its anion $TCNQ^-$ is known to rapidly form stable charge transfer salts with almost any cation, whether metallic[89] or organic[90-91] in nature. In addition, it has two favorable redox peaks (-185 and +445 mV vs NHE)[92] for interacting with both the stromal (-530 mV) and lumenal (+490 mV) sides of PSI. The coordination of TCNQ with transition metal cations or organic ligands can form a large number of various morphologies, including coordination polymers,[91] metal-organic frameworks,[93] and crystalline salts.[94] These complexes are almost all insoluble in both polar and nonpolar solvents,[95] thereby lending them the much-desired stability in a variety of environments and applications. Towards this end, they have found applications in the catalysis of electron transfer reactions,[96] as well as electrical, optical, and molecular switching, field emission devices. Specifically, certain organic complexes have high enough electronic conductivities to be considered fully organic metals, such as the well-known TTF-TCNQ salt.[97]

Herein, inspired by our successful encapsulation of PSI in ZIF-8 (PSI@ZIF-8)[98] we report the use of PSI@ZIF-8 composites as starting scaffolding materials to drive the constituent cations (namely, Zn^{2+} or the imidazole ion, H_2mim^+) from ZIF-8 towards subsequent formation of charge transfer complexes with TCNQ. While it has recently been demonstrated that a copper-based MOF can undergo ligand substitution to form CuTCNQ,[99] our work enables a transformation in an aqueous environment amenable to a host of biological materials rather than organic solvent. We demonstrate that the bound PSI remains embedded in the newly coordinated and conductive polymer network, which, in turn, allow significant augmentation in the photocurrent generation. We also show that the aforementioned cations can be reversibly exchanged in aqueous solution via electrochemical treatments to change both the composition and morphology of the TCNQ-based complex, which offers a myriad of future opportunities for successful integration of this unique class of charge transfer salt complexes with biological catalysts and light harvesters.

CHAPTER 2

ELUCIDATING THE ROLE OF METHYL VIOLOGEN AS A SCAVENGER OF PHOTOACTIVATED ELECTRONS FROM PHOTOSYSTEM I UNDER AEROBIC AND ANAEROBIC CONDITIONS

This chapter is based on the submitted paper:

"Elucidating the role of methyl viologen as a scavenger of photoactivated electrons from photosystem I under aerobic and anaerobic conditions" by Tyler Bennett**,** Hanieh Niroomand**,** Ravi Pamu**,** Ilia Ivanov**,** Dibyendu Mukherjee, and Bamin Khomami.

2.1 Introduction

During photosynthesis plants and algae use Photosystem I (PSI), a supra-molecular protein complex,[7] to harness solar energy with 100% quantum efficiency. Previous structural and functional studies of trimeric PSI,[7, 100] apart from characterizing its shape and dimensions (Figure 2.1), have revealed a photo-activated (λ = 680 nm) electron transfer chain. This electron transfer mechanism is mediated by a series of redox reactions initiated at the lumenal (mid-point potential, E_m (P700/ P700+) $\approx$ +0.49 V) and terminated at the stromal side (mid-point potential, E_m (F_A; F_B; F_X) $\approx$ -0.53 V), of the c complex, where the Fe-S clusters are housed. The highly efficient photo electrochemical activity of PSI has resulted in extensive studies[13-14] towards incorporation of PSI into highly efficient hybrid photochemical and electronic devices.[15-17] However, the first critical step towards achieving this goal requires a highly dense and uniform assembly of directionally aligned monolayer of PSI complexes on specific electron donor substrates to enable rapid electron transfer from the lumenal to the stromal side of PSI (Figure 2.1). To this end, in recent years, significant effort has been directed towards directional attachment of single PSI trimers,[39] molecular wiring for electron relay,[30] multi-layered PSI assemblies[17, 101] using genetically incorporated cysteine tags in PSI mutants along with site specific chemistry to covalently bond with Au,[39] maleimide functionalized carbon nano-tubes (CNT)[15, 33] or doped GaAs surfaces.[17] While these approaches are highly effective in directionally immobilizing PSI on various electron donor surfaces, intricate techniques for the synthesis of PSI mutants are required in order to avoid altering the structural and/or functional integrity of the protein. Furthermore, such methods also call for the fabrication of highly specialized and complex nanostructured surfaces. In contrast, in the last several years, systematic and rapid surface assembly of photosynthetic protein complexes (including PSI)[40-44] on alkanethiolate self-assembled monolayer (SAM)/Au substrates have proven to be a simple and highly reproducible method for creating uniform and dense monolayer of these proteins without denaturing them. Specifically, previous studies have demonstrated that OH-terminated alkanethiolate SAM substrates facilitate directional attachment of PSI with its stromal

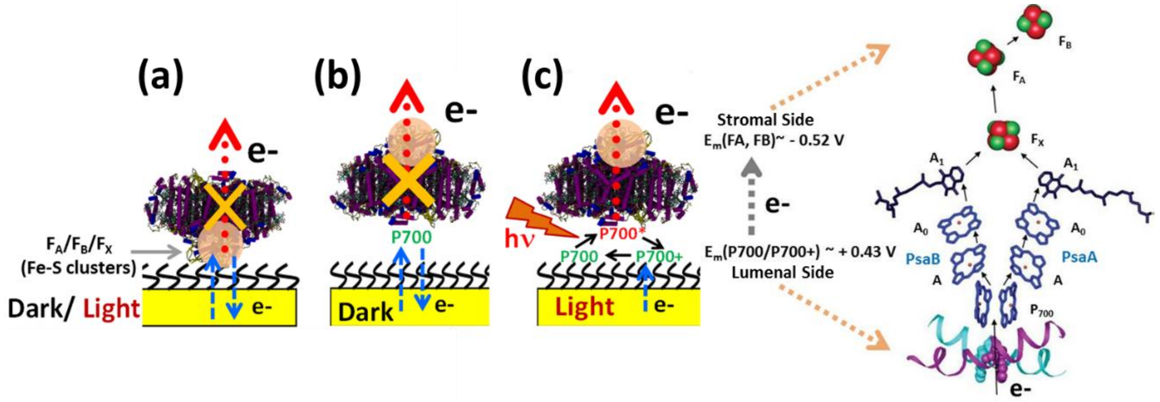

Figure 2.1 Schematics of the structure and dimensions of PSI along with the detailed photo-activated (λ = 680 nm) electron transfer pathway initiated at the lumenal side (P700/P700+) and terminated at F_A, F_B, F_X (Fe-S clusters) on the stromal side.[7, 100] Relationships between electronic activity and different PSI orientations on SAM/Au substrates for: a) stromal side ($F_A/F_B/F_X$ with Fe-S clusters) facing electrode under dark or, light conditions, b) lumenal side (P700 reaction center) facing electrode under dark conditions and c) lumenal side facing electrode under light conditions to promote enhanced electron transfer via photoactivated P700*.

side facing upwards due to weak hydrogen bonding of the lumenal side of PSI with the terminal OH group.[32, 102] Moreover, our recent comprehensive experimental studies of PSI immobilization on electron donor surfaces have revealed that by systematic manipulation of the solution chemistry, i.e., proper tuning of surfactant-protein interaction and deposition conditions, gravity driven or electric field assisted deposition techniques can be used to produce highly dense and uniform monolayer of PSI on a SAM/Au substrate.[28, 41, 45]

In an effort to understand the photo-activated properties of surface immobilized PSI, recent years have seen a host of electrochemical and photo-electrochemical studies. Many of these studies use dense mono- and multi-layers of PSI directly assembled on Au electrodes[46, 54, 60] or, PSI substrates in conjunction with electron scavengers such as methyl viologen (MV) in an electrolyte medium to complete a wet cell circuit.[42, 46-48] While new redox mediators, both acceptors and donors, are constantly being tested in new concentrations and combinations[32, 47-48, 50], MV has been the most widely used, in part because of its long history of being studied for toxicity effects and electron chain disruption[49]. Specifically, many photoelectrochemical measurements on surface assembled PSI systems have revealed the commonly accepted role of MV^{2+} as the external solution phase electron mediator and dissolved O_2 as the oxidizer to regenerate MV^{2+} from the reduced MV^{+}. Moreover, recent studies have shown enhanced photocurrents from directionally aligned PSI crystals on substrates as well as, PSI directionally immobilized on SAM/Au surfaces via cytochrome cyt_6 mediation.[103] Although such efforts provide valuable data for photo-electrochemical measurements on surface immobilized PSI, they do not provide a clear mechanistic picture for the electron transfer process. Precise morphological characterization of PSI complexes on the electron donor surface is required to determine the contribution of PSI to the electron transfer process. Moreover, the lack of fundamental understanding of the role of external redox mediators in dictating the directional photo-activated electron transfer from PSI trimers prevents any quantitative analysis of the bottlenecks for electron transfer. Thus, the understanding of whether the photocurrent generation is rate limited by mass transfer, redox kinetics, or chemical reaction rates is still an open question. To this end, the critical question that remains unanswered in the current state of the aforementioned research is, “How does the regeneration and migration of an external chemical as the electron scavenger effect photocurrent generation from PSI immobilized on SAM/Au surfaces?”

In this chapter detailed electrochemical measurements are used to investigate the role of dissolved O_2 in the electrolyte solution as an electron scavenger as well as its role in activating methyl viologen as a redox mediator during photocurrent generation from a uniform monolayer of Photosystem I (PSI) complexes assembled on alkanethiolate SAM (self-assembled monolayer)/Au surfaces. Specifically, results of direct measurements of light induced photocurrent from uniform monolayer assemblies of PSI on C9 alkanethiolate SAM/Au surfaces (refer to experimental section) are reported. These measurements confirm the ability of dissolved O_2 in the electrolyte to function as a weak electron scavenger for PSI. More importantly, they demonstrate the formation of an intermediate methyl viologen-oxygen complex that directly scavenges the photo-excited electrons from the terminal Fe-S cluster (F_B) of PSI.

2.2 Experimental Section

2.2.1 Growth and isolation of PSI

The thermophilic cyanobacterium *T. Elongatus* BP-1 was grown in 2L airlift fermenters (Bethesda Research Labs, Bethesda MD) in NTA media.[104] The details of the extraction and purification of the trimeric PSI complexes grown from *T. Elongatus* cells are provided elsewhere.[41] Based on spectrophotometer measured chlorophyll concentrations, the concentrations of the extracted PSI trimers was estimated to be around $C_B = 1.42 \times 10^{-5}$ mol/L. PSI trimers were stored in aliquots of 1.5 ml at -80°C for future use.

2.2.2 Preparation and analysis of electrode monolayers

Commercial gold electrodes with 1.6 mm diameter, 2.011 mm^2 working area (BAS Inc.; Model: MF-2014) were cleaned in a three-step process. First, they were treated with base piranha solution (RCA wash with 1:1:5 volume ratios of $NH_4OH:H_2O_2:H_2O$) at a temperature of 75^oC for 15 min to remove organic residues. They were then polished with 0.05micron alumina polish for 3 minutes. Finally, the electrodes were electrochemically cleaned by running cyclic voltammetry from -400 to +1400 mV vs Ag/AgCl at 200 mV/sec for 25 cycles in 0.1 M H_2SO_4 solution followed by ultra-sonication in isopropanol (99.99% v/v) then de-ionized water for 10 min, and drying in N_2 stream. Commercial glassy carbon (GC) electrodes were used with 3.0 mm diameter, 7.069 mm^2 working area (BAS Inc.; Model: MF-2012) were cleaned only with polishing, sonication, and drying in N_2 stream.

The OH-terminated SAM were formed by immersing the clean Au electrodes in 1 mM 11-mercapto-1-undecanol and 9-mercapto-1-nonanol (97% and 96% purity respectively; purchased from Sigma-Aldrich) in ethanol for 7 days[105] at room temperature in a glove box filled with dry N_2. The SAM/Au electrodes were rinsed in ethanol, sonicated in isopropanol, and dried in dry N_2 stream. Surface immobilization of PSI was carried out by incubating the SAM/Au electrodes for ~ 24 hours in colloidal suspension of PSI in 200 mM Na-phosphate aqueous buffer (pH = 7.0). Based on our earlier solution chemistry work to tune inter-protein distances that result in a "jammed" suspensions,[45] a high PSI concentration of ~ 1.4 x 10^{-3} mM stabilized with 0.02% w/v (i.e., 2.2 times the critical micellar concentration) of the detergent n-dodecyl-β-D-maltoside (DM; purchased from Gold Biotechnology) was specifically chosen to produce uniform, monolayer assemblies of PSI. Since the gold electrodes could not be mounted on the atomic force microscopy (AFM) measuring platforms, AFM topographical characterizations for PSI on SAM/Au substrates were carried out on samples prepared using an identical solution phase treatments outlined above on Au coated silicon wafers (Au thickness ~ 100 nm) with a titanium adhesion layer purchased from Platypus Technologies. Multi-layer assemblies of PSI on cleaned glassy carbon (GC) electrodes were achieved by drop casting 2.5 µL of stock PSI solution, placed under 30 in. Hg vacuum for 15 minutes, and rinsed in de-ionized water.

All surface topography images were collected on a Digital Instruments (Veeco) make atomic force microscopy (AFM) instrument (Model: NanoScope IIIa) in tapping mode using a silicon cantilever compatible with softer biological materials (Make: Olympus; Model: AC240TS). The tip had a force constant of 2 N/m^2 along with a resonant frequency of 70 kHz, and the images were recorded at a scan rate of 0.863 Hz. Surface layer thicknesses were measured using a *DRE-Dr. Riss Ellipsometerbau Gmbh* make ellipsometer (Model: EL X-02C) operating with a laser wavelength of 632.8 nm at an incidence and polarizer angle of 70°. All PSI/SAM/Au systems were analyzed using a three-layer (Au-thiol-PSI) model, where C9 and C11 thiol monolayer thicknesses were assumed to be ~ 0.77 and 0.95 nm respectively (based on C-C bond lengths and the brush tilt angle of 30^o to the surface normal). As reported in our earlier work[41] and for ease of data analysis, the refractive indices for surface-assembled PSI and thiols were assumed to be 1.46 altogether.

2.2.3 Electrochemical investigations and photocurrent measurements

Electrochemical measurements were conducted with a Bio-Logic potentiostat (Model: SP-200) operated by the EC-Lab software. A glass electrochemical cell with three-electrode configuration was used that carried a Pt wire counter electrode, Ag/AgCl (sat. KCl) reference electrode (Make: BAS Inc.; Model: MF-2052 with a reference shift +0.197 V vs. NHE) and the Au working electrode with the specific surface treatments (SAM/Au and PSI/SAM/Au electrodes for the controls and specifics respectively). The potential window for all experimental scans were chosen between -0.9 to +0.6 V (i.e., -0.7 to +0.8 V vs. NHE) to avoid interference from complex Au oxide peaks above +0.8 V vs. NHE. Except where specified, all electrochemical measurements were carried out in a standard electrolyte of 200 mM Na-phosphate aqueous buffer (pH = 7.0) to prevent any protein denaturation. Cyclic voltammetry (CV) data were collected with a scan rate of 200 mV/sec, except where stated at 20 mV/sec and 1000 mV/sec. Chronoamperometry (CA) data were collected at a bias of +0 V vs reference and idled for 20 minutes before exposing PSI/SAM/Au electrodes to light in 2 – 5 minute pulses. This potential was chosen to facilitate the photoresponse solely from PSI. It should be mentioned that as bias potentials are shifted further positive or negative, SAM/Au surfaces demonstrated increased photoactivated redox interaction, potentially from stripping of the thiol brushes. This bias is close to open circuit voltage (OCV) for all tested PSI/SAM/Au constructs, with minor background current shifts. We note here that the OCV shifts with varying solution content and concentrations, as well as surface modifications. A constant bias voltage was chosen over OCV to control the energy gap at the electrode surface, which greatly affects the electron kinetics of transfer to and from PSI or methyl viologen (MV). Stepped chronoamperometry data were collected at a series of bias potentials, stepping from -200 to +350 mV vs reference, and exposed to light in 2 - 5 minute pulses. For all control experiments requiring the purging of the dissolved O_2 from the buffer electrolyte, nitrogen (N_2) gas was bubbled through the solution for 15 minutes followed by a continuous sheath of N_2 gas being maintained above the solution throughout the experiment. For the oxygen imbued runs, O_2 was bubbled through the solution for 30 minutes, followed by a continuous sheath of O_2 gas flow above. The O_2 levels were measured with an ExStik II Dissolved Oxygen Meter (Model: DO600). 1 mM of methyl violgen (MV) was added as the electron scavenger. All data were measured in dark, room temperature conditions except for the light experiments where the measurements were taken while the working electrodes was under illumination from an LED whitelight source (ThorLabs; model:

MWWHL3) with a nominal intensity of 1000 W/m^2 before being passed through a red filter (λ = 635 - 650 nm).

2.3 Results and Discussion

2.3.1 Characterization of PSI deposition on SAM/Au substrates

The uniform, monolayer depositions of PSI on SAM/Au substrates as obtained via self-assembly from solution-phase are seen from the AFM topographical images in Figures 2.2a – 2.2f. These uniform surface assemblies are achieved through the use of specific PSI/detergent concentration ratios to maintain the individual PSI complexes in colloidal suspension[45] (details provided in experimental section). The AFM images depicted in Figures 2.2a and 2.2b show the controls prepared with alkanethiolate SAM/Au surfaces are devoid of PSI. In accord with earlier studies,[105] the images reveal uniform and dense brush layer formation on C11-alkanthiolate (C11-thiol) surface (Figure 2.2a) as compared to the relatively sparse assembly on C9-alkanethiolate (C9-thiol) surface (Figure 2.2b). Furthermore, AFM images for PSI attachment to SAM/Au surfaces with both C11-thiols and C9-thiols (Figures 2.2c and 2.2d) indicate a relatively uniform monolayer formation as indicated by the cross-section profile shown in each of the cases (Figures 2.2e and 2.2f). Typical average protein diameters of d = 32.3 ± 4.5 nm (corresponding to arrows marked on Figures 2.2c and 2.2d) as well as average heights of h = 8.4 ± 2.3 nm, as indicated in Figures 2.2e and 2.2f, are recorded from the cross-sectional profiles of PSI deposition on both C11 and C9 alkanethiolate SAM/Au surfaces. These dimensions are commensurate with the expected size of detergent bound PSI trimeric complexes.[41, 45] Additionally, ellipsometry measurements for PSI assembly on C11 and C9 alkanethiolate SAM/Au surfaces indicate the average PSI layer thicknesses to be ~ 4.2 to 5.1 ± 0.2 nm (i.e., surface coverage of ~ 50 - 65%). These measurements, when compared to an average thickness of ~ 8.0 nm for PSI spheroids with ~ 9 nm height and optimal hexagonal packing factor ~ 0.9 - 0.91, indicate that the PSI monolayer considered in this study do not exhibit maximum packing. Such results are in agreement with our earlier studies on PSI deposition from solution phase.[45] However, for the purpose of the current study it was not critical to attain PSI monolayer with maximum packing density as done in our prior studies via electric field assisted deposition.

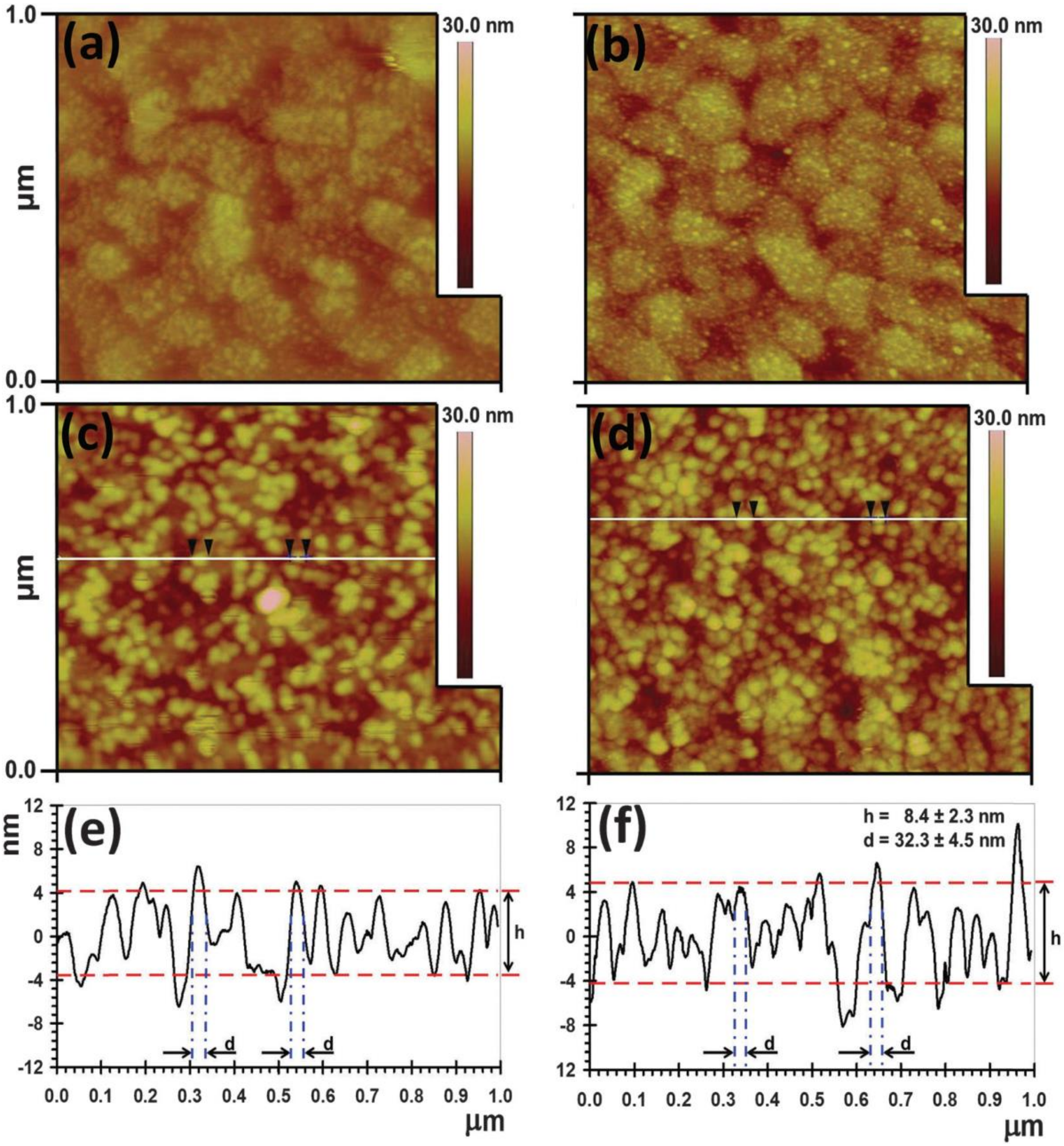

Figure 2.2 AFM images showing the surface topographies of: a) C11-thiol SAM/Au and b) C9-thiol SAM/Au substrates (background) as well as those for the respective: c) PSI/C11-thiol SAM/Au and d) PSI/C9-thiol SAM/Au substrates. Representative cross-sectional surface profiles (e & f) for PSI assembled SAM/Au substrates are shown below the respective AFM images (c & d).

2.3.2 Electrochemical measurements to detect PSI activity

Figure 2.1 depicts the possible PSI trimer attachments: 1) stromal side ($F_A/F_B/F_X$ with Fe-S clusters as marked by the orange circle) facing electrode under dark or, light conditions (Figure 2.1a); 2) lumenal side (P700 reaction center) facing electrode under dark condition (Figure 2.1b) and 3) lumenal side facing electrode under illumination (Figure 2.1c). In scenario 1), irrespective of dark or, light conditions, there would be only electron exchange between the accessible F_A/F_B redox centers and the Au electrode (electron donor) when biased at the F_A/F_B mid-point potential, but with no soluble electron donor to complete the circuit. In scenario 2), electron transfer cannot occur in the dark, even with upward orientation, as no photo-excited electrons are generated by PSI, causing it to act as an insulator. Only in scenario 3), where PSI trimers assembled on SAM/Au surfaces with upward orientations of $F_X/F_A/F_B$ are illuminated (Figure 2.1.c), the photoexcitation of P700 → P700* is energetically activated. In turn, the photoexcited reaction center gets oxidized (P700* → P700+) to initiate the electron release to the acceptor chlorophylls, A_0 in the PSI electron transfer chain. The electron deficient and energetically relaxed P700+ scavenges an electron from the Au donor to get reduced as P700+ → P700 for the next cycle of photoexcitation, provided a suitable electron scavenger such as methyl viologen (MV) is present to receive the electron from F_B.

Preliminary cyclic voltammetry (CV) measurements on the SAM/Au (controls) and PSI/SAM/Au (specific) electrodes in Na-phosphate buffer electrolyte (without any external electron scavenger) indicate capacitive (non-faradaic) current built-up due to the presence of dense thiol brushes, in particular for the C11-thiol samples. This background capacitive current masks the signal enhancement in photo-current due to the presence of PSI on SAM electrodes. Thus, once background is subtracted for the control (SAM/Au electrodes) data, negligible CV peaks for PSI redox centers (P700 and Fe-S cluster) were observed. These experiments, in accordance with earlier studies,[42, 106] indicate that the CV technique does not possess the sensitivity to clearly identify the electrochemical activities associated with the PSI redox centers from PSI/SAM/Au electrode assemblies. Additionally, chronoamperometry (CA) measurements revealed no discernable photoresponse on the PSI/C11-thiol SAM/Au electrodes. Thus, we believe that the dense brush layer on C11-thiol/ Au electrode, though ideal for better coverage of PSI monolayer, acts as an insulation barrier that retards electron transfer to the activated P700 reaction center. It should be mentioned here that accumulation of surface roughness during electrode polishing and cleaning prevents perfectly dense SAM formation, reducing the insulating effects and exposing underlying Au directly to solution. However, because the attachment of PSI is guided by the presence of SAM layers, localized insulation occurs. Hence, all electrochemistry measurements from hereon are reported only for the PSI/C9-Thiol SAM/Au samples wherein observable photocurrent from CA measurements are presented.

2.3.3 Photocurrent measurements mediated by the presence of dissolved O_2

Chronoamperometry measurements were carried out on PSI/C9-Thiol/Au electrodes in light/dark with the addition of MV under both aerobic and anaerobic conditions. We would like to mention here that the aerobic conditions refer to the ambient equilibrium level (~5 mg/L) of dissolved oxygen (O_2) in buffer electrolyte solutions. Figure 2.3a shows that in the presence of MV and dissolved O_2 (Figure 2.3a, O_2 present case in blue) a stable photocurrent of ~ 6 nA/cm^2 (negative directions as compared to baseline current) is achieved that is comparable to previously reported values from CA measurements on PSI/C6-Thiol/Au electrodes[42]. While a mixed orientation of PSI complexes is expected on SAM/Au surfaces, the photoresponse in Figure 2.3a demonstrates that the dominant electron transfer pathway involves reduction of photo-excited P700*/P700$^+$ by electrons from the Au donor. Current understandings of the electron transfer mechanism assume the final oxidation of F_B^- (redox potential ~ -0.53 V vs normal hydrogen electrode, NHE) at the stromal side of PSI is directly mediated by the electron being scavenged by MV^{2+} (redox potential ~ -0.45 V vs NHE). However, upon removal of all dissolved O_2 through systematic purging with nitrogen (N_2) in the electrolyte solution, this photoresponse shifts to a sharp positive spike in current (see Figure 2.3a, O_2 removed case in red). Such photocurrent spike is indicative of electron transfer into the Au surface via oppositely oriented PSI, that rapidly due to the unavailability of suitable charge carriers in solution to donate electrons to P700$^+$.

In an effort to understand the exact role of O_2 in the electron mediation from PSI immobilized on SAM/Au substrates, CA measurements were carried on identical PSI /SAM/Au electrodes in buffer electrolyte solution devoid of any MV. As expected, Figure 2.3b shows no photoresponse in the absence of oxygen (O_2 removed case in red). However, O_2 in the solution alone is able to scavenge electrons from F_B^- to produce a steady negative photocurrent of ~1.5 nA/cm^2 even in the absence of MV as the charge carrier (O_2 present case in blue). This confirms, a hypothesis put forward in an earlier study[50], that O_2 in solution alone can directly scavenge

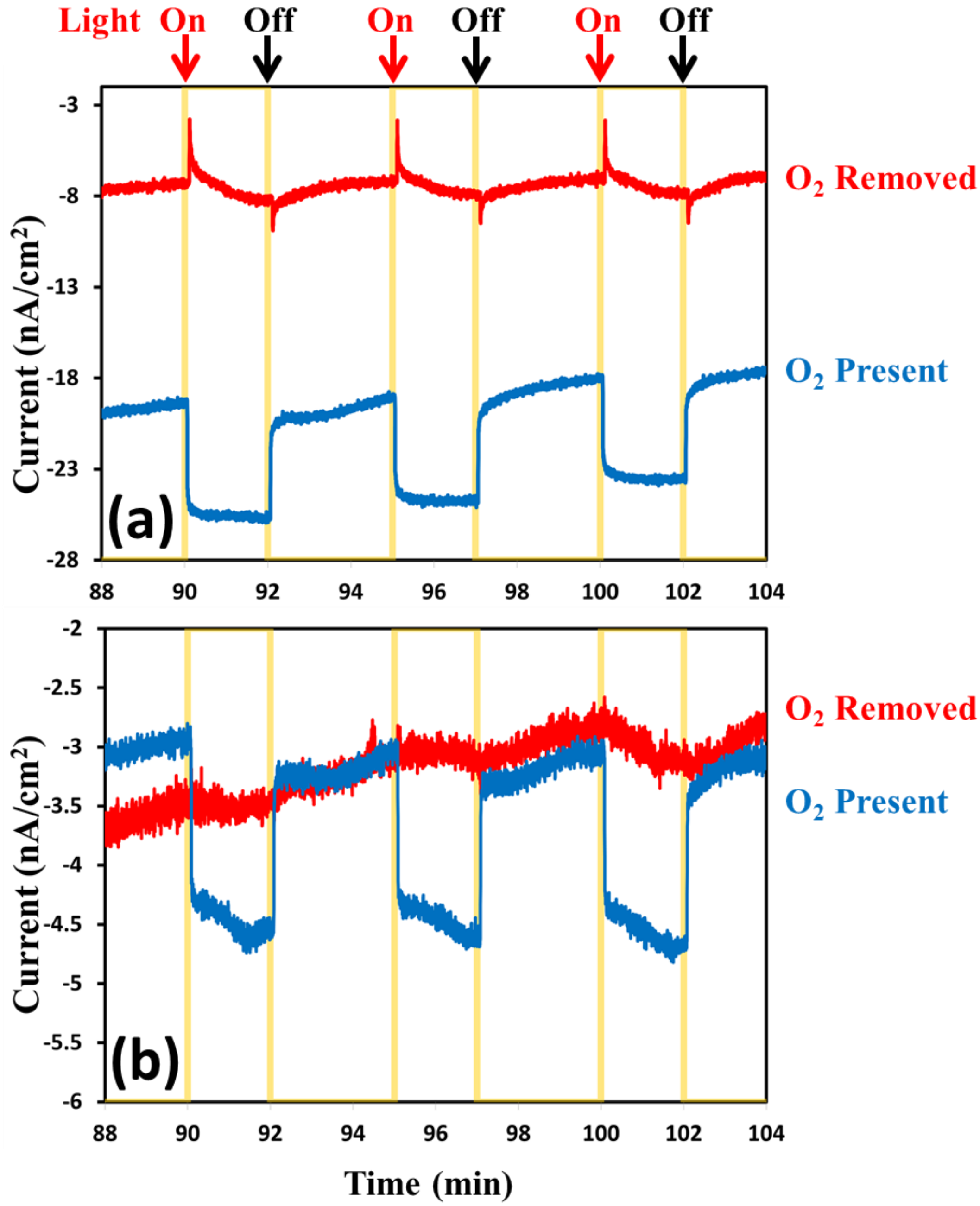

Figure 2.3 Chronoamperometry on PSI/C9-thiol SAM/Au electrodes at +0 V bias vs Ag/AgCl under illumination (λ = 635 - 650 nm) under both aerobic (O_2 present; blue line) and anaerobic (O_2 absent; red line) conditions with: a) 1 mM methyl viologen (MV) added as charge carrier showing suppression of photocurrent with O_2 removed; b) all charge carrier removed from solution, showing small direct scavenging of electrons by O_2.

electrons from F_B^-. However, the interaction between dissolved O_2 and MV remains still unclear, since there is a 4-fold increase in photocurrent when MV is added under aerobic conditions as compared to the corresponding photoresponse under anaerobic conditions. To enhance our understanding of the role of O_2 in scavenging the photoactivated electrons, we further ask the question: If removal of oxygen from the system suppresses the photocurrent response, then does increasing the oxygen content enhance it? To this end, fully purged solution was subsequently oxygenated in incremental stages by bubbling a 70%N_2/30%O_2 gas, while recording the photoresponse as dissolved O_2 content increased. As seen in Figure 2.4, this photocurrent peaks at ~5 mg/L, which incidentally coincides with the ambient level of dissolved O_2 found in freshly deionized Millipore water. The subsequent decrease in photocurrent is attributed to oxygen reacting with the sulfur group of thiol to strip the SAM and remove PSI from the surface. Thus, for given amounts of MV and PSI present, the normal level of oxygen found in our solution is sufficient to maximize the photoresponse. Although our observations confirm the catalytic role of dissolved O_2 in activating the solution-phase MV to effectively scavenge the electrons, they do not provide a fundamental understanding of the mechanism that makes the presence of dissolved O_2 imperative to sustained photocurrentssdf

2.3.4 Electrochemical measurements indicative of an intermediate redox species

The commonly accepted mechanism[107] of the reduction of solution-phase MV^{2+} by F_B^- ($MV^{2+} \rightarrow MV^+$) followed by their regeneration due to oxidation by O_2 ($MV^+ \rightarrow MV^{2+}$) appears insufficient to explain the behavior seen in Figure 2.3a. To further elucidate the role of O_2, let us assume that the aforementioned and commonly accepted electron transfer mechanism holds true. In the absence of dissolved O_2, one would expect a negative photocurrent spike which would quickly decay. The substantial (1 mM) population of MV^{2+} in the immediate vicinity of the PSI layer should still scavenge electrons initially. However, without O_2 to regenerate the MV^{2+}, available scavenger species at the surface would be exhausted and photocurrent intensity would diminish. In contrast, the photocurrents observed in Figure 2.3a in the absence of O_2, with MV as the electron scavenger in solution, shows a sharp positive response that quickly decays in time. While such observations provide weak indication of the possibility of MV^+ donating to reduce $P700^+$, as proposed by others[108], it raises questions about the current picture of PSI- MV interactions.

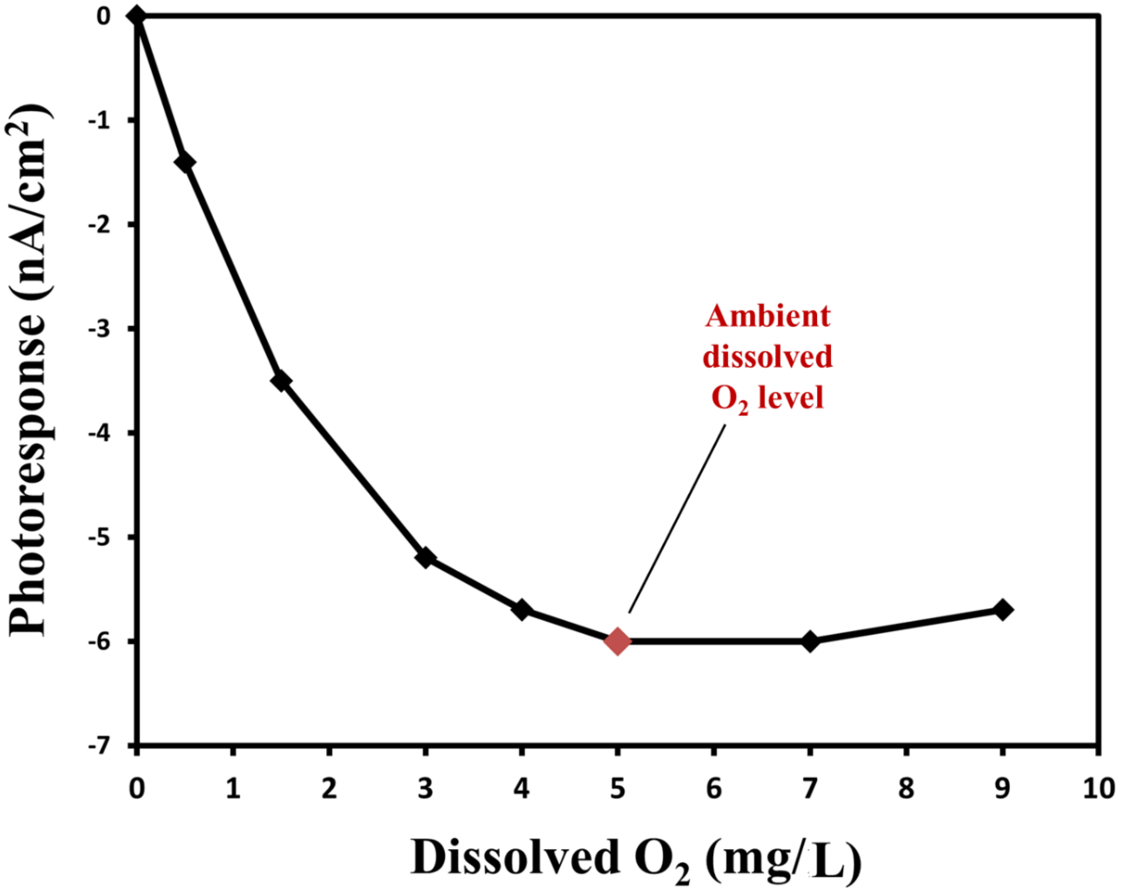

Figure 2.4 Net photocurrent change in series of chronoamperometry on PSI/C9-thiol SAM/Au electrodes at +0 V bias vs Ag/AgCl under illumination (λ = 635 - 650 nm) with 1 mM methyl viologen. O_2 concentration heavily regulates the scavenging of electrons from PSI. For the given concentration of MV, adding oxygen beyond the ambient amount present in Millipore deionized water did not further increase the photoresponse of PSI.

To this end, cyclic voltammetry (CV) measurements on PSI/SAM/Au electrodes in buffer electrolytes carrying solution-phase MV, both with and without oxygen, reveal a new electrochemical pathway for the electron transfer process. In Figure 2.5, dark CV scans at 200 mV/s in electrolytes containing MV, but purged of all O_2, demonstrate a repeatable, stable trace over 20 cycles with the well-established redox peaks (-450 mV vs NHE)[109] for $MV^{2+} \leftrightarrow MV^{+}$. However, the addition of O_2 not only brings the expected increase in cathodic current at negative potentials due to electrons being scavenged form the electrode surface, but also introduces a new irreversible peak indicating the reduction of an unknown solution-phase chemical species at ~ -325 mV vs NHE. This peak diminishes with successive cycles, indicating an irreversible electron transfer process which results from depletion of the aforementioned species at the electrode surface. This peak reappears slowly over time between scans and more quickly if the solution is shaken to promote O_2 diffusion from the air, which indicates the formation of a metastable methyl viologen-oxygen complex [MVO*]. In order to determine if this [MVO*] species was created at the electrode surface, CV scans at greatly reduced and increased scan rates were repeated (Figure 2.6).

The slowest scan rate of 20 mV/s indicated a stable trace, while the fastest scan rate of 1000 mV/s greatly amplified the trend of the disappearing peak at ~ -325 mV (vs NHE) with successive cycles. Such measurements indicate that this species is generated in the bulk solution and reduced at the surface. To further understand this process, we specifically carried out CV scans while purging the MV solution with additional pure O_2 (Figure 2.7). It is observed here that the distinct shoulder features of the individual redox peaks become less distinguishable since the excessive dissolved oxygen content provides a significant background reduction current. However, it can still be clearly seen that the specific redox peak for this [MVO*] complex significantly increases in both magnitude and breadth. Simultaneously, the peak to peak height difference for the MV^{+}/MV^{2+} redox couple reduces by ~50% after the first cycle. This reduction would be expected if the increased O_2 concentration has shifted the equilibrium concentration in favor of the [MVO*] complex, reducing the concentration of MV^{2+} species present. In successive cycles, the MV^{+}/MV^{2+} redox couple peak stabilizes in magnitude, while the shoulder feature continues to diminish as this [MVO*] complex is irreversibly consumed upon reduction. While these results clearly indicate the spontaneous formation of the aforementioned complex before any interaction with PSI, as also hypothesized before, the unanswered question here is whether the concentration

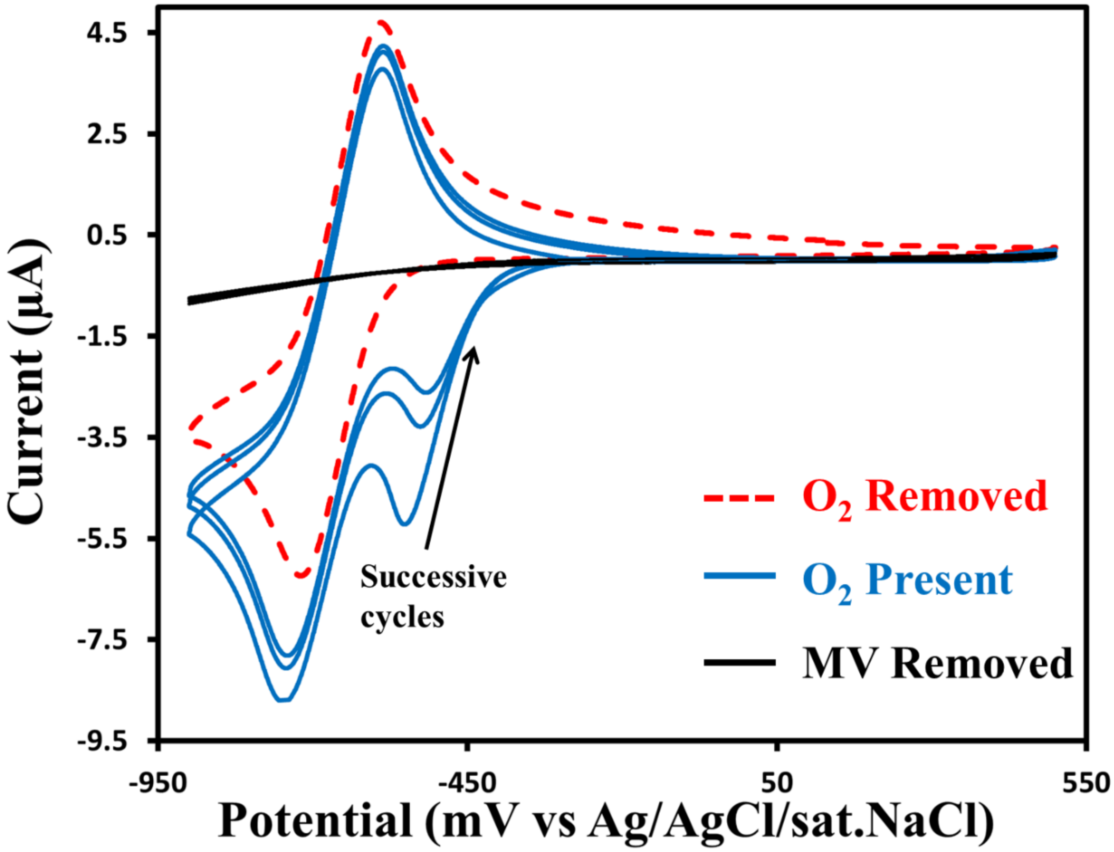

Figure 2.5 Cyclic Voltammetry scans at 200 mV/s on PSI/C9-thiol SAM/Au electrodes vs Ag/AgCl in dark with 1 mM MV in solution. When purged with nitrogen to remove all oxygen, the scans exhibited a stable repeated single redox peak for MV at the expected potential of ~ -0.65 V. When oxygen is introduced, an irreversible redox peak appears that diminishes in magnitude upon successive scans, which is attributed to the reduction of the metastable methyl viologen-oxygen complex.

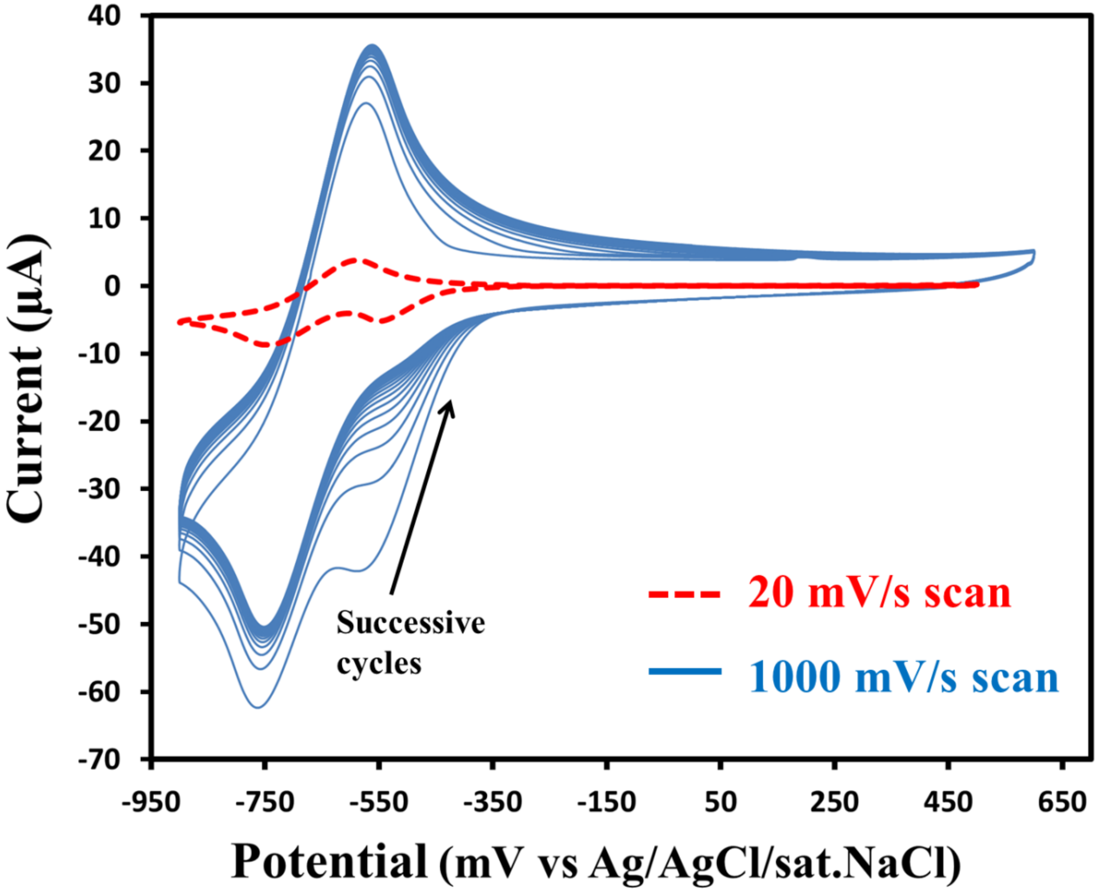

Figure 2.6 Cyclic Voltammetry scans on PSI/C9-thiol SAM/Au electrodes vs Ag/AgCl in dark with 1 mM MV in solution in aerobic conditions. Immediately stable trace at 20 mV/s scan and greatly diminishing reduction peak at 1000 mV/s scan indicates a methyl viologen-oxygen complex being formed in solution and consumed at the electrode surface.

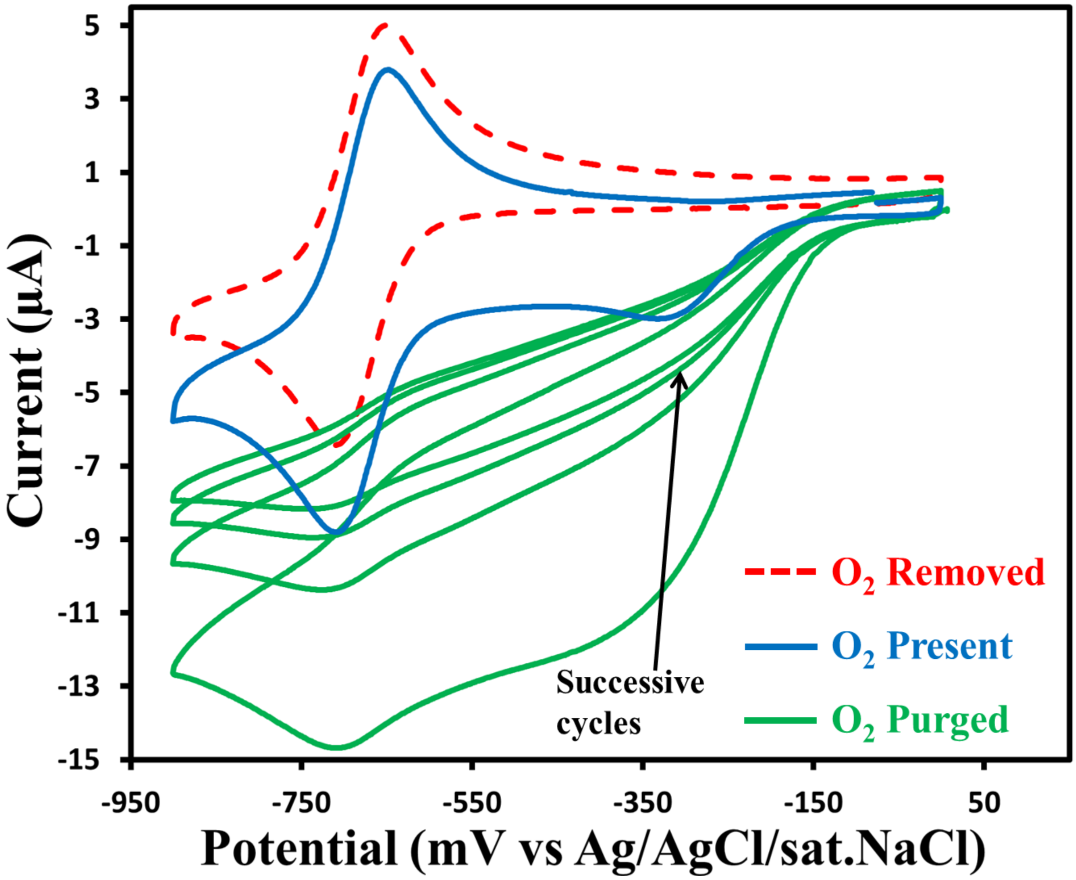

Figure 2.7 Cyclic Voltammetry scans at 200 mV/s on PSI/C9-thiol SAM/Au electrodes vs Ag/AgCl in dark with 1 mM MV in solution. When purged with nitrogen to remove all oxygen, the scans exhibited a stable repeated single redox peak for MV at the expected potential of ~ -0.65 V. When pure oxygen is bubbled through the solution, the irreversible redox peak appears grows in magnitude, while the distinguishable MV^{+}/MV^{2+} pair diminishes by ~50% peak to peak height.

of this complex is the limiting factor that inhibits the electron transport chain of substrate → PSI → the final solution-phase scavenger.

In an effort to investigate the ability of methyl viologen to scavenge electrons directly in the absence of oxygen, we sought to augment the observed photocurrent effects at varying electrode bias voltages. However, the thiol SAM/Au formation proves to be unstable when the electrodes are exposed to a wider range of bias potentials over long periods of times (as required for CA experiments), especially deteriorating rapidly at negative overpotentials. Thus we drop cast PSI directly onto glassy carbon electrodes (GCE) to form multilayers that are stable over a much larger range of bias potentials and for longer periods of time (Figure 2.8). Applying a negative bias potential increases the electron energy at the electrode surface, thereby facilitating the charge transfer to $P700^+$. If MV^{2+} is the primary species scavenging electrons from F_B^-, we should see a significant increase in the magnitude of the photocurrent with decreasing bias potential on the electrodes. However, in the absence of O_2 (Figure 2.8), the net photocurrent values at bias potentials < 100 mV (vs NHE) are significantly suppressed as compared to the corresponding values in the presence of oxygen. Added to this, the characteristic trend for the photoresponse curve at -100 mV bias potential in Figure 2.9a indicates the same response as previously observed for the 0 V bias potential case. Thus, we observe an immediate and stable negative photoresponse in the presence of O_2 (Figure 2.9b). However, in the absence of O_2, we only see a slower decay towards a negative response (Figure 2.9a). To sum it up, even at negative overpotentials, no sharp photoresponse indicative of any direct electron scavenging by MV^{2+} alone was observed.

Our explanation for the aforementioned phenomena is that MV^{2+} first reacts with O_2 to form a new intermediate complex, [MVO*]. This species then directly scavenges the electron from PSI and is subsequently regenerated to MV^{2+} while producing H_2O_2, as depicted in Figure 2.10. This is in contrast with the previous understanding that MV^{2+} directly takes up an electron from PSI to then react with O_2 and form H_2O_2. Previous work has pointed towards a large number of possible intermediates: $[MV^+O^-]$, [MVO], $[MVO^+]$, $[MV(O)_2]$, $[MV^+O_2^-]$, $[MV(OH)_2]$,[110] along with the possibility of directly photogenerated $[MV^{+\cdot}]$.[111] Due to the ephemeral nature of such solution-phase complex formation, it is outside the scope of this work to propose the exact molecular structure of the intermediate species, except to say that it is an electron-starved species which reacts upon reduction. With the aim of choosing suitable electron scavengers through a fundamental understanding of the electron transfer pathways, it is sufficient to replace the existing

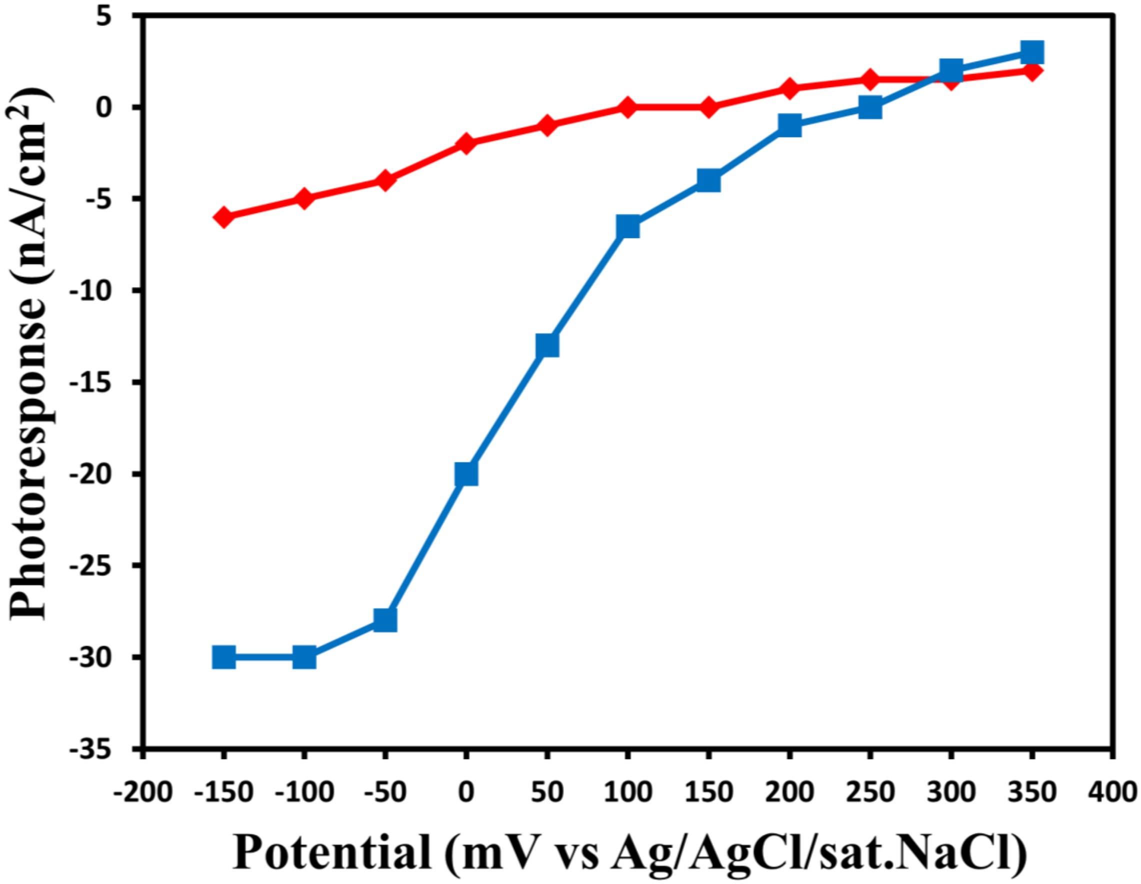

Figure 2.8 Net photocurrent change in series of continuous chronoamperometry biased steps on dropcast PSI/GC electrodes under illumination (λ = 635–650 nm) with 1 mM methyl viologen (MV) added as a charge carrier under aerobic and anaerobic conditions.

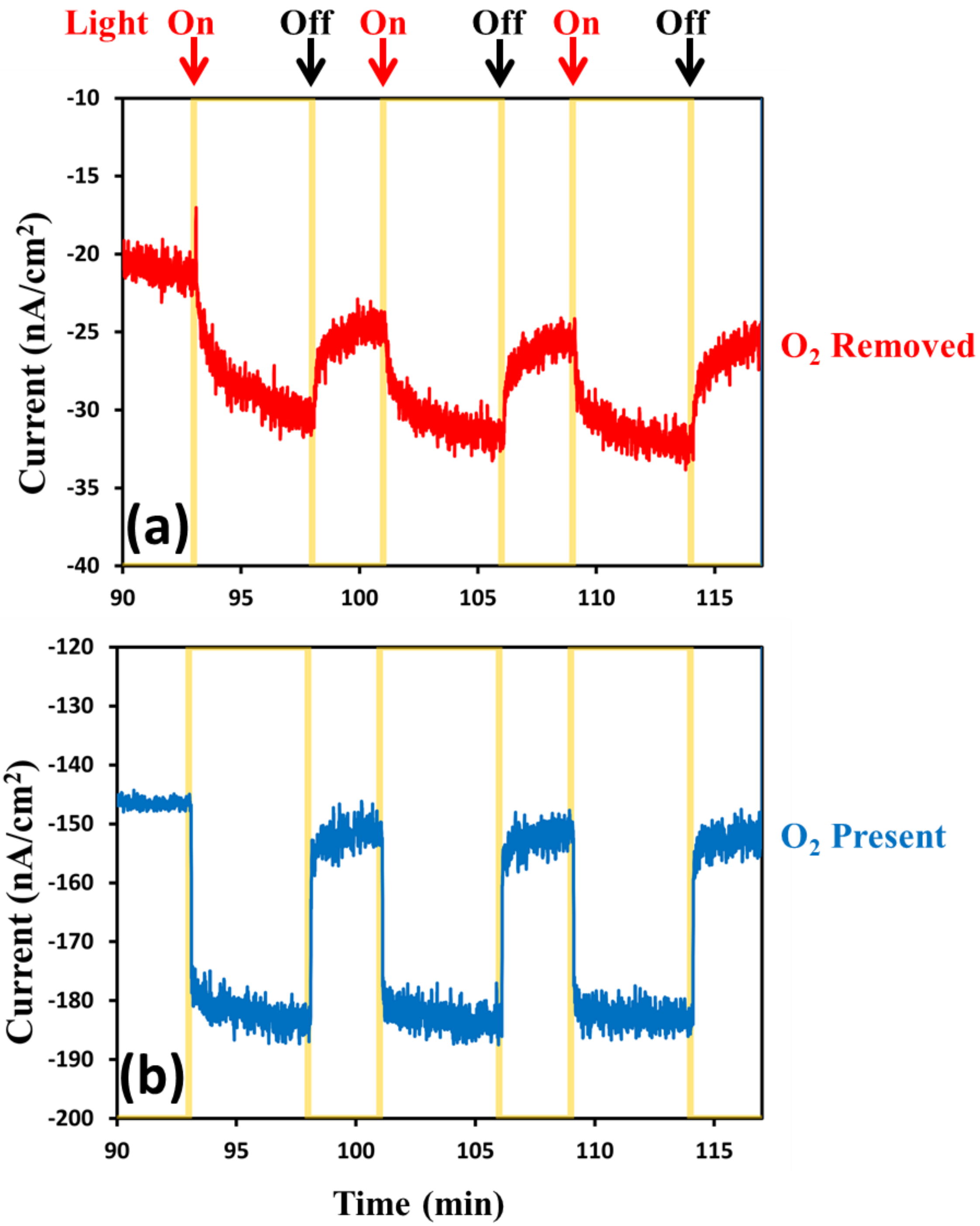

Figure 2.9 Chronoamperometry on dropcast PSI/GC electrodes at -100 mV bias vs Ag/AgCl under illumination (λ = 635 - 650 nm) with 1 mM methyl viologen (MV) added as charge carrier under a) anaerobic (O_2 removed, red line) and b) aerobic (O_2 present; blue line) showing suppression of photocurrent with O_2 removed. Even at negative overpotentials, the distinct characteristic differences in the photoresponse curves indicates a separate species from MV^{2+} involved in electron scavenging.

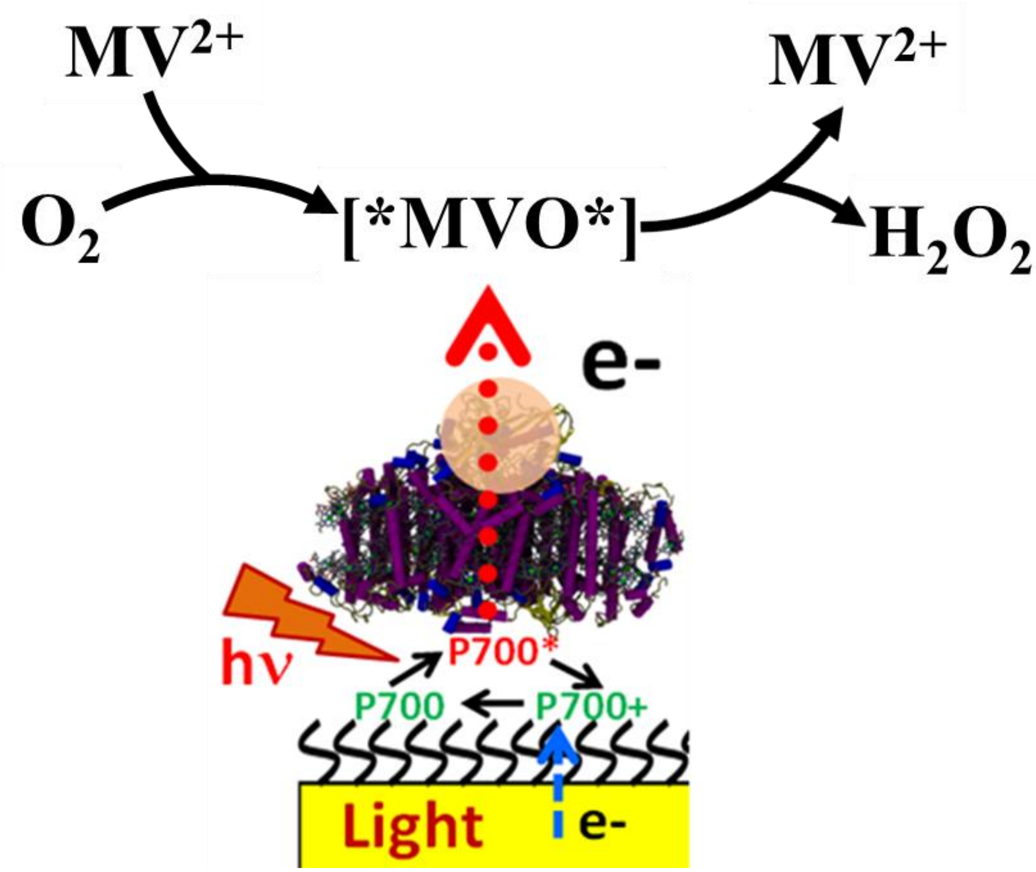

Figure 2.10 Proposed series of events with MV reacting with oxygen to form an intermediate, which is the species responsible for direct electron scavenging, in contrast to the understanding of MV^{2+} directly scavenging and subsequently being regenerated by O_2.

model of MV^{2+} scavenging and subsequently donating the electron to O_2 with a more accurate model as depicted schematically in Figure 2.10. Thus, when using MV as an electron scavenger in the presence of oxygen, the emergence of this intermediate species as the primary electron scavenger makes it more rational to consider the effective redox potential of the scavenger as -325 mV vs NHE instead of the previously assumed -450 mV.

2.4 Conclusions

Chronoamperometry measurements under light and dark conditions reveal the mechanistic picture behind the electrochemical pathway mediated by methyl viologen for the electron transport from the stromal F_A/F_B terminal of PSI (the ones that are directionally oriented) to the counter electrode in solution. Specifically, our experiments reveal the critical role of solution-phase dissolved O_2 concentrations in producing an intermediate complex (MVO*), heretofore not accounted for, that facilitates the electron scavenging mechanism in the presence of MV. Thus, the rate limiting step in the kinetics of photocurrent generation from PSI/SAM/Au systems is directly related to the rate of formation of this complex, as evidenced by the non-linear increase in photocurrent density with increasing dissolved O_2 concentrations.

The proposed model for the electron transfer pathway from our current findings paves the way for rational design of PSI wet cells that use combinations of well-known mediators such as methyl viologen and ferrocyanide[47], or methyl viologen and an osmium base[32]. In the framework of such a model, the redox potential for electron scavenging by the most successful and widely used methyl viologen needs to be re-adjusted from -450 mV to -325 mV vs NHE. Such observations provide critical insight into the optimization of the energetics of electron transport pathways from PSI to a soluble carrier, solid-state electrode, or bound catalysts in future photoactivated bio-hybrid energy harvesting constructs.

CHAPTER 3

CONFINEMENT AND PHOTOACTIVATION OF PSI IN A METAL–ORGANIC FRAMEWORK

This chapter is based on the submitted paper:

"Jolly green MOF: confinement and photoactivation of photosystem I in a metal–organic framework," by Tyler H. Bennett, Michael D. Vaughn, Seyyed Ali Davari, Kiman Park, Dibyendu Mukherjee and Bamin Khomami.

3.1 Introduction

Photosystem I (PSI) is a chlorophyll-rich transmembrane protein complex responsible for driving the light-activated charge separation and electron transport during the photosynthesis cycle in plants and bacteria. Specifically, membrane bound PSI exists in trimeric form and weighs 1068 kDa in the cyanobacterium *T. Elongatus*.[6-7] It acts as a biological photodiode shuttling electrons from the lumenal side (P_{700}^{+}, E_m = +490 mV) to the stromal side (F_B^{-}, E_m = -530 mV) of PSI with nearly 100% quantum efficiency.[7] The broad visible spectrum activity and remarkable charge separation properties of PSI have recently resulted in a series of intense studies, both to understand its fundamental mechanisms and to incorporate it into bio-hybrid photochemical and optoelectronic materials.

Past studies have extensively investigated the photoelectrochemical activities of PSI layers attached to conducting surfaces such as gold electrodes,[28-32] carbon nanotubes,[15, 33-34] metal oxide nanowires,[35] or plasmonic nanostructures.[36-38] However, a significant hurdle in these studies has been the weak optical absorption of a single PSI monolayer (only 0.34% of incident light at 680 nm).[53] In order to absorb appreciable light for generating significant photoresponse from PSI, multi-layer assemblies have been deposited on a variety of surfaces including p-doped silicon,[55] and graphene.[23, 56-57] In an effort to move away from vacuum-assisted drop-casting films which is difficult to precisely control and stabilize, one would envision suitable scaffolds for supporting PSI in multi-layered thin film structures that can provide stability as well as facilitate efficient charge transport. To this end, various research groups have investigated the use of mesoporous electrodes,[20] hydrogels,[50] conductive polymers,[58-60] or even combinations of DNA binders and complementary enzyme assemblies.[61] More recently, the PSI research community has increasingly turned its attention towards the design of tailored structural microenvironments when incorporating PSI into bio-hybrid materials. Reconstituting PSI into organic or inorganic frameworks including lipid bilayers[64-65] that mimic the native thylakoid membrane has shed light on how microenvironment alterations in the structural scaffold of PSI might affect the coherent or incoherent energy transfer of the chlorophyll network.[62]

Here we propose the next step of incorporating PSI into a unique metal organic framework to investigate these confinement effects. Metal organic frameworks (MOFs) are rapidly emerging as the new class of materials that comprise highly organized crystalline structures made from inorganic (metal) nodes connected by organic linkers. Such networked structures are tunable with near infinite possible combinations of nodes and linkers. Furthermore, MOF structures are highly permeable with pore sizes ranging from 0.3 to 10 nm[67] and astonishingly large free volumes (over 90%)[68] and surface areas (over 10,000 m^2/gm).[69] Currently, there exist over 20,000 MOFs that have been characterized,[70] and the field is rapidly growing. Thus far, MOFs have been systematically implemented for gas storage,[71] fluid separations,[72] sensing,[73] catalysis,[74] luminescence,[75] and photovoltaics.[76]

Specifically, Zeolitic Imidazolate Framework (ZIF-8) is a MOF structure comprised of zinc (metal node) and 2-methylimidazole (organic linker) that offers 11.4 Å cavities gated by 3.4 Å apertures.[77] With an optical band gap of 5.5 eV (λ = 225 nm)[78] this semiconductor framework is transparent in the visible region (380 nm to 740 nm)[79] which is a key optical property needed for suitable PSI encapsulation to ensure its photochemical functionality. Critically, ZIF-8 is set apart from the vast majority of other MOFs in that can be synthesized in water at room temperature and pH < 11,[80] whereas most MOF synthesis requires organic solvents, high pressure and temperature, or extreme acidic conditions. ZIF-8 is highly stable in a wide range of solvent conditions (aqueous, organic solvents, or high alkalinity),[77] and in temperatures over 200° C.[80] ZIF-8 is not stable in acidic environments as nitrogen members of the imidazole ring preferentially form N-H bonds, releasing the N-Zn bond. Past studies have demonstrated that ZIF-8 has the capacity to lend these harsh environment resistant properties to small proteins embedded inside them, thereby protecting them from denaturation under extreme conditions.[81-83] Specifically, encapsulated enzymes have been shown to retain and, in a small number of cases, even enhance their activities.[84-87] This enhancement is not yet fully understood, but has been attributed to the physical confinement of an active conformation and/or interactions between the active site and the metal nodes of the framework. Fundamental understanding on the effects of such MOF encapsulation on the functional behaviors of large membrane proteins is still an open question.

To this end, ZIF-8 could act as an ideal organic-inorganic scaffolding to protect PSI from harsh environments, while enabling fundamental investigations into the role of artificial confinements on the photoactivated properties of PSI. Such studies also contribute to the backbone of the ongoing research in our group towards unveiling the effects of microenvironment alterations on the photoactivities of PSI in an effort to design bio-hybrid photochemical energy conversion devices. Hence, we report ZIF-8 crystal structures grown via heterogeneous nucleation on PSI acting as the seeding agent, which allows us to encapsulate the photocatalytic protein within the zeolitic structure to create encaged PSI@ZIF-8 composites. Herein, we demonstrate that by doing so the PSI is protected from denaturing environments while retaining its photoactivity (redox transfers) within the ZIF-8 framework. In the broader context of the recent surge of research interests in this area, rational designs of such protective scaffoldings for PSI could provide the architectural framework much needed for preserving PSI activities when assembled onto bio-hybrid devices that can operate under harsh and extreme environments.

3.2 Experimental Section

3.2.1 Materials

Zinc acetate dehydrate (**ZnAc**, >99.0%), 2-methylimidazole (**Hmim**, 99%), sodium dodecyl sulfate (**SDS**, >99.0%), sodium L-ascorbate (**NaAsc**, >99.0%), sodium 2,6-dichloroindophenolate hydrate (**DCIP**, ACS grade), Triton X-100 (**TX100**, laboratory grade) were purchased from Sigma Aldrich. Monobasic and dibasic sodium phosphate (>99.0%), ethanol (**EtOH**, 100%), methanol (**MeOH**, >99.8%), methyl viologen hydrate (**MV**, 98%) were purchased from Fisher Scientific and n-dodecyl β-maltoside (**DDM**, >99%) was purchased from Glycon.

3.2.2 Methods

Growth of T. Elongatus and Preparation of Photosystem I

The thermophilic cyanobacterium *Thermosynechococcus Elongatus (T. Elongatus)* BP-1 was grown and extracted from thylakoids according to previously described methods.[41] The details of the extraction and purification of the trimeric PSI complex from the grown *T. Elongatus* cells are provided elsewhere,[112] with the following changes: lysozyme was not used, cells were broken using a Dyhydromatics microfluidizer reaction chamber, and the 26/700 mm XK ion-exchange column was packed with Toyopearl DEAE-650M resin. Based on spectrophotometer measurement of chlorophyll concentrations,[113] the concentration of the extracted PSI trimers is estimated to be around 54.0 × 10^{-6} mol L^{-1}. PSI trimers were stored in aliquots of 100 µL at -80°C for future use.

Synthesis of pure ZIF-8

A 15 mM aqueous solution of ZnAc was prepared by dissolving 0.0659 grams of ZnAc in 20 mL of deionized water. Separately, 2.463 grams of Hmim was dissolved in 20 mL of deionized water to generate a concentration of 1500 mM. The two solutions were then mixed in a 50 mL centrifuge tube, vortexed for 15 seconds, and placed in the dark at room temperature for 1 hour. The precipitate was collected by centrifugation at 5000-g for 5 minutes, then washed with deionized water and centrifuged again 3 additional times. Before the final spin, 5 µL of the suspension was deposited on a silica wafer for SEM imaging. The final precipitate was either suspended in pH 7.4, 50 mM sodium phosphate buffer or else dried overnight in vacuum for powder XRD analysis.

Synthesis of PSI@ZIF-8

To the previously prepared 15 mM aqueous solution of ZnAc, 4 mg of PSI was added. Then, this solution was mixed with the separately prepared 1500 mM aqueous solution of Hmim in a 50 mL centrifuge tube, the mixture was vortexed for 15 seconds, and placed in the dark at room temperature for 1 hour. This final mixture contained 7.5 mM ZnAc, 750 mM Hmim, and 0.1 mg/mL PSI. The precipitate was collected by centrifugation at 5000 x g for 5 minutes and either washed and dried, or a second cycle was initiated by re-suspending the precipitate in 20 mL of 1500 mM Hmim solution by vortexing. To this same tube was then added 20 mL of 15 mM ZnAc solution, vortexed for 15 seconds, and placed in the dark for 1 hour. In this way, the PSI was immersed in fresh ZIF-8 growth solution for a total of 3 times before being finally centrifuged and washed in DI water several times to be stored in pH 7.4, 50 mM sodium phosphate buffer.

UV-Vis Characterization

All spectral absorbance and fluorescence data presented were obtained on a BioTek Synergy H1 well plate reader at room temperature. Solutions of PSI were in pH 7.0, 50 mM sodium phosphate buffer and 2.2 CMC DDM. Solutions of PSI@ZIF-8 were in pH 7.0, 50 mM sodium phosphate buffer, except where noted. Release of PSI from PSI@ZIF-8 composites was achieved by adding pH 5.5, 100 mM sodium acetate solution and measuring fluorescence after 10 minutes of incubation. All fluorescence emission measurements were excited by 440 nm light.

Supernatant Analysis

To measure the successful PSI encapsulation in ZIF-8, an aliquot of the supernatant from the centrifuged PSI@ZIF-8 solution was taken and placed in a centrifuge tube and diluted to a 90% methanol solution. This was vortexed for 30 seconds, then centrifuged at 17000 x g for 3 minutes. Of this second supernatant, 300 µL was placed in a plate well for UV-Vis characterization. A chlorophyll assay was performed by reading absorbance at 664 nm and using previously established equations.[113] With a known total volume of the supernatant, the total amount of chlorophyll recovered was converted to PSI content compared to the total known amount of PSI added in the synthesis. Identical analyses were performed for the supernatants of PSI@ZIF-8 solutions that had been washed with 2% DDM, TX100, SDS or 75% ethanol.

LIBS Analysis of PSI@ZIF-8 Composition

Motivated by our recent success with laser-induced breakdown spectroscopy (LIBS) to make quantitative characterizations of intermetallic nanoalloys and nanocomposites,[114-116] thin films,[117] and biological samples.[118], we have used this technique to estimate the MOF-confined PSI contents by using the inherent Mg atomic emission signatures from PSI chlorophyll networks and Zn emission lines from the ZIF-8 frameworks. To the best of our knowledge, no prior works have used LIBS for quantitative estimation of protein contents in confined frameworks. In fact, many recent studies on MOF-confined proteins either have resorted to thermogravimetric analysis (TGA) or x-ray scattering techniques (SAXS) [86, 119] that are neither precise nor as robust as direct atomic emission spectroscopy techniques to provide quantitative estimations of protein contents.

Both the actual PSI@ZIF-8 composites as well as the standard samples of simple PSI/ZIF-8 mixtures used for calibration were directly deposited onto a substrate for LIBS analyses of the Mg signals from PSI in identical ZIF matrices. The LIBS experimental set-up is described in details elsewhere.[114, 117, 120] Briefly, it uses a Q-switched Nd-YAG laser of nominal wavelength 1064 nm operating at 200 mJ/pulse, and a pulse width of 8 ns (Make: Insight Model: 122551-R) to thermally ablate the samples to collect atomic emission signatures of the constituent analyte species. To improve statistical average for the signal intensity for each analyte of interest, spectral data over ~40 shots were collected. Mg I (285 nm) and Zn I (334.5 nm) emission lines were chosen from

NIST Atomic Energy Levels Data Center[121] based on the relative line strengths, and transition probabilities. Optimal accuracy and signal detections for the respective emissions were determined to be at 5µs gate delay and 20µs gate width. Based on these settings and a quantitative methodology reported in our earlier works,[114-115, 117-118, 122-124] a calibration curve for the intensity ratios of the Mg I (285 nm) to Zn I (334.5 nm) emission lines was constructed for PSI response signals in ZIF-8 matrix. Based on the calibration curve, the net PSI concentrations in the final PSI@ZIF-8 structures were calculated.

Scanning Electron Microscopy

All SEM images were taken with a Zeiss Auriga at 1 keV beam power.

Pump-Probe Spectroscopy

Formation and decay of P_{700}^+ was measured via pump-probe spectroscopy using a Bio-Logic JTS-100 system. Samples of PSI (with 2.2 CMC DDM) or PSI@ZIF-8 were suspended in a solution of pH 7.4, 50 mM sodium phosphate buffer. If 4 mM NaAsc is added to the samples and then left in the dark for 30 minutes, all previously present P_{700}^+ will be reduced. However, if in addition to the ascorbate, 0.002 mM DCPIP is added, the P_{700}^+ population is reduced in ~5 minutes. This facilitates multiple successive measurements on a sample with negligible effects on the observed kinetics in the 500 ms time window. Samples were excited with 2000 µE actinic light at 630 nm for 30 ms and probed at 810 nm. Subsequently, the measurement was repeated after adding 0.8 mM MV to the sample. Then, a final measurement was taken after adding 0.4 mM DCPIP to the solution.

3.3 Results and Discussion

3.3.1 PSI encapsulation in ZIF-8

The formation of PSI@ZIF-8 particles was achieved through multiple coating cycles, as described in the methods section and depicted in Figure 3.1. While multiple other enzymes have been embedded in ZIF-8 through a one-pot method in the past, the large transmembrane protein (~22 nm diameter x 10 nm height) PSI presents particular challenges. Previous works have successfully embedded highly water soluble enzymes such as cytochrome c (12 kDa),[86] bovine

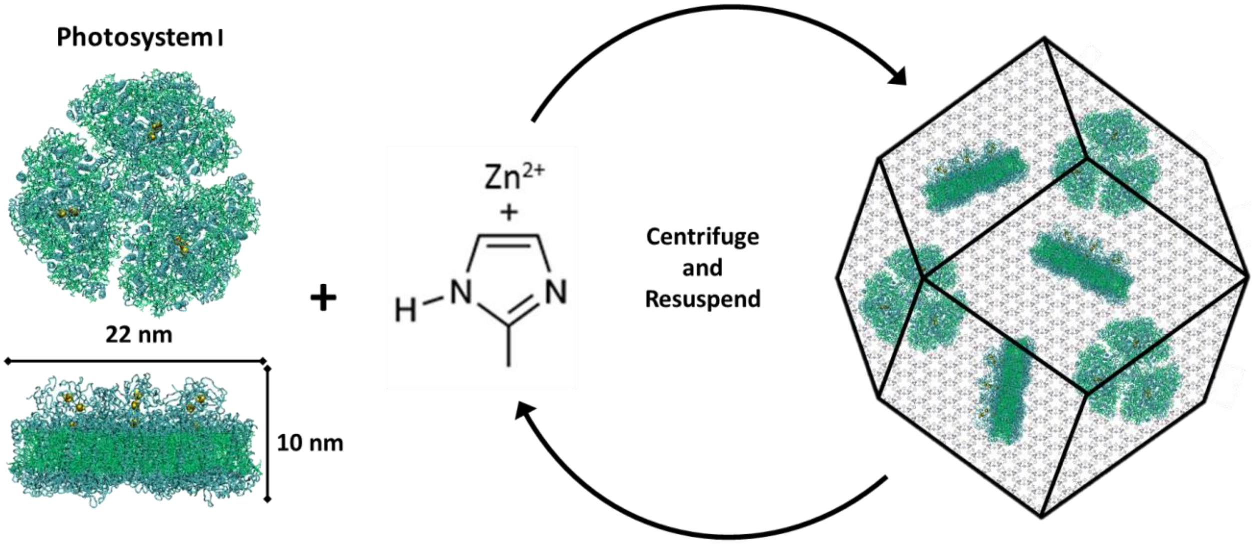

Figure 3.1 Top and side views of the trimeric photosystem I (left); a schematic of the synthesis procedure for PSI@ZIF-8 composites, whereby PSI is combined with zinc (Zn^{2+}) acetate and 2-methylimidazole (Hmim), incubated to induce nucleation and crystal growth, and then finally centrifuged and resuspended in fresh reactants to further coat PSI in the ZIF-8 framework.

hemoglobin (64.5 kDa),[125] and urease (90 kDa),[126] while PSI (1068 kDa) is an order of magnitude larger than any protein structure integrated in ZIF-8 thus far. It contains a uniquely coordinated chlorophyll network and, as a membrane-bound protein, exhibits contrasting hydrophobic/hydrophilic regions that promote non-uniform heterogeneous nucleation of ZIF-8 on its surface. Here, one needs to bear in mind that high concentrations of Zn and high Hmim:Zn ratios can yield faster nucleation of smaller particles, rapid growth, and high-purity ZIF products. However, if self-nucleation is too fast, much of the PSI is not encapsulated in the framework and remains only surface-bound. In fact, the hydrophobic surface of ZIF-8 strongly and readily binds the protein. Figure 3.2a shows the as-synthesized pure ZIF-8 crystals which rapidly bind over 99% of the PSI subsequently added, as measured by a chlorophyll assay of the supernatant. It should be mentioned that when washed with gentle surfactants such as DDM or TX100, no measurable amounts of PSI were released. However, 96% of the surface-bound PSI was removed upon using harsh denaturing detergents such as SDS, while a subsequent ethanol wash removed the remaining 4%. Figure 3.2b provides the visual support for these phenomena.

In addition to excluding PSI from full encapsulation, fast nucleation also creates a dense solution of highly concentrated ZIF-8 nanoparticles that scatter light, thereby blocking the light and preventing any effective photoactivity measurements. Previous published works with embedded enzymes have been unconcerned about light scattering since most enzymes function perfectly in the dark, avoiding the need for such optimization.[126-127] Hence the choice of low Zn concentration, high Hmim:Zn ratio of 100:1, and multiple coating cycles promote PSI surfaces to be the primary nucleation sites. The corresponding XRD plots for pure ZIF-8 and PSI@ZIF-8 in Figure 3.3a confirm that the PSI@ZIF-8 composites fabricated under these conditions form highly crystalline ZIF-8 around PSI. Additionally, as described in our method section earlier, LIBS technique was employed to extract the quantitative information on the amount of PSI (by % wt.) confined within the ZIF-8 frameworks. Figure 3.3b shows the representative Mg I (285 nm) and Zn I (334.5 nm) atomic emission lines collected from the as-prepared PSI@ZIF-8 composites immobilized on substrates, and indicating the strong chlorophyll signals (Mg) emanated from the PSI@ZIF-8 composites. Based on these Mg and Zn emission lines, the calibration curve generated in Figure 3.3c clearly shows the linear correlation ($R^2 = 0.983$) for the normalized emission intensity ratios (I_{MgI}/I_{ZnI}) as a function of PSI concentrations for the various PSI/ZIF-8 mixtures (see methods section). Based on this calibration curve and the Mg I and Zn I signals collected from

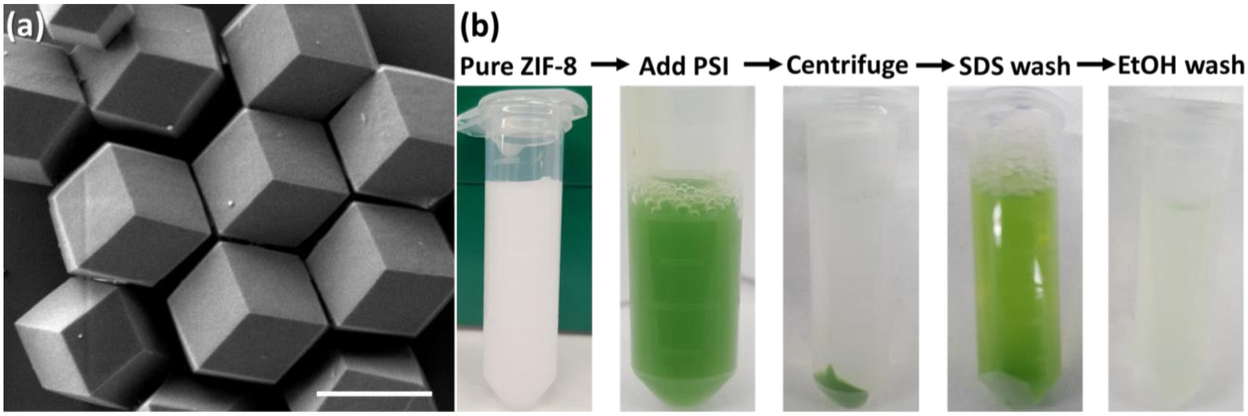

Figure 3.2 (a) SEM image of synthesized pure ZIF-8 crystals (scale bar 1 μm); (b) snapshots of a sequence that shows that PSI binds quickly and strongly to the ZIF-8 surface that can only be removed by using harsh denaturing surfactants while the remaining chlorophyll is removed using an organic solvent.

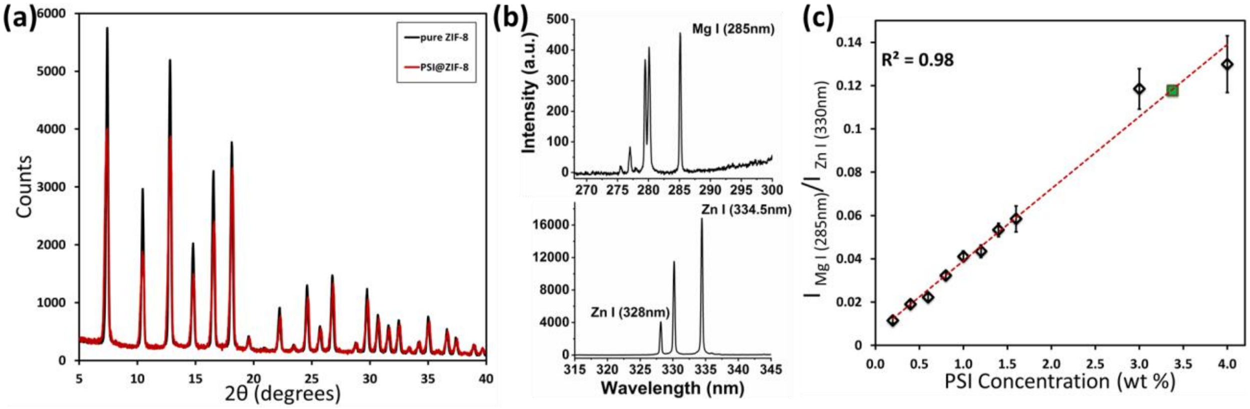

Figure 3.3 (a) XRD plot for pure ZIF-8 and the embedded PSI@ZIF-8 indicates high crystallinity and corresponding lattice peaks for the composite material; (b) LIBS atomic emission signals as collected from the substrate immobilized PSI@ZIF-8 composites for Mg I (285 nm) from the chlorophyll networks and Zn I (334.5 nm) from the ZIF-8 frameworks; (c) calibration curve indicating the normalized intensity ratios ($I_{\mathrm{Mg\,I}}/I_{\mathrm{Zn\,I}}$) as a function of PSI concentrations (% wt) generated from various PSI/ZIF-8 mixtures and the final composition of PSI@ZIF-8 after 3 cycles (green).

the PSI@ZIF-8 composites, our calculations reveal the PSI content embedded within the ZIF-8 framework to be 3.4% by weight. It should also be noted that owing to the ZIF framework flexibility, we had posited that it would take at least a ~10 nm shell thickness of ZIF-8 around each PSI trimer to form a secure barrier against solvent denaturation. Assuming ZIF-8 density[77] of 0.95 g cm^{-3}, the calculated 3.38% by weight of PSI in the final composite corresponds to roughly an average of ~13 nm of ZIF-8 shell surrounding each PSI trimer. While this corroborates our hypothesis, the nature of the multi-cycle coating means that the actual thickness from the ZIF-8 surface to the first embedded PSI may be greater.

Figure 3.4 shows the role of successive cycles of ZIF-8 coating in creating larger crystal faces and aggregates of PSI@ZIF-8 particles that provide much more complete and robust protection from external harsh solvents. To prove this, Figure 3.4 also demonstrates the supernatant color (green) after a series of SDS and ethanol washes for the PSI@ZIF-8 composites made with 1, 2 and 3 cycles of coating. The SDS molecules (~15 Å length) are size excluded by the much smaller 3.4 Å ZIF-8 pores. Therefore, any PSI which is broken apart and removed by SDS (indicated by the green colored supernatant) must have been either surface bound or accessible through large mesopores and defects. As seen from Figure 3.4, a single cycle shows PSI removed by both SDS and ethanol, while a second cycle shows protection from SDS but not from ethanol, which is known to diffuse readily through ZIF-8 pores.[128] The green EtOH supernatant indicates the presence of mesopores large enough for ethanol to disrupt the protein structure and release chlorophyll. Only after three cycles of ZIF coating do we observe that the PSI is substantially protected, where less than 1% removed after washing with both SDS and ethanol. Successive coating cycles enhance the coverage and framework integrity such that even if PSI@ZIF-8 is exposed to otherwise denaturing solvents, the tortuosity of the porous framework sterically hinders any disruption of the structure and removal of chlorophyll. Thus, we were able to confirm the complete encapsulation of PSI in ZIF-8.

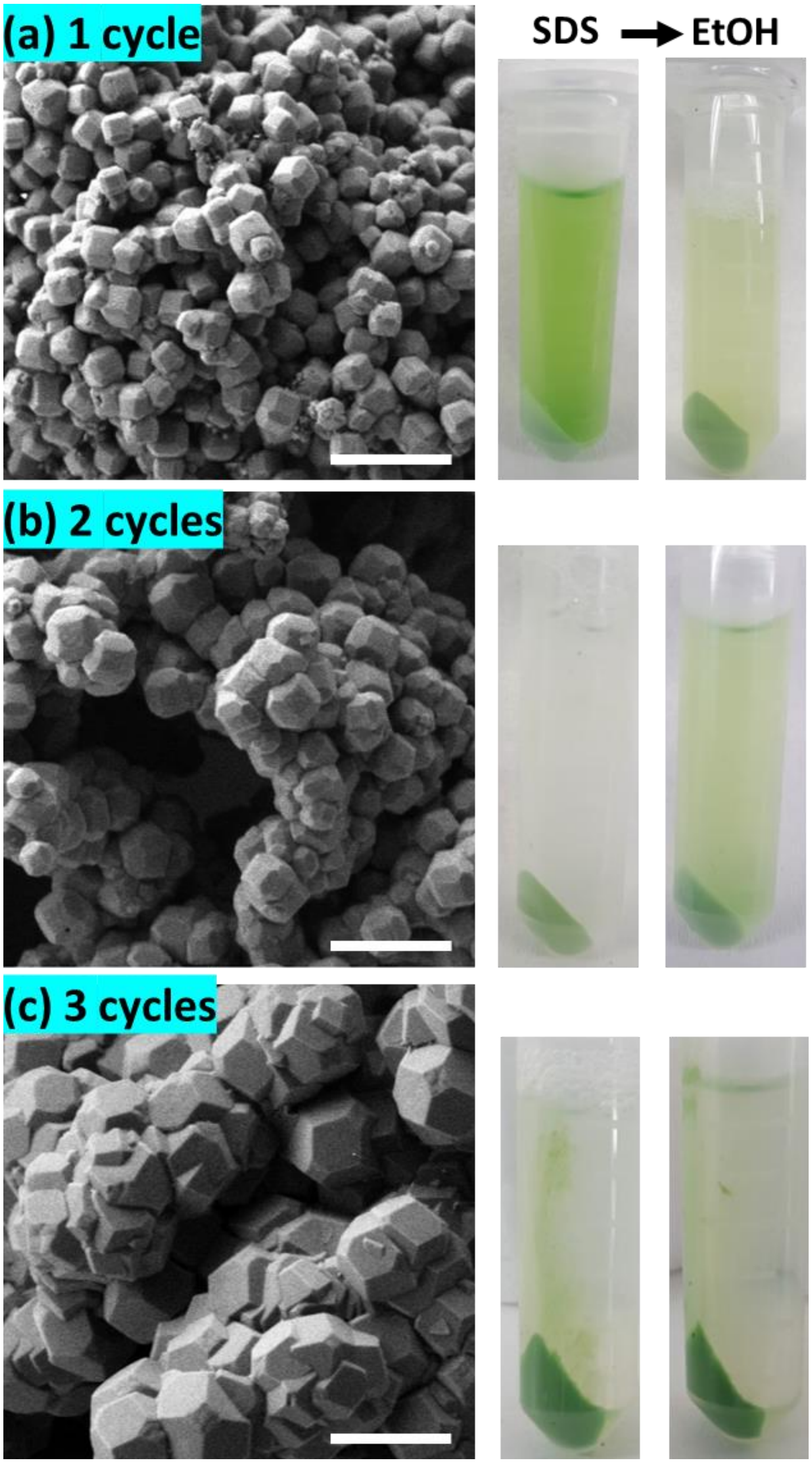

Figure 3.4 SEM images of PSI@ZIF-8 coated with 1, 2 and 3 cycles of ZnAc and Hmim treatments (scale bar 1 μm). Corresponding samples which have been washed with SDS and then with ethanol are pictured on the right of each case; (a) 1 cycle leaves PSI accessible to both SDS and EtOH; (b) 2 cycles protect PSI from SDS but not from a smaller organic solvent like EtOH; (c) 3 cycles protect PSI from both, where EtOH removes less than 1% of the original PSI content.

3.3.2 Optical properties of PSI@ZIF-8

Typically, PSI has two characteristic absorption peaks at ~440 nm and 680 nm. It is well known that the absorption response differences between chlorophylls contained within PSI and free chlorophylls result from both the presence of a small number of carotenoids and the unique conformational coordination of the chlorophyll network in PSI. The roles of steric confinement and local chemical environments in tailoring the conformational changes in the chlorophyll network are of great interest for fundamentally understanding photosynthetic mechanisms. Our group has previously found shifts in both absorbance and fluorescence peaks when PSI is confined within fully organic lipid bilayer environments.[129] To investigate such effects, Figure 3.5 shows the absorption spectra for pure PSI (green), pure ZIF-8 (gray), and the PSI@ZIF-8 hybrid material (blue). Due to the significant scattering of the ZIF nanoparticle suspensions, manual subtraction of a ZIF-8 background was performed to reveal the underlying contribution of the embedded PSI in the PSI@ZIF-8 composites (red). The red absorption peak slightly blue shifted from 680 nm to 676 nm, which is comparable to the shift found previously. The most likely explanation for this shift is exposure to the alkaline conditions (pH ~11) during ZIF-8 synthesis. A similar shift is observed from PSI in a solution of 1 M Hmim after 2 hours. No such blue shift is observed in the blue region, where the 440 nm peak remained unchanged.

The fluorescence emission data reveals an even more pronounced shift and variations in the peak wavelengths as seen from Figure 3.6a. When excited at 440 nm, PSI trimers fluoresce at 720 nm. When embedded, PSI@ZIF-8 fluoresces with a much higher intensity at a significantly blue shifted peak of 676 nm. Interestingly, this is also in agreement with previously reported confinement effects in PSI-proteoliposomes.[129] However, what creates the confusion in attributing this distinctive shift to the confinement effects is that this emission profile appears uncannily similar to that of uncoupled chlorophyll (i.e., when PSI is denatured by 2% SDS as seen in Figure 3.6b or by 75% ethanol as seen in Figure 3.S3 in the Appendix). In our effort to confirm if the synthesis procedure might have damaged the chlorophyll network, PSI@ZIF-8 composites are incubated for 10 minutes in pH 5.5 sodium acetate buffer solution (described in methods section for UV-Vis characterizations). This has been demonstrated previously to release encapsulated targets in ZIF-8 by dissolving the MOF frameworks that readily break down under acidic conditions.[81, 130] Here, we clearly observe that the fluorescence profile after the acid treatment matches that of free PSI trimers, confirming that the ZIF-8 encapsulation process successfully

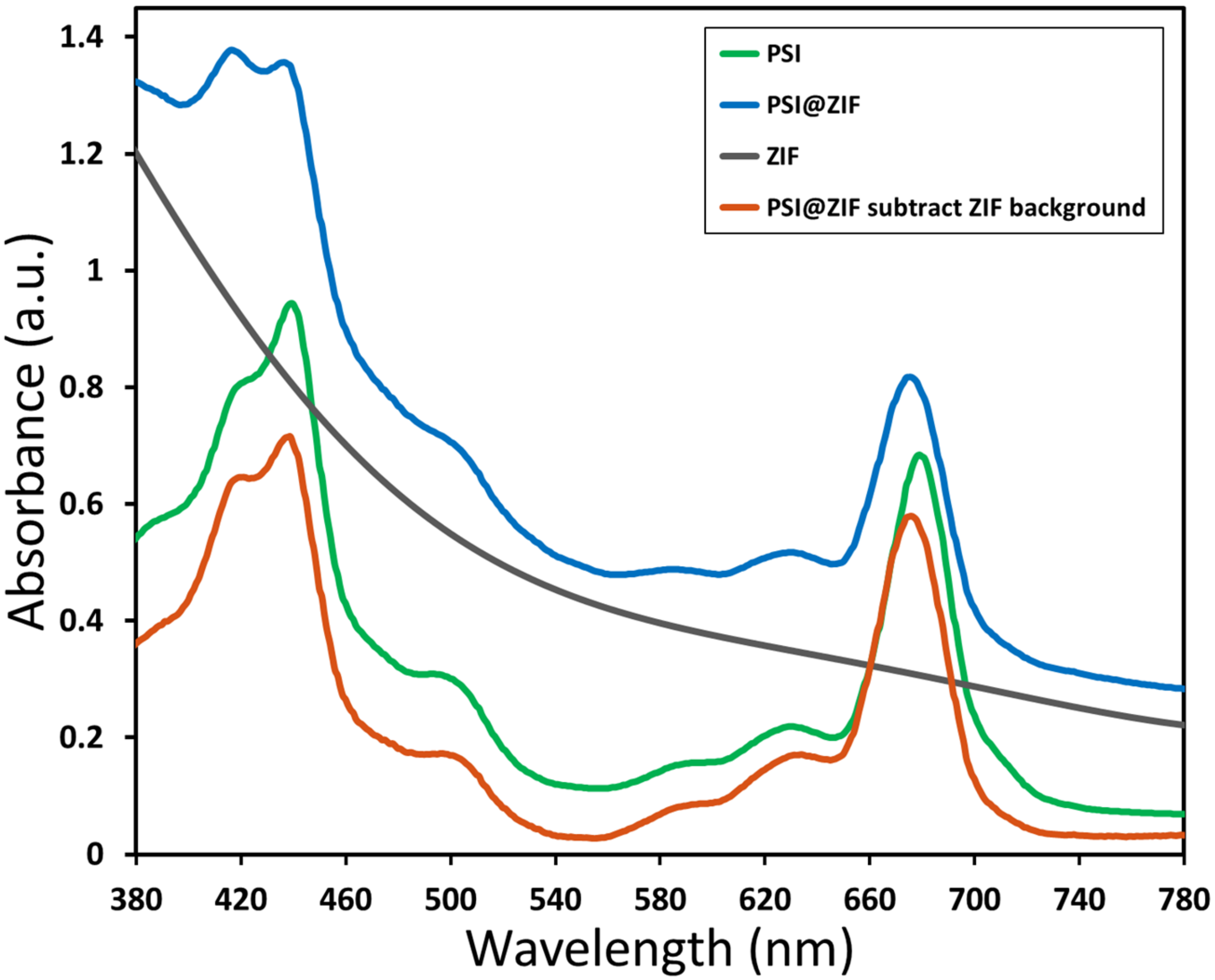

Figure 3.5 Absorbance data for free PSI (green), pure ZIF-8 (gray), and PSI embedded in ZIF-8, *i.e.* PSI@ZIF-8 (blue) in solution. A manual subtraction of the scattering background reveals a blue shift in the absorbance peak for PSI@ZIF-8 (red) from 680 nm to 676 nm.

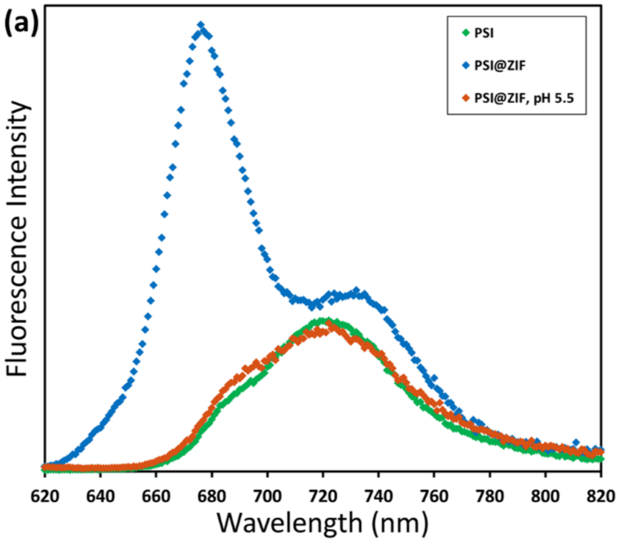

Figure 3.6 Room temperature fluorescence emission (excitation 440 nm) of variously treated PSI samples. (a) Free PSI (green) with a peak at 720 nm; when confined in ZIF-8 this shifts to 676 nm (blue); exposing to acidic conditions releases the PSI, whereupon the fluorescence profile returns (orange). Comparatively, (b) PSI denatured by using SDS has the characteristic emission at 680 nm of uncoupled chlorophyll, which is amplified by a further breakdown under acidic conditions.

preserves the protein and the chlorophyll network structure until released by the breakdown of the MOF structures around them. One needs to bear in mind that SDS does not only pull PSI apart into monomers, but it denatures the constituent subunits, thereby decoupling the chlorophylls. Similarly, exposing this denatured PSI to acidic conditions only further accelerates the breakdown process (as also clearly seen from Figure 3.6b).

In order to verify that PSI trimers are not significantly damaged or altered by the very presence of ZIF-8 structures, ZnAc, Hmim, acidic solutions, we carried out systematic control experiments whose results can be found in the supplementary information (Figures 3.S4 and 3.S5 in the Appendix). These stringent controls clearly indicate that: 1) the ZIF-8 framework alone has no fluorescence emission in this region, and 2) ZnAc, imidazole, or acidic solution ranging from pH 5.5 to 6.5 separately has minimal to no effects on the regular PSI fluorescence emission profile. Specifically, the PSI in acidic buffer solutions in Figure 3.S5 (Appendix) show decreasing fluorescence signal with decreasing pH level as Mg^{2+} ions are dechelated from the chloropyll molecules, but the characteristic peak location is unchanged. This further corroborates our observations that even when the ZIF-8 structure breaks down in pH 5.5 solution to release the encapsulated PSI, the trimeric complexes by themselves remain unaffected as reflected by the return of the emission profile to the original PSI signature in Figure 3.6a.

Consequently, we can confidently conclude that the emission peak and intensity shift is a distinct outcome of the microenvironment alterations due to the PSI confinement within the ZIF framework. At this stage, we hypothesize that such variations in the emission profile are possibly due to a combination of conformational changes in chlorophyll network from the steric hindrance that tunes the vibrational modes as well as the electronic or vibronic coherences due to interactions between the framework environment and the chlorophyll network. It needs to be pointed out that it has recently been shown that a single chromophore embedded in a variety of different metal organic frameworks yielded unique fluorescence changes (both red and blue shifts) depending on the topology and chemistry of the framework.[131] Similarly, green fluorescent protein (GFP) has been investigated by utilizing its fluorophore HBI as both an occupant in a MOF[132] and as a structural component of one.[133] Such studies point toward the complex interplay of the local chemical environment, electronic coordination, and steric hindrance affecting light absorption and emission behavior. In an effort to gain a fundamental understanding of these coherent/incoherent interactions, our current ongoing efforts are systematically directed towards divulging and separating the intricate roles of microenvironment structure and chemical composition in driving such energetic interactions/coupling which we believe is crucial for understanding, utilizing, and developing artificial photosynthetic systems which aim to coordinate multiple chromophores.

3.3.3 Photoactivity of PSI@ZIF-8

While encapsulation and protection of PSI in the ZIF-8 structures are confirmed from the earlier sections, the critical questions that remain unanswered at this stage are: 1) Is the charge separation pathway still active within the PSI in the PSI@ZIF-8 composites? And 2) are both the terminal electron acceptor F_B^- and the primary electron donor P_{700} accessible to suitable mediators for electron transfer? To this end, in this section we present pump-probe spectroscopy performed with excitation at 630 nm (pump) and measurements at 810 nm (probe) that effectively measures the creation and decay of the P_{700}^+ population. Because the samples were exposed to light and oxygen (which can scavenge electrons from F_B^- directly)[29] during synthesis and handling, they were incubated in the dark with ascorbate to eliminate any P_{700}^+ already present; the ascorbate donor exhibits slow kinetics and reduces P_{700}^+ on a timescale orders of magnitude slower than PSI charge recombination.

The first measurement in Figure 3.7a (purple line) exhibits only the decay of P_{700}^+ population due to charge recombination from F_B^- to P_{700}^+. Exponential decay fits (green overlay) reveals a characteristic decay time, $\tau = 89$ ms, which is in good agreement with previously reported recombination rates that can vary from 30 ms to 100 ms.[134-135] When methyl viologen (MV) is added (orange line, red fit), a long-lived P_{700}^+ population is observed because MV scavenges the electron from F_B^- and prevents recombination, thereby maintaining a constant population of P_{700}^+. Finally, when additional DCPIP is added (blue line, gray fit), this electron donor efficiently reduces P_{700}^+ faster than F_B^- reduces MV. The entirety of all calculated decay times can be found in the supporting information Table 3.S1 (in Appendix); it should be noted that because the donation of electrons from DCPIP to PSI is a second order reaction dependent on both concentrations and clearly taking place in a diffusion-controlled regime, the calculated decay time is essentially arbitrary. That is, the match between the decay times with Asc alone and with Asc, MV, and DCPIP is rather a coincidence, where shifting the concentration of DCPIP up or down also shifts the observable decay time. The 2 to 3-fold increase in amplitude of the decay rate is indicative of the electron donation process over the previously inhibited recombination. Thus, we can observe

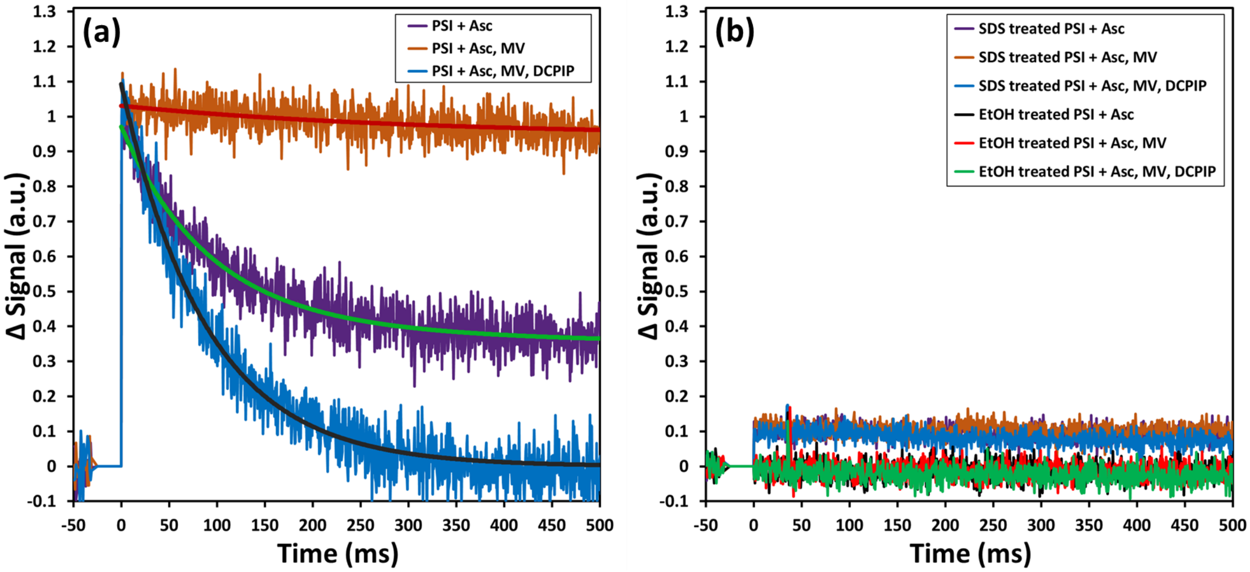

Figure 3.7 Pump (630 nm)–probe (810 nm) data for solubilized PSI indicate that: (a) charge recombination from F_B^- to P_{700}^+ is seen in the presence of ascorbate (purple) due to the slow kinetics of this donor. Addition of methyl viologen (orange) scavenges electrons and maintains the P_{700}^+ population. The subsequent addition of DCPIP as a donor reduces P_{700}^+ at relevant timescales; (b) if the chlorophyll network is disrupted by denaturing agents such as SDS detergents or ethanol, no P_{700}^+ is formed at any time.

intrinsic charge separation as well as charge transfer at both the lumenal and stromal sides of free PSI in solution. As expected, if PSI is exposed to SDS or ethanol (Figure 3.7b), the chlorophyll network is completely disrupted, thereby removing the possibility of P_{700}^+ generation at any point. Figure 3.8a shows the same sequence of pump-probe measurements for the PSI@ZIF-8 composites. It can be clearly observed that the decay trends (recombination $\tau = 95$ ms) for the composites are comparable to the respective cases observed for free PSI in solution. This demonstrated that not only is the characteristic charge separation maintained, but also both mediators can access the F_B^- and P_{700}^+ terminals for charge transport to and from PSI. The latter observation is noteworthy because MV and DCPIP are larger than the 3.4 Å ZIF-8 pore sizes. Both MV and DCPIP are linear molecules with relevant widths comparable to that of benzene, which has a kinetic diameter of 5.85 Å.[136] Despite this larger size, benzene and even trimethylbenzene are seen to diffuse through ZIF-8,[137] testifying to the flexible nature of the gating apertures.[138] While large enough molecules can be shown to be truly size excluded,[139] the exact cut-off is still unknown due to this framework flexibility. Because total electron transport through PSI is diffusion limited, there is still significant need for studies into the underlying mass transport properties of these larger molecules before we can understand how this confinement affects the electron transport kinetics of PSI.

Furthermore, Figure 3.8b and 3.8c also show the respective pump-probe signal decay profiles for the P_{700}^+ population for the PSI@ZIF-8 composites exposed to SDS and ethanol (EtOH) respectively. Thus, PSI@ZIF-8 maintains the familiar activity after exposure to SDS (Figure 3.8b), which is plausibly limited to only accessing the PSI on the ZIF surfaces or, through large mesopores. More excitingly, what we observe is that even exposure to a smaller molecule with a high uptake and large diffusion coefficient like ethanol[137] (Figure 3.8c) does not inhibit this charge transport process. Because of the large size of PSI compared to other enzymes and its precisely positioned chlorophyll network that is not covalently bonded, we anticipated that it might be vulnerable to ethanol that readily disrupts the protein structure to dislocate the chlorophyll network of free PSI and is known to rapidly diffuse through the ZIF-8 framework. However, our results clearly indicate that even after exposure to such organic solvents, the photoactivity of the PSI@ZIF-8 composite is preserved, indicating the tight steric hindrance that locks the conformation in place and prevents any disruption of the chlorophyll network.

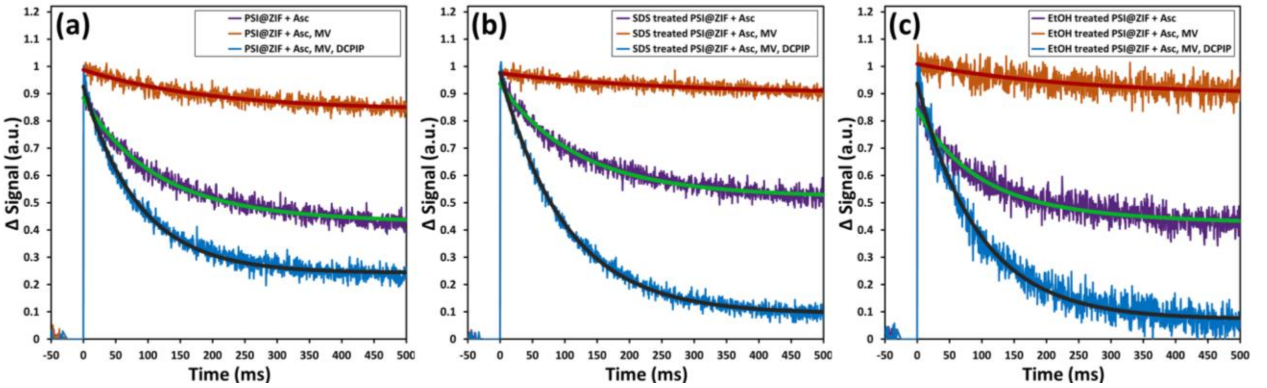

Figure 3.8 Pump (630 nm)–probe (810 nm) data for PSI@ZIF-8 composites demonstrate that: (a) even when fully encased by the ZIF-8 framework, MV and DCPIP are able to diffuse through to reach the stromal and lumenal sides of PSI, (b) this activity is maintained after exposure to the denaturant SDS, which is excluded by the small pore size, and (c) even after exposure to ethanol, which is known to denature PSI and can get transported readily through the framework pores, PSI and its chlorophyll network are not disrupted and maintain their full activity.

3.4 Conclusions

We have demonstrated the first-ever successful encapsulation of the supramolecular photosynthetic protein, PSI (~1000 kDa size) in a metal organic framework, ZIF-8. We find that the large, membrane-native PSI initiates nucleation of ZIF-8 on its surface, while subsequent coatings of ZIF-8 reactants fill in the ZIF mesopores to complete the coverage of the protective framework. Our results indicate that the as-fabricated PSI@ZIF-8 composites exhibit significant blue shift and intensity enhancements in their fluorescence emissions, when compared to that for native PSI, owing to their confinements inside the hybrid crystalline frameworks of ZIF-8. We have also successfully shown that this encapsulation preserves the PSI structure while protecting it from harsh denaturing conditions. To this end, we have demonstrated through systematic visual inspections as well as detailed pump-probe experiments that harsh detergents such as SDS are prevented from accessing the embedded PSI through the small ZIF-8 pores, while organic solvents such as ethanol is able to access the framework interiors but, unable to disrupt the chlorophyll network due to steric hindrance.

Finally, our solution-phase pump-probe experiments have established that the unique light-activated charge separation facilitated by PSI's chlorophyll networks and electron transport pathways remain unaffected in the PSI@ZIF-8 composites, thereby indicating that the mediators MV and DCPIP are able to diffuse through the framework to scavenge and donate electrons from and to PSI. Further investigations are required and are currently underway in our group to quantify the macro-scale diffusion kinetics of these mediators and understand the complex charge transport processes within these hybrid frameworks. In summary, our first successful encapsulation of transmembrane photoactive proteins within MOF scaffolds lays the fundamental groundworks for robust design of organic-inorganic interfaces in bio-hybrid photoactive materials that can be functional under otherwise incompatible conditions for future photochemical solar fuel conversions.

CHAPTER 4

AUGMENTED PHOTOCURRENTS FROM PHOTOSYSTEM I EMBEDDED IN ZINC AND IMIDAZOLE BASED TCNQ CHARGE TRANSFER SALT FILMS DERIVED FROM ZIF-8

4.1 Introduction

Photosynthesis harnesses the bountiful solar energy and converts it to usable forms for sustaining all the life on this planet. Photosystem I (PSI) is one of the primary biomolecular machines responsible for driving this solar conversion. It is a chlorophyll-rich transmembrane protein complex, which drives the light-activated charge separation and subsequent electron transport of photosynthesis in plants and bacteria. In the cyanobacterium *Thermosynechococcus Elongatus*, membrane bound PSI exists in trimeric form and weighs 1068 kDa.[6-7] This biological photodiode shuttles electrons from the lumenal side (P_{700}^{+}, $E_m = +490$ mV) to the stromal side (F_B^{-}, $E_m = -530$ mV) of PSI with nearly 100% quantum efficiency.[7] The remarkable photoactivated charge separation properties of PSI, being active over the broad visible spectrum of light, have resulted in a long history of intense scientific studies, both to understand its fundamental biophysics and to integrate it into bio-hybrid photochemical and optoelectronic devices.

The photoelectrochemical activities of PSI have previously been studied through investigations of PSI monolayers immobilized on various conducting substrates: gold electrodes,[28-32] carbon nanotubes,[15, 33-34] metal oxide nanowires,[35] or plasmonic nanostructures.[36-38] Despite the fundamental insights gained from such works, a significant barrier for large photocurrent generation has been the weak optical absorption of a single PSI monolayer (only 0.34% of incident light at 680 nm).[53] To this end, one can surmise that an appreciable generation of photoresponse from PSI might require much higher effective light absorption cross-sections.

To mitigate the aforementioned problems, multi-layer assembly techniques have been increasingly pursued by various research groups that involved adding them to suitable beneficial substrates such as p-doped silicon,[55] and graphene,[23, 56-57] or creating thin film structures to stabilize as well as enhance PSI charge transport. Such implemented constructs have included mesoporous electrodes,[20] hydrogels,[50] conductive polymers,[58-60] polymer micro-particles,[140] and DNA binders with complementary enzymes.[61] In recent years, a specifically intriguing approach towards such efforts has been to confine PSI encapsulated in synthetic lipid membrane bilayers[62, 64-65] that mimic the native PSI thylakoid membrane. To this end, our recent works have shown considerable alterations in the photochemical and optical responses along with significant photocurrent enhancements due to the lipid bilayer mediated PSI microenvironment alterations.[65, 141-142] Thus, whether by introducing more favorable redox steps, greater functional surface area, or more complete conduction pathways, such efforts have continuously pushed the frontiers of biohybrid photovoltaics or photochemical energy conversion routes.

In this chapter we propose a new approach which may increase the options for all three of those fronts, through the formation of a TCNQ-based charge transfer salt. TCNQ, or 7,7,8,8-tetracyanoquinodimethane, is well known as an extremely strong organic electron acceptor, with an electron affinity of 2.88 eV,[88] and its anion $TCNQ^-$ is known to rapidly form stable charge transfer salts with almost any cation, whether metallic[89] or organic[90-91] in nature. In addition, it has two favorable redox peaks (-185 and +445 mV vs NHE)[92] for interacting with both the stromal (-530 mV) and lumenal (+490 mV) sides of PSI. The coordination of TCNQ with transition metal cations or organic ligands can form a large number of various morphologies, including coordination polymers,[91] metal-organic frameworks (MOFs),[93] and crystalline salts.[94] These complexes are almost all insoluble in both polar and nonpolar solvents,[95] thereby lending them the much-desired stability in a variety of environments and applications. Towards this end, they have found applications in the catalysis of electron transfer reactions,[96] as well as electrical, optical, and molecular switching, field emission devices. Specifically, certain organic complexes have high enough electronic conductivities to be considered fully organic metals, such as the well-known TTF-TCNQ salt.[97]

Herein, inspired by our successful encapsulation of PSI in ZIF-8 (PSI@ZIF-8)[98] we report the use of PSI@ZIF-8 composites as starting scaffolding materials to drive the constituent cations (namely, Zn^{2+} or the imidazole ion, H_2mim^+) from ZIF-8 towards subsequent formation of charge transfer complexes with TCNQ. While it has recently been demonstrated that a copper-based MOF can undergo ligand substitution to form CuTCNQ,[99] our work enables a transformation in an aqueous environment amenable to a host of biological materials rather than organic solvent. We demonstrate that the bound PSI remains embedded in the newly coordinated and conductive polymer network, which, in turn, allow significant augmentation in the photocurrent generation. We also show that the aforementioned cations can be reversibly exchanged in aqueous solution via electrochemical treatments to change both the composition and morphology of the TCNQ-based complex, which offers a myriad of future opportunities for successful integration of this unique class of charge transfer salt complexes with biological catalysts and light harvesters.

4.2 Experimental

4.2.1 Materials

Zinc acetate dehydrate (**ZnAc**, >99.0%), 2-methylimidazole (**Hmim**, 99%), acetic acid (**HAc**, 99.7%) were purchased from Sigma Aldrich. Monobasic and dibasic sodium phosphate (>99.0%), methyl viologen hydrate (**MV**, 98%), lithium iodide (**LiI**, 99%), 7,7,8,8-tetracyanoquinodimethane (**TCNQ**, 98%), acetonitrile (ACS grade) were purchased from Fisher Scientific and n-dodecyl β-maltoside (**DDM**, >99%) was purchased from Glycon. ITO coated glass slides (25mm x 50mm, TIX002) were purchased from TechInstro.

4.2.2 Methods

Growth of *T. Elongatus* and Preparation of Photosystem I

The thermophilic cyanobacterium *T. Elongatus* BP-1 was grown and extracted from thylakoids according to previously described methods.[41] The details of the extraction and purification of the trimeric PSI complex from the grown *T. Elongatus* cells are provided elsewhere.[112] Similar protocols were used here except for the following changes, namely: lysozyme was not used, cells were broken using a Dyhydromatics microfluidizer reaction chamber, and the 26/700 mm XK ion-exchange column was packed with Toyopearl DEAE-650M resin. Based on spectrophotometer measurements of chlorophyll concentrations,[113] the concentration of the extracted PSI trimers was estimated to be around 54.0×10^{-6} mol L^{-1}. PSI trimers were stored in aliquots of 100 µL at -80°C for future use.

Synthesis of LiTCNQ

The organic-inorganic salt complex LiTCNQ was prepared using a previously established procedure[143] with slight alterations. A solution of 1000 mL acetonitrile was brought to 80°C under continuous stirring on a hot plate. 100 mL of this was taken out and added to a beaker with 20 grams of LiI. In the remaining 900 mL of the original solution, 10.2 grams of TCNQ was added. Once both solids were completely dissolved, the 100 mL containing 20 grams LiI was added back to the 900 mL containing 10.2 grams TCNQ (the final concentrations were thus 50 mM of TCNQ, 150 mM of LiI), covered, and left stirring at 80°C for 12 hours. The purple precipitate was collected by repeated centrifugation at 5000x g and washed with fresh acetonitrile until the supernatant turned from a bright green to a pale green. The solid was then dried in vacuum and stored in a sealed glass vial.

Synthesis of PSI@ZIF-8

A 50 mM aqueous solution of zinc acetate was prepared by dissolving 0.439 grams of ZnAc in 40 mL of deionized water. Separately, a 2000 mM solution of 2-methylimidazole was prepared by dissolving 6.568 grams of Hmim in 40 mL of deionized water. In a 2 mL microcentrifuge tube, 76.7 µL DI water, 60 µL ZnAc solution, 13.3 µL PSI stock solution, and 150 µL Hmim solution were combined. The final volume was approximately 300 µL with final concentrations being 2.5 µM PSI, 10 mM ZnAc, 1000 mM Hmim. This solution was vortexed for 15 seconds and placed in dark at room temperature for 1 hour. The precipitate was collected by centrifugation at 3000 x g for 5 minutes, then washed and centrifuged in DI water for 3 times.

Conversion of PSI@ZIF-8 into PSI-Zn-H2mim-TCNQ

A 15 mM aqueous solution of LiTCNQ was prepared by dissolving 0.0317 grams of LiTCNQ in 10 mL of deionized water, which had been purged with nitrogen gas. A 15 mM aqueous solution of acetic acid was prepared by dissolving 34.35 µL of pure HAc to 40 mL of DI water. After the final centrifugation step of the previously prepared PSI@ZIF-8, 850 µL of LiTCNQ solution was added and vortexed for 1 minute until thoroughly mixed. To this suspension was then added 500 µL of the 15 mM HAc solution which was followed immediately with vortexing for 1 minute. This solution contained approximately 7.5×10^{-4} µmol PSI, 3 µmol ZIF-8, 7.5 µmol HAc, and 12.75 µmol LiTCNQ. After 5 minutes, the precipitate was collected by centrifugation at 3000x g for 5 minutes, then washed and centrifuged in DI water for 3 times. After the final wash, the precipitate was suspended in 1 mL of DI water, and 100 µL was pipetted onto an ITO slide then dried in vacuum for subsequent testing.

Electrochemical Analysis and Treatments

All electrochemical measurements and reactions were conducted using a potentiostat from Bio-Logic (Model: SP-300) operated using the EC-Lab software. Working electrode ITO slides were secured in a custom acrylic electrochemical cell (working area 1.267 cm^2) with three-electrode configuration that carried a Pt wire counter electrode, the SCE reference electrode (BAS Inc.; Model:

EF-1352 with a reference shift of +248 mV *vs.* SHE). Cyclic voltammetry was performed using a scan rate of 50 mV/s in a window from -350 mV to +300 mV in 100 mM ZnAc solution. All chronoamperometry measurements were performed in DI water with 4 mM MV as electron scavenger and 100 mM ZnAc as background electrolyte, at open circuit potential, which varied based on sample composition but was approximately -30 mV vs SCE. Electrodes were illuminated by a red LED (Thorlabs, model M660L4) with light intensity 300 W/m^2 in 30 second intervals.

LIBS Analysis of PSI@ZIF-8 Composition

Laser-induced breakdown spectroscopy (LIBS) was used to provide a qualitative estimation of the compositions of the various organic/inorganic complexes, PSI and the final charge transfer salts from the standard atomic emission lines of C, inherent Mg signatures from PSI chlorophyll networks, and Zn from the ZIF-8 frameworks. The LIBS experimental set-up and procedure have been described in details elsewhere for PSI@ZIF-8 as well as for diverse biological and nanomaterial compositions.[98, 114, 116-117, 120, 122, 144]

Scanning Electron Microscopy

All SEM images were taken with a Zeiss Auriga at 1 keV beam power.

Raman Spectroscopy

All Raman measurements were obtained using a LabRam spectrograph from JY-Horiba, with a 532 nm excitation wavelength.

4.3 Results and Discussion

4.3.1 Formation of PSI-Zn-H$_2$mim-TCNQ films

Following on the heels of our previous work embedding PSI in the metal organic framework of ZIF-8,[98] initially we had attempted to produce photocurrents from direct dropcast films of PSI@ZIF-8 that resulted unfortunately in negligible responses. The intrinsic insulation of the ZIF-8 material and diffusion-limiting nanopores render it an unsuitable material for long range charge transfer. But, our very failed attempts at generating of significant current led us to the concept of using the ZIF-8 as a sacrificial scaffold to create more conductive matrices in which the PSI could systematically remain embedded. As described in the experimental section, PSI@ZIF-8 was incubated with an excess of LiTCNQ, the only water-soluble TCNQ salt, and then acetic acid (HAc) to break down the ZIF-8 into Zn^{2+} and H_2mim^+ cations (schematically shown in Figure 4.1). The order of these steps is critical, as the TCNQ complexation happens almost instantaneously and the PSI will be excluded from the new matrix if HAc is added first to dissolve ZIF-8 without TCNQ being already present. For this same reason, any attempts at reacting aqueous solutions of Zn^{2+} and LiTCNQ or H_2mim^+ and LiTCNQ with PSI both resulted in precipitates that bound negligible amounts of PSI. Only when starting with PSI@ZIF-8 does over 90% of the PSI remain in the precipitate of the newly formed material because the breakdown of the first matrix is immediately followed by the formation of the new one. Because this material is expected to be a mixture of the two charge transfer salts $Zn^{2+}(TCNQ^-)_2(H_2O)_2$[145] and what we can reasonably reason from known chemistry to be $H_2mim^+TCNQ^-$,[146-148] the inclusion of both is at first assumed whereby this resultant blend is referred to from hereon as PSI-Zn-H_2mim-TCNQ. The subsequent dropcast films from the PSI-Zn-H_2mim-TCNQ complex salt are found to be ~ 2.5 microns in thickness, as measured by SEM cross sections in Figure 4.2.

4.3.2 Composition of PSI-Zn-H_2mim-TCNQ films

The Raman spectroscopy in Figure 4.3 (all peaks are scaled for comparison) indicates the complete transformation of our starting material. The absence of the unique peaks of ZIF-8 at 110, 175, and 680 cm^{-1} from the PSI-Zn-H_2mim-TCNQ spectrum indicate the absence of any unreacted ZIF-8. In contrast, the PSI peaks at 1160 and 1530 cm^{-1} both remain, which indicate that the protein chains of PSI have remained intact. Because of the similarities between the spectra for $Zn^{2+}(TCNQ^-)_2(H_2O)_2$ and $H_2mim^+TCNQ^-$, it is not possible from this data alone to conclude whether one or both complexes are present. However, the discernible peaks of 1200 and 1600 cm^{-1} from of these as seen from the PSI-Zn-H_2mim-TCNQ spectrum, confirm that we have successfully formed charge transfer complexes rather than breaking down the potentially fragile $TCNQ^-$ anion.[90, 147]

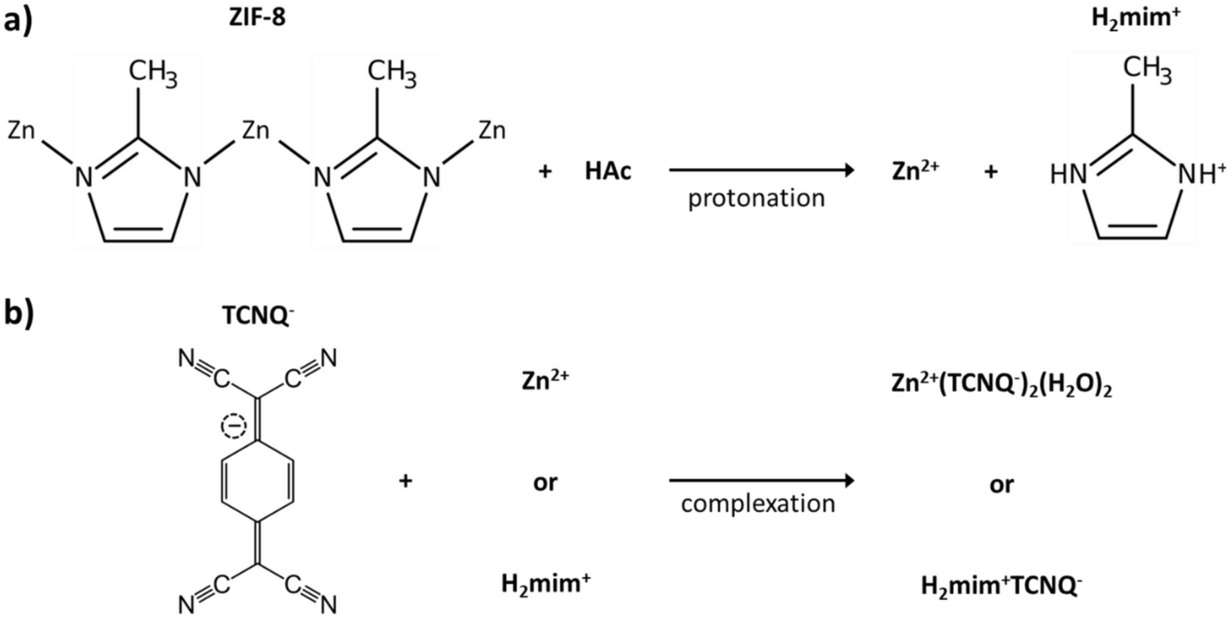

Figure 4.1 Schematic of (a) the breakdown of ZIF-8 by acetic acid to release Zn^{2+} and H_2mim^+ cations, and (b) the subsequent reaction of these cations with $TCNQ^-$ to form insoluble charge transfer complexes.

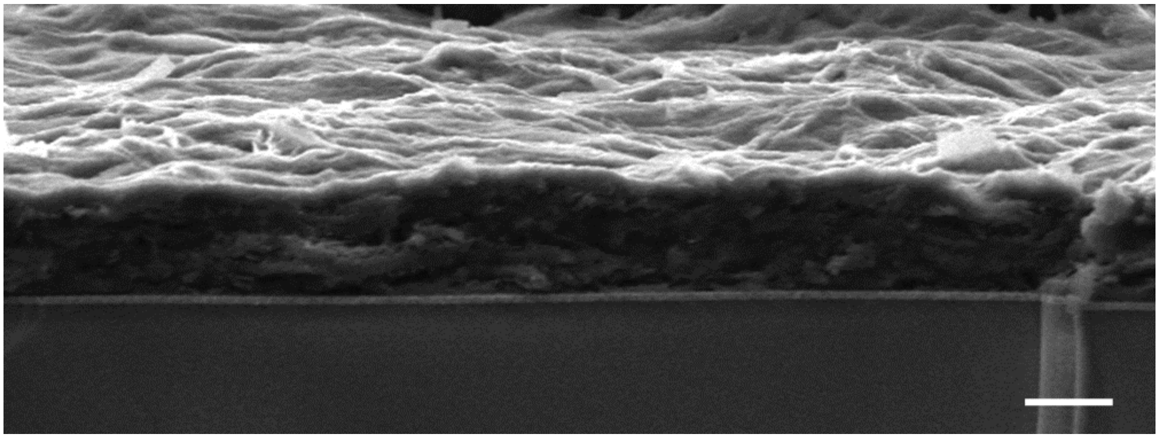

Figure 4.2 Cross section of a PSI-Zn-H_2mim-TCNQ film on ITO. Scale bar 2 microns.

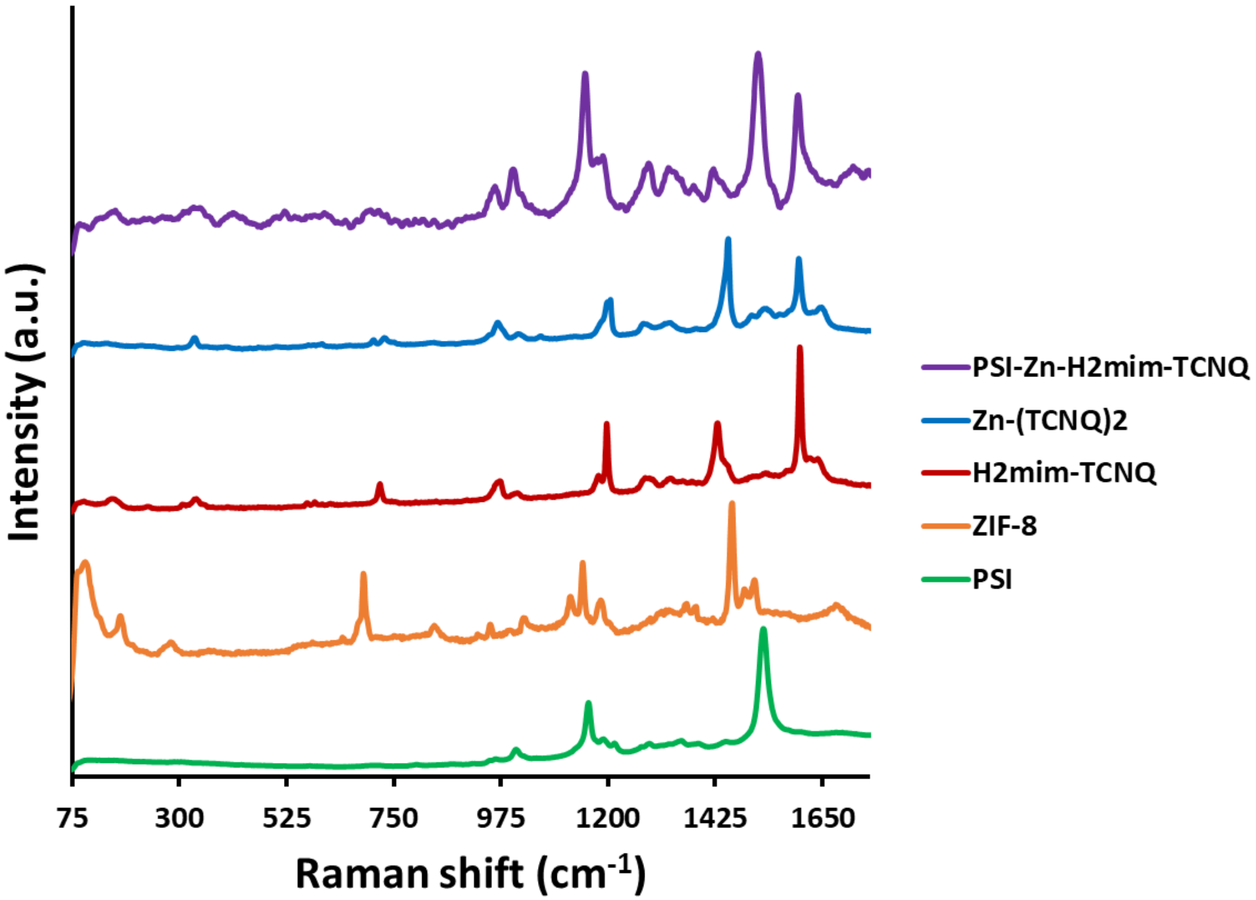

Figure 4.3 Raman spectroscopy prepared materials, indicating the breakdown of ZIF-8, the formation of charge transfer salts, and the inclusion of PSI into a single mixture.

While we would expect the ZIF-8 precursor to form stoichiometric amounts of $Zn^{2+}(TCNQ^{-})_2(H_2O)_2$ and $H_2mim^{+}TCNQ^{-}$, the presence of both can best be confirmed by LIBS analysis (Figure 4.4). The carbon (C I emission line at 247.86 nm) from 2-methylimidazole and TCNQ, the magnesium (Mg I emission line at 285.21 nm) chelated in the porphyrin rings of chlorophyll coordinated in PSI, and finally, the zinc (Zn I emission line at 334.50 nm), provides us with 3 strong atomic signature lines that can be systematically evaluated to draw robust qualitative analysis for the complexes formed. Specifically, we can look at the ratios of these background subtracted signals (C : Mg : Zn) in each sample.

Although all four samples contain C, only pure PSI and PSI-Zn-H_2mim-TCNQ can contain Mg. This is worth noting since the potential exposure of PSI to significant acetic acid during synthesis could have denatured it. The simplest path for that would be the acidic conditions dechelating the Mg ions from the chlorophyll, thereby denaturing the PSI and deactivating its absorption and charge transfer properties. However, the high Mg signal indicates that very little, if any chlorophyll was dechelated, and the ZIF-8 effectively neutralized all the present acid. Similarly, the presence of both significant Zn signals and highly elevated C signals demonstrate that both the charge transfer complexes ($Zn^{2+}(TCNQ^{-})_2(H_2O)_2$ and $H_2mim^{+}TCNQ^{-}$) contribute to the blended material. The ratios of the elemental signals in Table 4.1 affirm the presence of all 3 of the listed materials in the PSI-Zn-H_2mim-TCNQ complex.

4.3.3 Photocurrent measurements and electrochemical treatments

As previously mentioned, the PSI@ZIF-8 had yielded exceptionally low photocurrents. Even increasing the PSI contents from the previous 3.4% by weight to over 50% only resulted in photocurrent measurements of less than 0.1 $\mu A/cm^2$ (Figure 4.5, red line). But, after converting the PSI@ZIF-8 to PSI-Zn-H_2mim-TCNQ and dropcasting onto an ITO slide, we noticed that the photocurrent exhibits a 15-fold increase in magnitude up to 1.5 $\mu A/cm^2$ (blue line). When ZIF-8 is converted without any embedded PSI, the resulting charge transfer salts have similarly small photocurrent (black line), demonstrating that indeed the photoactivated electron transfer pathways through PSI are the sole drivers of the observed photocurrent.

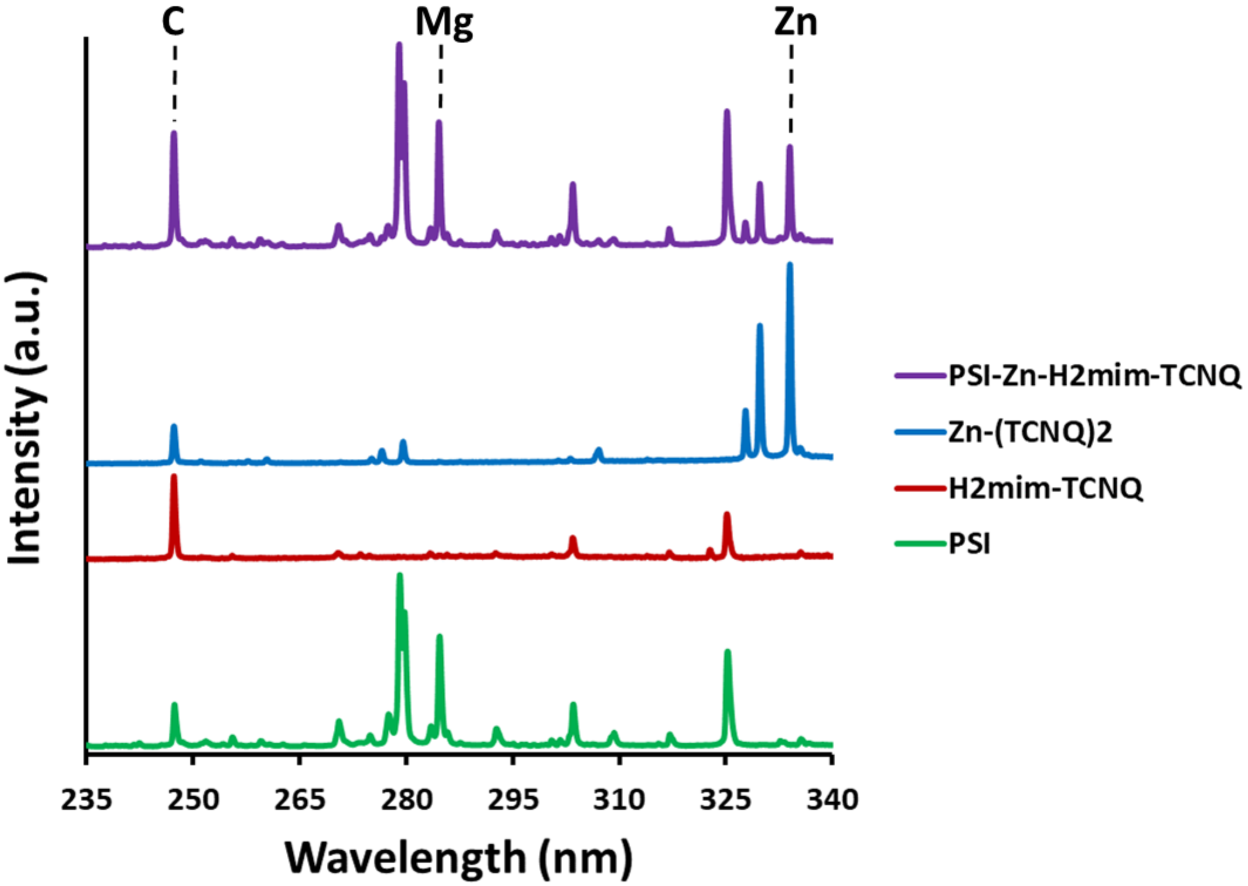

Figure 4.4 Elemental emissions from laser-induced breakdown spectroscopy. Presence of Mg and Zn signatures confirm both intact chlorophyll and blended TCNQ salts

Table 4.1 The ratio of elemental emission intensities of prepared samples, relative to their carbon emission lines

Sample material	**LIBS signal ratio (normalized to carbon)**		
	C	**Mg**	**Zn**
PSI	1	2.64	0
$H_2mim^+TCNQ^-$	1	0	0
$Zn^{2+}(TCNQ^-)_2(H_2O)_2$	1	0	5.42
PSI-Zn-H_2mim-TCNQ	1	1.1	0.87

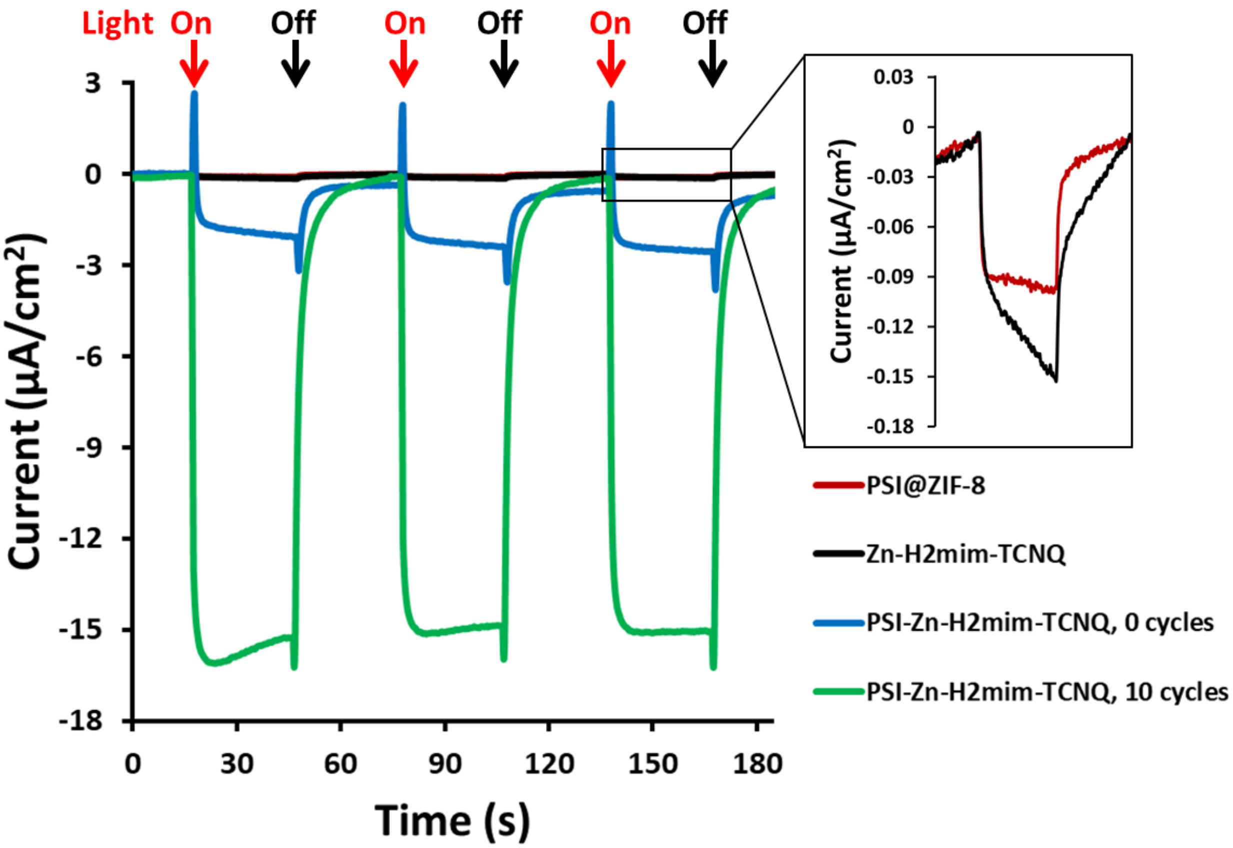

Figure 4.5 Photocurrent production of prepared samples, in the presence of 4 mM methyl viologen as electron scavenger and 100 mM ZnAc, illuminated by 300 W/m^2 red light in 30 second intervals. All measurements at OCV.

Remarkably, in a series of electrochemical experiments, we observed that if the PSI-Zn-H_2mim-TCNQ complex is briefly electrochemically cycled in a 100 mM ZnAc solution, the photocurrent increases by another order of magnitude all the way up to 15 μA/cm^2 (green line). Curiosity led us to perform continued cycling, although it did not provide any further increase in the photocurrent. In fact, repeated cycling eventually decreased the photocurrent magnitude. Motivated by these highly promising results, here we proceed to put forward our envisioned mechanisms for these unique observations. To this end, we resort to the cyclic voltammetry data shown in Figure 4.6 for the first 10 cycles of a PSI-Zn-H_2mim-TCNQ film sample immersed in 100 mM zinc acetate solution and scanned at 50 mV/s.

One needs to bear in mind that when PSI@ZIF-8 is formed, ZIF-8 nucleates on the surface exposed amino acid residues of PSI. The protocol used in this paper embeds 15 times more PSI than before, which leads to enhanced nucleation events and hence, discrete nano-sized ZIF-8 particles. These are then protonated and reacted with LiTCNQ to form $Zn^{2+}(TCNQ^-)_2(H_2O)_2$ and $H_2mim^+TCNQ^-$. Due to the immediacy of the complexation after breakdown, it is conceivable that these polymeric charge transfer salts also form discrete particles, rather than a homogenous continuous film. As indicated in Figure 5, scanning in the positive direction oxidizes $TCNQ^-$ to $TCNQ^0$, which then breaks down the charge complex and releases the cations. Subsequent scanning in the negative direction reduces $TCNQ^0$ to $TCNQ^-$ and the cations are bound again.[149] Herein, we posit that these cationic transfers promote electrochemical annealing of the PSI-Zn-H_2mim-TCNQ film that promote the formation of more homogeneous conductive pathways and establish better electrical connectivity between the PSI, the ITO surface and the soluble electron scavenger. This process is also substituting the H_2mim^+ cations for the Zn^{2+} cations in the PSI-Zn-H_2mim-TCNQ film during each scan since any expelled cations diffuse into the bulk solution, while the 100 mM ZnAc out-populates and thus out-competes the return of the H_2mim^+ ions.

Figure 4.7 shows the stark difference in both color and texture of the two charge transfer salts, (a) $H_2mim^+TCNQ^-$ which dries into an airy material that easily dislodges and (b) $Zn^{2+}(TCNQ^-)_2(H_2O)_2$ which dries as a dense-packed film. The bright color change from (c) to (d) reveals the growth of $Zn^{2+}(TCNQ^-)_2(H_2O)_2$ during electrochemical cycling. The same 4 samples are pictured in Figure 4.8, where SEM images reveal the underlying morphology.

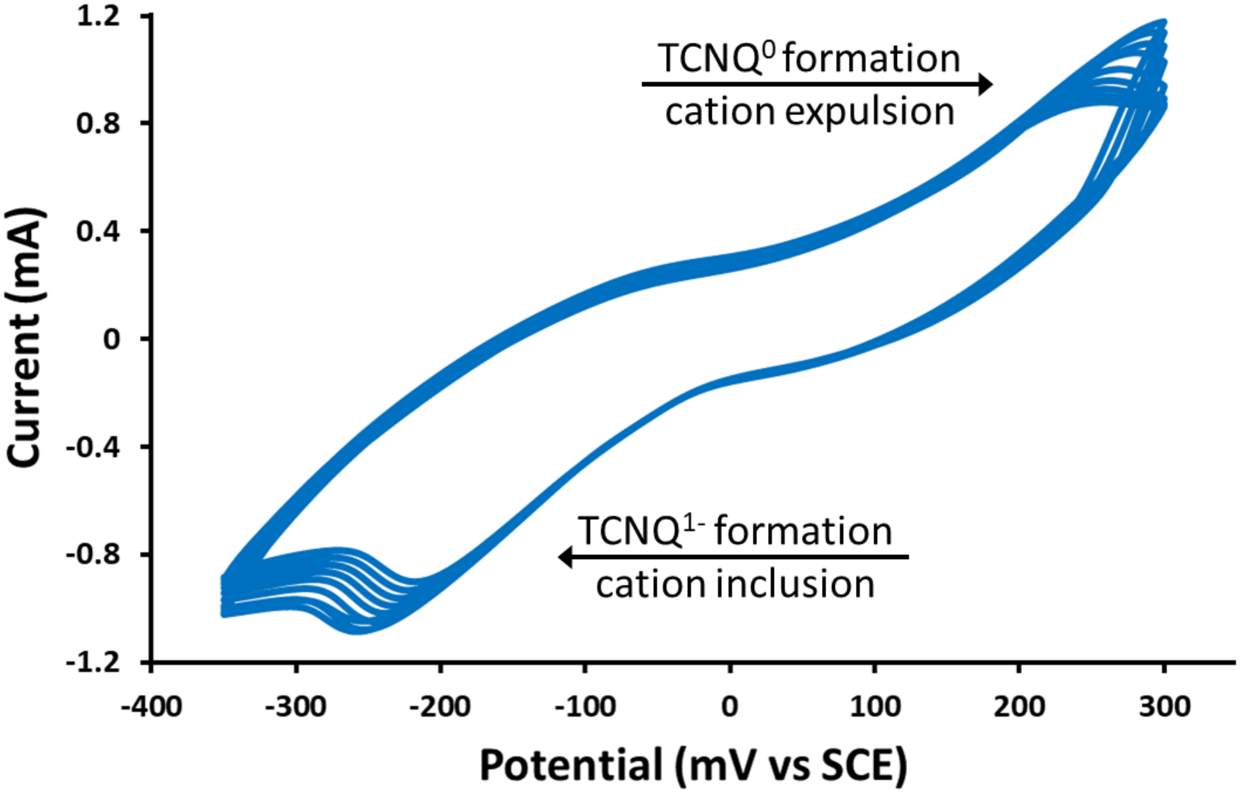

Figure 4.6 Cyclic voltammetry of a PSI-Zn-H_2mim-TCNQ film in 100 mM zinc acetate, scanned at 50 mV/s.

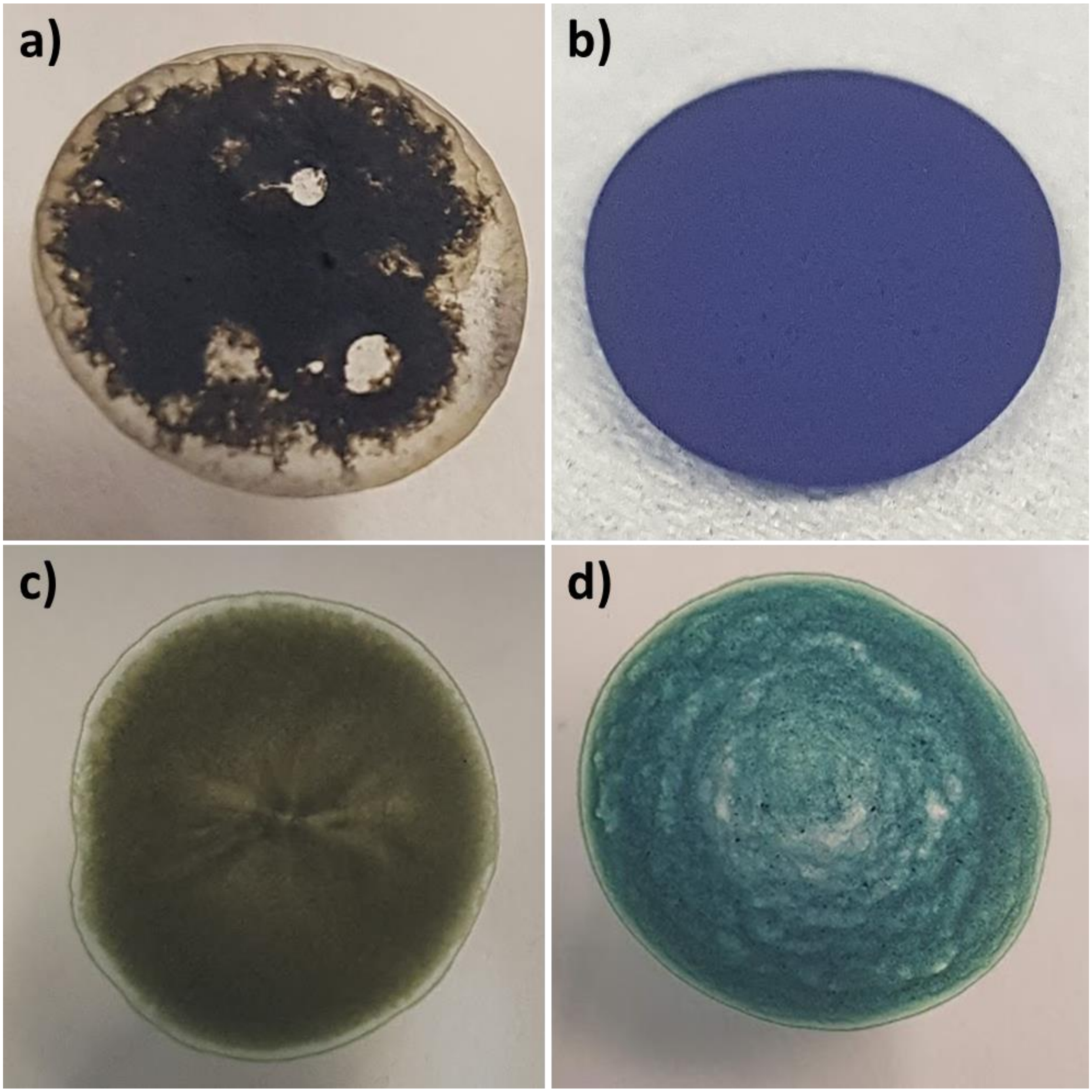

Figure 4.7 Photographs of dropcast films on ITO of (a) $H_2mim^+TCNQ^-$, (b) $Zn^{2+}(TCNQ^-)_2(H_2O)_2$, and PSI-Zn-$H_2$mim-TCNQ both (c) before and (d) after electrochemically cycling in 100 mM ZnAc.

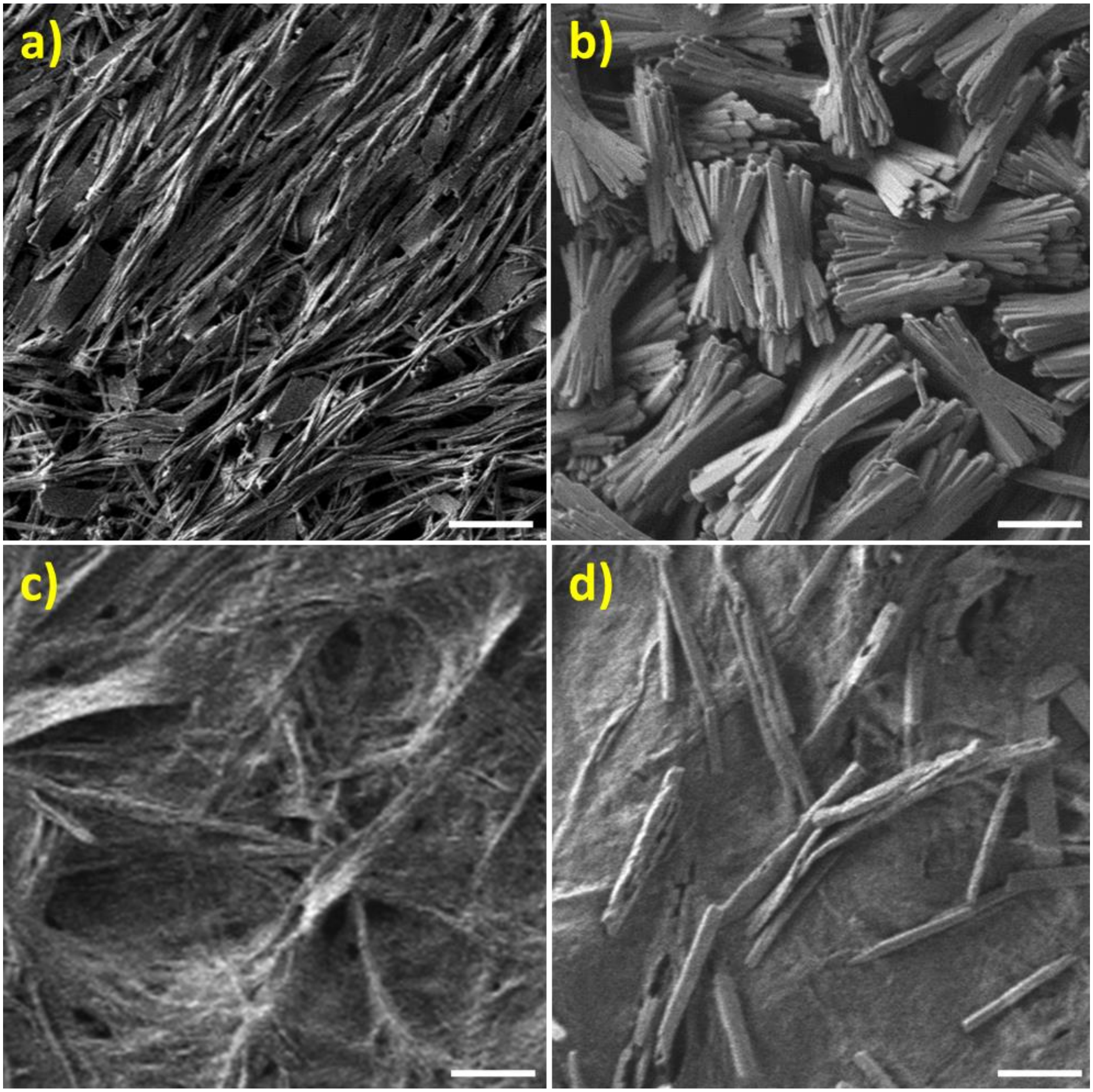

Figure 4.8 SEM images of dropcast films on ITO of (a) $H_2mim^+TCNQ^-$, (b) $Zn^{2+}(TCNQ^-)_2(H_2O)_2$, and PSI-Zn-$H_2$mim-TCNQ both (c) before and (d) after electrochemically cycling in 100 mM ZnAc. Scale bar 2 microns.

The reasons for such drastic differences in texture are revealed by SEM images, showing that the imidazole-based complex builds long flexible chains (Figure 4.8a), while the zinc-based complex builds shorter, thicker stacks with perhaps some level of crystallinity, as seen from Figure 4.8b. On the contrary, the highly polymeric nature of PSI-Zn-H_2mim-TCNQ is revealed in Figure 4.8c, but with a loss of clarity seen in the image due to the large presence of PSI trimers embedded throughout. As this sample is cycled in a zinc solution, the surface begins to grow blocky structures (Figure 4.8d) which are most likely due to the $Zn^{2+}(TCNQ^-)_2(H_2O)_2$ formations. Furthermore, continued cycling reveals the enhanced growth of such larger structures. This might very well shed light on why the successive cycles eventually lower the photocurrent productions. Although $Zn^{2+}(TCNQ^-)_2(H_2O)_2$ may be more conductive than $H_2mim^+TCNQ^-$, it is beyond the scope of the study to probe how these morphological changes (independent from chemical composition) affect the conductivity.[150-152] Beyond that, the photocurrent output is not merely a function of the conductivity, but also of the extent of interface between the matrix and PSI. As larger structures dominate the film, the surface area available for such contact decreases. It is also possible that during the cation expulsion step, PSI is irreversibly lost from the film, or that TCNQ is then reacting with dissolved oxygen in the solution. Further investigations are definitely required to answer such detailed mechanistic questions. While such cycling beyond certain parameters may inhibit photocurrent in this particular architecture, we have demonstrated, for the first time, the solid-solid conversion of one TCNQ salt to another via cation-exchange in an aqueous environment. In turn, this opens the doors to explore many other TCNQ-based charge transfer salts, as well as provides a superior method to interface biological materials to conductive interfacial matrices without using any organic solvents during the fabrication.

4.4 Conclusions

In this work, we have demonstrated a heretofore not reported methodology for the conversion of a metal-organic framework (ZIF-8) to a TCNQ-based charge transfer salt in an entirely aqueous environment, while simultaneously retaining the full functionality of the embedded supramolecular photosynthetic protein complex PSI without denaturing it. The subsequent PSI-Zn-H_2mim-TCNQ charge transfer salt complex formed was shown to contain both the $Zn^{2+}(TCNQ^-)_2(H_2O)$ and $H_2mim^+TCNQ^-$ complexes, thereby benefiting from both the constituents to form dense and stable films with high surface area and electrical connectivity. We have also shown that through systematic electrochemical cycling, the Zn^{2+} and H_2mim^+ cations from the ZIF-8 framework can be reversibly exchanged to alter the composition of the solid TCNQ-based film. Furthermore, through limited (~10) cycling, the film was electrochemically annealed to increase both electrical connectivity and electron conductivity that enabled the embedded PSI in the as-fabricated charge transfer salt film to generate significant photocurrents (~15 $\mu A/cm^2$). The photocurrent generations reported here indicate a ~150 and ~750 fold increase respectively from our previous works reporting photocurrent enhancements due to plasmonic interactions with PSI, and due to PSI confinements in lipid bilayer membranes.[38, 141] Such work paves the path for future investigations into the ways to control the morphology and chemistry of TCNQ-based charge transfer salt complexes during the aforementioned PSI reconstitution process that can, in turn, allow the design of PSI thin films with greater conductivity and/or, charge transfer interfaces for catalytic reactions.

CHAPTER 5

CONCLUSIONS AND FUTURE DIRECTION

This dissertation focuses on implementing PSI from *Thermosynechococcus Elongatus* into bio-hybrid devices and investigating the fundamental interactions of the redox transfer mechanism, the stabilizing and optical effects of unique confinements, and the augmented photocurrent generation of PSI embedded in a conductive polymer formed in situ through substitutionary reactions.

In **Chapter 1**, we discussed the nature of the photosynthetic process and introduced a fundamental understanding of the biological electron pump Photosystem I. Further insight was given into the unique and robust photoelectrochemical properties of PSI which have made it such highly studied structure. A brief history of PSI biohybrid devices was laid out, emphasizing the need to understand the specific redox transfer steps, to stabilize and coordinate long range structures of PSI, and to properly interface PSI with suitably conductive pathways.

In **Chapter 2**, chronoamperometry measurements under light and dark conditions reveal the mechanistic picture behind the electrochemical pathway mediated by methyl viologen (MV) for the electron transport from the stromal F_A/F_B terminal of PSI (the ones that are directionally oriented) to the counter electrode in solution. Specifically, our experiments reveal the critical role of solution-phase dissolved O_2 concentrations in producing an intermediate complex (MVO*), heretofore not accounted for, that facilitates the electron scavenging mechanism in the presence of MV. Thus, the rate limiting step in the kinetics of photocurrent generation from PSI/SAM/Au systems is directly related to the rate of formation of this complex, as evidenced by the non-linear increase in photocurrent density with increasing dissolved O_2 concentrations.

The proposed model for the electron transfer pathway from our current findings put in review the redox species of electron scavenging by the most successful and widely used acceptor, MV, thereby adjusting its known -450 mV peak to the true PSI-interactive species at -325 mV vs NHE. As the puzzle remains unsolved for which properties yield the most ideal electron mediator, these observations contribute additional insight into the optimization of the energetics of electron transport pathways from PSI to a soluble carrier, solid-state electrode, or bound catalysts in future photoactivated bio-hybrid energy harvesting constructs.

In **Chapter 3**, we demonstrated the first-ever successful encapsulation of the supramolecular photosynthetic protein, PSI, in a metal organic framework, ZIF-8. We find that the large, membrane-native PSI initiates nucleation of ZIF-8 on its surface, while subsequent coatings of ZIF-8 reactants fill in the ZIF mesopores to complete the coverage of the protective framework.

Our results indicate that the as-fabricated PSI@ZIF-8 composites exhibit significant blue shift and intensity enhancements in their fluorescence emissions, when compared to that for native PSI, owing to their confinements inside the hybrid crystalline frameworks of ZIF-8. We have also successfully shown that this encapsulation preserves the PSI structure while protecting it from harsh denaturing conditions. To this end, we have demonstrated through systematic visual inspections as well as detailed pump-probe experiments that harsh detergents such as SDS are prevented from accessing the embedded PSI through the small ZIF-8 pores, while organic solvents such as ethanol is able to access the framework interiors but, unable to disrupt the chlorophyll network due to steric hindrance.

Finally, our solution-phase pump-probe experiments have established that the unique light-activated charge separation facilitated by PSI's chlorophyll networks and electron transport pathways remain unaffected in the PSI@ZIF-8 composites, thereby indicating that the mediators such as MV and DCPIP are able to diffuse through the framework to scavenge and donate electrons from and to PSI. Upon completion of this work, further investigations underway in our group to quantify the macro-scale diffusion kinetics of these mediators and understand the complex charge transport processes within these hybrid frameworks. In summary, our first successful encapsulation of transmembrane photoactive proteins within MOF scaffolds laid the fundamental groundworks for robust design of organic-inorganic interfaces in bio-hybrid photoactive materials that can be functional under otherwise incompatible conditions for future photochemical solar fuel conversions.

In **Chapter 4**, continuing the efforts to enhance the photocurrent generation from our PSI@ZIF-8 constructs fabricated in Chapter 3, this thesis demonstrates the conversion of the previously synthesized PSI@ZIF-8 to a TCNQ-based charge transfer salt, while simultaneously retaining the full capture and functionality of the embedded PSI protein complex. The subsequent PSI-Zn-H_2mim-TCNQ charge transfer salt complex formed was shown to contain both the $Zn^{2+}(TCNQ^{-})_2(H_2O)$ and $H_2mim^{+}TCNQ^{-}$ complexes, thereby benefiting from both the constituents to form dense and stable films with high surface area and electrical connectivity. We have also shown that through systematic electrochemical cycling, the Zn^{2+} and H_2mim^{+} cations from the ZIF-8 framework can be reversibly exchanged to alter the composition of the solid TCNQ-based film. This electrochemical annealing significantly enhanced photocurrents (from 1.5 to 15 $\mu A/cm^2$). Such work paves the path for future investigations into the ways to control the morphology and chemistry of TCNQ-based charge transfer salt complexes during the aforementioned PSI reconstitution process that can, in turn, allow the design of PSI thin films with greater conductivity and/or, charge transfer interfaces for catalytic reactions.

LIST OF REFERENCES

1. Orr, L.; Govindjee, Photosynthesis online. *Photosynthesis Research* **2010,** *105* (2), 167-200.
2. Leadbetter, E. R.; Poindexter, J. S., *Bacteria in Nature*. Plenum Press: New York,, 1985; Vol. 1.
3. Walker, D., *Energy, Plants and Man*. Oxygraphics: Brighton, 1992.
4. Liberton, M.; Page, L. E.; O'Dell, W. B.; O'Neill, H.; Mamontov, E.; Urban, V. S.; Pakrasi, H. B., Organization and Flexibility of Cyanobacterial Thylakoid Membranes Examined by Neutron Scattering. *The Journal of Biological Chemistry* **2013,** *288* (5), 3632-3640.
5. Stingaciu, L.-R.; O'Neill, H.; Liberton, M.; Urban, V. S.; Pakrasi, H. B.; Ohl, M., Revealing the Dynamics of Thylakoid Membranes in Living Cyanobacterial Cells. *Scientific Reports* **2016,** *6*, 19627.
6. Jordan, P.; Fromme, P.; Witt, H. T.; Klukas, O.; Saenger, W.; Krauß, N., Three-dimensional structure of cyanobacterial photosystem I at 2.5 Å resolution. *Nature* **2001,** *411* (6840), 909.
7. Nelson, N.; Yocum, C. F., Structure and function of photosystems I and II. *Annual Review of Plant Biology* **2006,** *57*, 521-565.
8. Golbeck, J. H., *Photosystem I: The light-driven plastocyanin: ferredoxin oxidoreductase*. Springer: Netherlands, 2006; Vol. 24.
9. Brettel, K., Electron transfer and arrangement of the redox cofactors in photosystem I. *Biochimica et Biophysica Acta (BBA) - Bioenergetics* **1997,** *1318* (3), 322-373.
10. Brettel, K.; Leibl, W., Electron transfer in photosystem I. *Biochimica et Biophysica Acta (BBA) - Bioenergetics* **2001,** *1507* (1–3), 100-114.
11. Nelson, N., Evolution of photosystem I and the control of global enthalpy in an oxidizing world. *Photosynthesis Research* **2013,** *116* (2-3), 145-151.
12. Vassiliev, I. R.; Jung, Y.-S.; Smart, L. B.; Schulz, R.; McIntosh, L.; Golbeck, J. H., A mixed-ligand iron-sulfur cluster (C556SPaB or C565SPsaB) in the Fx-binding site leads to a decreased quantum efficiency of electron transfer in photosystem I. *Biophys. J.* **1995,** *69* (4), 1544-1553.
13. Blankenship, R. E.; Tiede, D. M.; Barber, J.; Brudvig, G. W.; Fleming, G.; Ghirardi, M.; Gunner, M. R.; Junge, W.; Kramer, D. M.; Melis, A.; Moore, T. A.; Moser, C. C.; Nocera, D. G.; Nozik, A. J.; Ort, D. R.; Parson, W. W.; Prince, R. C.; Sayre, R. T., Comparing Photosynthetic and Photovoltaic Efficiencies and Recognizing the Potential for Improvement. *Science* **2011,** *332* (6031), 805-809.
14. LaVan, D. A.; Cha, J. N., Approaches for biological and biomimetic energy conversion. *Proceedings of the National Academy of Sciences of the United States of America* **2006,** *103* (14), 5251-5255.
15. Carmeli, I.; Mangold, M.; Frolov, L.; Zebli, B.; Carmeli, C.; Richter, S.; Holleitner, A. W., A photosynthetic reaction center covalently bound to carbon nanotubes. *Adv. Mater.* **2007,** *19* (22), 3901-+.
16. Das, R.; Kiley, P. J.; Segal, M.; Norville, J.; Yu, A. A.; Wang, L. Y.; Trammell, S. A.; Reddick, L. E.; Kumar, R.; Stellacci, F.; Lebedev, N.; Schnur, J.; Bruce, B. D.; Zhang, S. G.; Baldo, M., Integration of photosynthetic protein molecular complexes in solid-state electronic devices. *Nano Lett.* **2004,** *4* (6), 1079-1083.
17. Frolov, L.; Wilner, O.; Carmeli, C.; Carmeli, I., Fabrication of Oriented Multilayers of Photosystem I Proteins on Solid Surfaces by Auto-Metallization. *Adv. Mater.* **2008,** *20* (2), 263-266.

18. Terasaki, N.; Yamamoto, N.; Hiraga, T.; Sato, I.; Inoue, Y.; Yamada, S., Fabrication of novel photosystem I-gold nanoparticle hybrids and their photocurrent enhancement. *Thin Solid Films* **2006,** *499* (1-2), 153-156.
19. Gerster, D.; Reichert, J.; Bi, H.; Barth, J. V.; Kaniber, S. M.; Holleitner, A. W.; Visoly-Fisher, I.; Sergani, S.; Carmeli, I., Photocurrent of a single photosynthetic protein. *Nat Nano* **2012,** *7* (10), 673-676.
20. Ciesielski, P. N.; Scott, A. M.; Faulkner, C. J.; Berron, B. J.; Cliffel, D. E.; Jennings, G. K., Functionalized Nanoporous Gold Leaf Electrode Films for the Immobilization of Photosystem I. *Acs Nano* **2008,** *2* (12), 2465-2472.
21. LeBlanc, G.; Chen, G.; Gizzie, E. A.; Jennings, G. K.; Cliffel, D. E., Enhanced Photocurrents of Photosystem I Films on p-Doped Silicon. *Adv Mater* **2012,** *24* (44), 5959-5962.
22. LeBlanc, G.; Chen, G.; Jennings, G. K.; Cliffel, D. E., Photoreduction of Catalytic Platinum Particles Using Immobilized Multilayers of Photosystem I. *Langmuir* **2012,** *28* (21), 7952-7956.
23. Gunther, D.; LeBlanc, G.; Prasai, D.; Zhang, J. R.; Cliffel, D. E.; Bolotin, K. I.; Jennings, G. K., Photosystem I on Graphene as a Highly Transparent, Photoactive Electrode. *Langmuir* **2013,** *29* (13), 4177-4180.
24. LeBlanc, G.; Winter, K. M.; Crosby, W. B.; Jennings, G. K.; Cliffel, D. E., Integration of Photosystem I with Graphene Oxide for Photocurrent Enhancement. *Adv. Energy Mater.* **2014,** *4* (9), 5.
25. Frolov, L.; Rosenwaks, Y.; Richter, S.; Carmeli, C.; Carmeli, I., Photoelectric Junctions Between GaAs and Photosynthetic Reaction Center Protein. *The Journal of Physical Chemistry C* **2008,** *112* (35), 13426-13430.
26. Carmeli, I.; Mangold, M.; Frolov, L.; Zebli, B.; Carmeli, C.; Richter, S.; Holleitner, A. W., A Photosynthetic Reaction Center Covalently Bound to Carbon Nanotubes. *Adv Mater* **2007,** *19* (22), 3901-3905.
27. Kaniber, S. M.; Brandstetter, M.; Simmel, F. C.; Carmeli, I.; Holleitner, A. W., On-Chip Functionalization of Carbon Nanotubes with Photosystem I. *J Am Chem Soc* **2010,** *132* (9), 2872-2873.
28. Mukherjee, D.; Vaughn, M.; Khomami, B.; Bruce, B. D., Modulation of cyanobacterial Photosystem I deposition properties on alkanethiolate Au substrate by various experimental conditions. *Colloids and Surfaces B: Biointerfaces* **2011,** *88*, 181 - 190.
29. Bennett, T.; Niroomand, H.; Pamu, R.; Ivanov, I.; Mukherjee, D.; Khomami, B., Elucidating the role of methyl viologen as a scavenger of photoactivated electrons from photosystem I under aerobic and anaerobic conditions. *PCCP* **2016,** *18* (12), 8512-8521.
30. Terasaki; Noritaka Yamamoto Dr.; Takashi Hiraga Dr.; Yoshinori Yamanoi Dr.; Tetsu Yonezawa Dr.; Hiroshi Nishihara Prof.; Tsutomu Ohmori Dr.; Makoto Sakai Dr.; Masaaki Fujii Prof.; Akihiko Tohri Dr.; Masako Iwai Dr.; Yasunori Inoue Prof.; Satoshi Yoneyama Dr.; Makoto Minakata Prof.; Prof., I. E., Plugging a Molecular Wire into Photosystem I: Reconstitution of the Photoelectric Conversion System on a Gold Electrode. *Angew. Chem.* **2009,** *48* (9), 1585-1587.
31. Carmeli, I.; Frolov, L.; Carmeli, C.; Richter, S., Photovoltaic activity of photosystem I-based self-assembled monolayer. *J. Am. Chem. Soc.* **2007,** *129*, 12352-12353.
32. Manocchi, A. K.; Baker, D. R.; Pendley, S. S.; Nguyen, K.; Hurley, M. M.; Bruce, B. D.; Sumner, J. J.; Lundgren, C. A., Photocurrent generation from surface assembled photosystem I on alkanethiol modified electrodes. *Langmuir* **2013,** *29* (7), 2412-9.

33. Kaniber, S. M.; Brandstetter, M.; Simmel, F. C.; Carmeli, I.; Holleitner, A. W., On-Chip Functionalization of Carbon Nanotubes with Photosystem I. *J. Am. Chem. Soc.* **2010,** *132* (9), 2872-+.
34. Kaniber, S. M.; Simmel, F. C.; Holleitner, A. W.; Carmeli, I., The optoelectronic properties of a photosystem I–carbon nanotube hybrid system. *Nanotechnology* **2009,** *20* (34), 345701.
35. Mershin, A.; Matsumoto, K.; Kaiser, L.; Yu, D.; Vaughn, M.; Nazeeruddin, M. K.; Bruce, B. D.; Graetzel, M.; Zhang, S., Self-assembled photosystem-I biophotovoltaics on nanostructured TiO 2 and ZnO. *Scientific Reports* **2012,** *2*, 234.
36. Brecht, M.; Hussels, M.; Nieder, J. B.; Fang, H.; Elsässer, C., Plasmonic interactions of photosystem I with Fischer patterns made of Gold and Silver. *Chem. Phys.* **2012,** *406*, 15-20.
37. Czechowski, N.; Lokstein, H.; Kowalska, D.; Ashraf, K.; Cogdell, R.; Mackowski, S., Large plasmonic fluorescence enhancement of cyanobacterial photosystem I coupled to silver island films. *Appl. Phys. Lett.* **2014,** *105* (4), 043701.
38. Pamu, R.; Sandireddy, V. P.; Kalyanaraman, R.; Khomami, B.; Mukherjee, D., Plasmon-Enhanced Photocurrent from Photosystem I Assembled on Ag Nanopyramids. *The Journal of Physical Chemistry Letters* **2018,** *9* (5), 970-977.
39. Frolov, L.; Rosenwaks, Y.; Carmeli, C.; Carmeli, I., Fabrication of a Photoelectronic Device by Direct Chemical Binding of the Photosynthetic Reaction Center Protein to Metal Surfaces. *Adv. Mater.* **2005,** *17* (20), 2434-2437.
40. Kondo, M.; Nakamura, Y.; Fujii, K.; Nagata, M.; Suemori, Y.; Dewa, T.; Lida, K.; Gardiner, A. T.; Cogdell, R. J.; Nango, M., Self-assembled monolayer of light-harvesting core complexes from photosynthetic bacteria on a gold electrode modified with alkanethiols. *Biomacromolecules* **2007,** *8* (8), 2457-2463.
41. Mukherjee, D.; May, M.; Vaughn, M.; Bruce, B. D.; Khomami, B., Controlling the Morphology of Photosystem I Assembly on Thiol-Activated Au Substrates. *Langmuir* **2010,** *26* (20), 16048-16054.
42. Ciobanu, M.; Kincaid, H. A.; Lo, V.; Dukes, A. D.; Jennings, G. K.; Cliffel, D. E., Electrochemistry and photoelectrochemistry of photosystem I adsorbed on hydroxyl-terminated monolayers. *J. Electroanal. Chem.* **2007,** *599* (1), 72-78.
43. Kincaid, H. A.; Niedringhaus, T.; Ciobanu, M.; Cliffel, D. E.; Jennings, G. K., Entrapment of photosystem I within self-assembled films. *Langmuir* **2006,** *22* (19), 8114-8120.
44. Ko, B. S.; Babcock, B.; Jennings, G. K.; Tilden, S. G.; Peterson, R. R.; Cliffel, D.; Greenbaum, E., Effect of surface composition on the adsorption of photosystem I onto alkanethiolate self-assembled monolayers on gold. *Langmuir* **2004,** *20* (10), 4033-4038.
45. Mukherjee, D.; May, M.; Khomami, B., Detergent-protein interactions in aqueous buffer suspensions of Photosystem I (PS I). *J. Colloid Interface Sci.* **2011,** *358* (2), 477-484.
46. Manocchi, A. K.; Baker, D. R.; Pendley, S. S.; Nguyen, K.; Hurley, M. M.; Bruce, B. D.; Sumner, J. J.; Lundgren, C. A., Photocurrent Generation from Surface Assembled Photosystem I on Alkanethiol Modified Electrodes. *Langmuir* **2013,** *29* (7), 2412-2419.
47. Chen, G.; LeBlanc, G.; Jennings, G. K.; Cliffel, D. E., Effect of Redox Mediator on the Photo-Induced Current of a Photosystem I Modified Electrode. *J. Electrochem. Soc.* **2013,** *160* (6), H315-H320.
48. Yamanoi, Y.; Terasaki, N.; Miyachi, M.; Inoue, Y.; Nishihara, H., Enhanced photocurrent production by photosystem I with modified viologen derivatives. *Thin Solid Films* **2012,** *520* (16), 5123-5127.

49. Suntres, Z. E., Role of antioxidants in paraquat toxicity. *Toxicology* **2002,** *180* (1), 65-77.
50. Badura, A.; Guschin, D.; Kothe, T.; Kopczak, M. J.; Schuhmann, W.; Roegner, M., Photocurrent generation by photosystem 1 integrated in crosslinked redox hydrogels. *Energy & Environmental Science* **2011,** *4* (7), 2435-2440.
51. Nguyen, K.; Vaughn, M.; Frymier, P.; Bruce, B. D., In vitro kinetics of P 700+ reduction of Thermosynechococcus elongatus trimeric Photosystem I complexes by recombinant cytochrome c 6 using a Joliot-type LED spectrophotometer. *Photosynth. Res.* **2017,** *131* (1), 79-91.
52. Zhao, F.; Ruff, A.; Rögner, M.; Schuhmann, W.; Conzuelo, F., Extended Operational Lifetime of a Photosystem-Based Bioelectrode. *J. Am. Chem. Soc.* **2019**.
53. Gordiichuk, P. I.; Wetzelaer, G. J. A.; Rimmerman, D.; Gruszka, A.; de Vries, J. W.; Saller, M.; Gautier, D. A.; Catarci, S.; Pesce, D.; Richter, S., Solid-State Biophotovoltaic Cells Containing Photosystem I. *Adv. Mater.* **2014,** *26* (28), 4863-4869.
54. Ciesielski, P. N.; Hijazi, F. M.; Scott, A. M.; Faulkner, C. J.; Beard, L.; Emmett, K.; Rosenthal, S. J.; Cliffel, D.; Jennings, G. K., Photosystem I - Based biohybrid photoelectrochemical cells. *Bioresour. Technol.* **2010,** *101* (9), 3047-3053.
55. LeBlanc, G.; Chen, G.; Gizzie, E. A.; Jennings, G. K.; Cliffel, D. E., Enhanced photocurrents of photosystem I films on p-doped silicon. *Adv. Mater.* **2012,** *24* (44), 5959-62.
56. Darby, E.; LeBlanc, G.; Gizzie, E. A.; Winter, K. M.; Jennings, G. K.; Cliffel, D. E., Photoactive Films of Photosystem I on Transparent Reduced Graphene Oxide Electrodes. *Langmuir* **2014,** *30* (29), 8990-8994.
57. Feifel, S.; Stieger, K.; Lokstein, H.; Lux, H.; Lisdat, F., High photocurrent generation by photosystem I on artificial interfaces composed of π-system-modified graphene. *Journal of Materials Chemistry A* **2015,** *3* (23), 12188-12196.
58. Baker, D. R.; Manocchi, A. K.; Lamicq, M. L.; Li, M.; Nguyen, K.; Sumner, J. J.; Bruce, B. D.; Lundgren, C. A., Comparative photoactivity and stability of isolated cyanobacterial monomeric and trimeric Photosystem I. *The Journal of Physical Chemistry B* **2014,** *118* (10), 2703-2711.
59. Robinson, M.; Simons, C.; Cliffel, D.; Jennings, G., Photocatalytic photosystem I/PEDOT composite films prepared by vapor-phase polymerization. *Nanoscale* **2017,** *9* (18), 6158-6166.
60. Gizzie, E. A.; LeBlanc, G.; Jennings, G. K.; Cliffel, D. E., Electrochemical Preparation of Photosystem I–Polyaniline Composite Films for Biohybrid Solar Energy Conversion. *ACS Applied Materials & Interfaces* **2015**.
61. Stieger, K. R.; Ciornii, D.; Kölsch, A.; Hejazi, M.; Lokstein, H.; Feifel, S. C.; Zouni, A.; Lisdat, F., Engineering of supramolecular photoactive protein architectures: the defined co-assembly of photosystem I and cytochrome c using a nanoscaled DNA-matrix. *Nanoscale* **2016,** *8* (20), 10695-10705.
62. Scholes, G. D., Quantum-coherent electronic energy transfer: Did nature think of it first? *The Journal of Physical Chemistry Letters* **2010,** *1* (1), 2-8.
63. Matsumoto, K.; Zhang, S.; Koutsopoulos, S., Enhanced electron transfer activity of photosystem I by polycations in aqueous solution. *Biomacromolecules* **2010,** *11* (11), 3152-3157.
64. Niroomand, H.; Pamu, R.; Mukherjee, D.; Khomami, B., Microenvironment alterations enhance photocurrents from photosystem I confined in supported lipid bilayers. *Journal of Materials Chemistry A* **2018**.

65. Niroomand, H.; Pamu, R.; Mukherjee, D.; Khomami, B., Tuning the photocurrent generations from photosystem I assembled in tailored biotic–abiotic interfaces. *MRS Communications* **2018**, 1-7.
66. Gizzie, E. A.; Niezgoda, J. S.; Robinson, M. T.; Harris, A. G.; Jennings, G. K.; Rosenthal, S. J.; Cliffel, D. E., Photosystem I-polyaniline/TiO 2 solid-state solar cells: simple devices for biohybrid solar energy conversion. *Energy & Environmental Science* **2015,** *8* (12), 3572-3576.
67. Stavila, V.; Talin, A. A.; Allendorf, M., MOF-based electronic and opto-electronic devices. *Chem. Soc. Rev.* **2014,** *43* (16), 5994-6010.
68. Farha, O. K.; Eryazici, I.; Jeong, N. C.; Hauser, B. G.; Wilmer, C. E.; Sarjeant, A. A.; Snurr, R. Q.; Nguyen, S. T.; Yazaydın, A. O. z. r.; Hupp, J. T., Metal–organic framework materials with ultrahigh surface areas: is the sky the limit? *J. Am. Chem. Soc.* **2012,** *134* (36), 15016-15021.
69. Furukawa, H.; Ko, N.; Go, Y. B.; Aratani, N.; Choi, S. B.; Choi, E.; Yazaydin, A. Ö.; Snurr, R. Q.; O'Keeffe, M.; Kim, J., Ultrahigh porosity in metal-organic frameworks. *Science* **2010,** *329* (5990), 424-428.
70. Furukawa, H.; Cordova, K. E.; O'Keeffe, M.; Yaghi, O. M., The chemistry and applications of metal-organic frameworks. *Science* **2013,** *341* (6149), 1230444.
71. Furukawa, H.; Yaghi, O. M., Storage of hydrogen, methane, and carbon dioxide in highly porous covalent organic frameworks for clean energy applications. *J. Am. Chem. Soc.* **2009,** *131* (25), 8875-8883.
72. Farrusseng, D., *Metal-organic frameworks: applications from catalysis to gas storage*. John Wiley & Sons: 2011.
73. Li, S.-L.; Xu, Q., Metal–organic frameworks as platforms for clean energy. *Energy & Environmental Science* **2013,** *6* (6), 1656.
74. Farrusseng, D.; Aguado, S.; Pinel, C., Metal–organic frameworks: opportunities for catalysis. *Angew. Chem. Int. Ed.* **2009,** *48* (41), 7502-7513.
75. Heine, J.; Müller-Buschbaum, K., Engineering metal-based luminescence in coordination polymers and metal–organic frameworks. *Chem. Soc. Rev.* **2013,** *42* (24), 9232-9242.
76. So, M. C.; Wiederrecht, G. P.; Mondloch, J. E.; Hupp, J. T.; Farha, O. K., Metal–organic framework materials for light-harvesting and energy transfer. *Chem. Commun.* **2015,** *51* (17), 3501-3510.
77. Park, K. S.; Ni, Z.; Côté, A. P.; Choi, J. Y.; Huang, R.; Uribe-Romo, F. J.; Chae, H. K.; O'Keeffe, M.; Yaghi, O. M., Exceptional chemical and thermal stability of zeolitic imidazolate frameworks. *Proceedings of the National Academy of Sciences* **2006,** *103* (27), 10186-10191.
78. Butler, K. T.; Hendon, C. H.; Walsh, A., Electronic Structure Modulation of Metal–Organic Frameworks for Hybrid Devices. *ACS Applied Materials & Interfaces* **2014,** *6* (24), 22044-22050.
79. Zahmakiran, M., Iridium nanoparticles stabilized by metal organic frameworks (IrNPs@ ZIF-8): synthesis, structural properties and catalytic performance. *Dalton Transactions* **2012,** *41* (41), 12690-12696.
80. Pan, Y.; Liu, Y.; Zeng, G.; Zhao, L.; Lai, Z., Rapid synthesis of zeolitic imidazolate framework-8 (ZIF-8) nanocrystals in an aqueous system. *Chem. Commun.* **2011,** *47* (7), 2071-2073.

81. Liang, K.; Ricco, R.; Doherty, C. M.; Styles, M. J.; Bell, S.; Kirby, N.; Mudie, S.; Haylock, D.; Hill, A. J.; Doonan, C. J., Biomimetic mineralization of metal-organic frameworks as protective coatings for biomacromolecules. *Nature communications* **2015,** *6*, 7240.
82. Hou, M.; Ge, J., Armoring Enzymes by Metal–Organic Frameworks by the Coprecipitation Method. In *Methods Enzymol.*, Elsevier: 2017; Vol. 590, pp 59-75.
83. Du, Y.; Gao, J.; Zhou, L.; Ma, L.; He, Y.; Huang, Z.; Jiang, Y., Enzyme nanocapsules armored by metal-organic frameworks: A novel approach for preparing nanobiocatalyst. *Chem. Eng. J.* **2017,** *327*, 1192-1197.
84. Chen, S.; Wen, L.; Svec, F.; Tan, T.; Lv, Y., Magnetic metal–organic frameworks as scaffolds for spatial co-location and positional assembly of multi-enzyme systems enabling enhanced cascade biocatalysis. *RSC Advances* **2017,** *7* (34), 21205-21213.
85. Li, Z.; Xia, H.; Li, S.; Pang, J.; Zhu, W.; Jiang, Y., In situ hybridization of enzymes and their metal–organic framework analogues with enhanced activity and stability by biomimetic mineralisation. *Nanoscale* **2017,** *9* (40), 15298-15302.
86. Lyu, F.; Zhang, Y.; Zare, R. N.; Ge, J.; Liu, Z., One-pot synthesis of protein-embedded metal–organic frameworks with enhanced biological activities. *Nano Lett.* **2014,** *14* (10), 5761-5765.
87. Zhang, Y.; Ge, J.; Liu, Z., Enhanced activity of immobilized or chemically modified enzymes. *ACS Catalysis* **2015,** *5* (8), 4503-4513.
88. Hiroma, S.; Kuroda, H.; Akamatu, H., Semiconductivity and photoconductivity of TCNQ crystal. *Bull. Chem. Soc. Jpn.* **1971,** *44* (4), 974-977.
89. Fadly, M.; El Gandoor, M.; Sawaby, A., Solid state properties and molecular structure of some divalentnd 10 cation-TCNQ salts. *Journal of materials science* **1992,** *27* (5), 1235-1239.
90. Abrahams, B. F.; Elliott, R. W.; Robson, R., Coordination Polymers Constructed from TCNQ2–Anions and Chelating Ligands. *Aust. J. Chem.* **2014,** *67* (12), 1871-1877.
91. Bonniface, D.; Braithwaite, M.; Eley, D.; Evans, R.; Pethig, R.; Willis, M., Factors affecting conduction in polymeric complex TCNQ salts. *Discussions of the Faraday Society* **1971,** *51*, 131-138.
92. Khoo, S. B.; Foley, J. K.; Pons, S., Electrolyte effects on the cyclic voltammetry of TCNQ and TCNE. *J. Electroanal. Chem.* **1986,** *215*, 273-285.
93. Zhang, X.; Saber, M. R.; Prosvirin, A. P.; Reibenspies, J. H.; Sun, L.; Ballesteros-Rivas, M.; Zhao, H.; Dunbar, K. R., Magnetic ordering in TCNQ-based metal–organic frameworks with host–guest interactions. *Inorganic Chemistry Frontiers* **2015,** *2* (10), 904-911.
94. Shoji, H.; Haruo, K.; Hideo, A., Polarized Absorption Spectra of Single Crystals of Ion Radical Salts. II. K(TCNQ) and Cs2(TCNQ)3. *Bull. Chem. Soc. Jpn.* **1971,** *44* (1), 9-15.
95. Odom, S. A.; Caruso, M. M.; Finke, A. D.; Prokup, A. M.; Ritchey, J. A.; Leonard, J. H.; White, S. R.; Sottos, N. R.; Moore, J. S., Restoration of Conductivity with TTF-TCNQ Charge-Transfer Salts. *Adv. Funct. Mater.* **2010,** *20* (11), 1721-1727.
96. Pauliukaite, R.; Malinauskas, A.; Zhylyak, G.; Spichiger-Keller, U. E., Conductive Organic Complex Salt TTF-TCNQ as a Mediator for Biosensors. An Overview. *Electroanalysis: An International Journal Devoted to Fundamental and Practical Aspects of Electroanalysis* **2007,** *19* (24), 2491-2498.
97. van de Wouw, H. L.; Chamorro, J.; Quintero, M.; Klausen, R. S., Opposites Attract: Organic Charge Transfer Salts. *J. Chem. Educ.* **2015,** *92* (12), 2134-2139.

98. Bennett, T. H.; Vaughn, M. D.; Davari, S. A.; Park, K.; Mukherjee, D.; Khomami, B., Jolly green MOF: confinement and photoactivation of photosystem I in a metal–organic framework. *Nanoscale Advances* **2019,** *1* (1), 94-104.
99. Fernandez, C. A.; Martin, P. C.; Schaef, T.; Bowden, M. E.; Thallapally, P. K.; Dang, L.; Xu, W.; Chen, X.; McGrail, B. P., An Electrically Switchable Metal-Organic Framework. *Scientific Reports* **2014,** *4*, 6114.
100. Jordan, P.; Fromme, P.; Witt, H. T.; Klukas, O.; Saenger, W.; Krauss, N., Three-dimensional structure of cyanobacterial photosystem I at 2.5 angstrom resolution. *Nature* **2001,** *411* (6840), 909-917.
101. LeBlanc, G.; Chen, G.; Gizzie, E. A.; Jennings, G. K.; Cliffel, D. E., Enhanced photocurrents of photosystem I films on p-doped silicon. *Adv Mater* **2012,** *24* (44), 5959-62.
102. Lee, I.; Lee, J. W.; Greenbaum, E., Biomolecular electronics: Vectorial arrays of photosynthetic reaction centers. *Phys. Rev. Lett.* **1997,** *79* (17), 3294-3297.
103. Stieger, K. R.; Feifel, S. C.; Lokstein, H.; Lisdat, F., Advanced unidirectional photocurrent generation via cytochrome c as reaction partner for directed assembly of photosystem I. *PCCP* **2014,** *16* (29), 15667-15674.
104. Talling, J. F.; Driver, D., Primary productivity measurements, marine and freshwater. Doty, M., Ed. ed.; Commission, U. A. E., Ed. Washington, DC, 1963; Vol. Vol. TID 7633.
105. Love, J. C.; Estroff, L. A.; Kriebel, J. K.; Nuzzo, R. G.; Whitesides, G. M., Self-Assembled Monolayers of Thiolates on Metals as a Form of Nanotechnology. *Chem. Rev.* **2005,** *105* (4), 1103-1170.
106. Kievit, O.; Brudvig, G. W., Direct electrochemistry of photosystem I. *J. Electroanal. Chem.* **2001,** *497* (1-2), 139-149.
107. Bird, C. L.; Kuhn, A. T., ELECTROCHEMISTRY OF THE VIOLOGENS. *Chem. Soc. Rev.* **1981,** *10* (1), 49-82.
108. Kozi Asada, C. N., Ulrich Heber and Ulrich Schreiber, Methyl Viologen-Dependent Cyclic Electron Transport in Spinach Chloroplasts in the Absence of Oxygen. *Plant Cell Physiol* **1990,** *31* (4), 557-564.
109. Hill, L. M. a. E. S., The Viologen Indicators. *Journal of General Physiology* **1933,** *16* (6), 859-873.
110. Nanni, E. J.; Angelis, C. T.; Dickson, J.; Sawyer, D. T., Oxygen activation by radical coupling between superoxide ion and reduced methyl viologen. *J. Am. Chem. Soc.* **1981,** *103* (14), 4268-4270.
111. Ebbesen, T. W.; Levey, G.; Patterson, L. K., Photoreduction of methyl viologen in aqueous neutral solution without additives. *Nature* **1982,** *298* (5874), 545-548.
112. Fromme, P.; Witt, H. T., Improved isolation and crystallization of photosystem I for structural analysis. *Biochimica et Biophysica Acta (BBA)-Bioenergetics* **1998,** *1365* (1-2), 175-184.
113. Porra, R.; Thompson, W.; Kriedemann, P., Determination of accurate extinction four different solvents; verification of the concentration of chlorophyll standards by atomic absorption spectroscopy. *Biochimica et Biophysica Acta-Bioenergetics* **1989,** *975,* 384-394.
114. Davari, S. A.; Hu, S.; Mukherjee, D., Calibration-free quantitative analysis of elemental ratios in intermetallic nanoalloys and nanocomposites using Laser Induced Breakdown Spectroscopy (LIBS). *Talanta* **2017,** *164*, 330-340.

115. Davari, S. A.; Hu, S.; Ribeiro, E. L.; Mukherjee, D., Rapid elemental composition analysis of intermetallic ternary nanoalloys using calibration-free quantitative Laser Induced Breakdown Spectroscopy (LIBS). *Mrs Advances* **2017,** *2* (55), 3371-3376.
116. Hu, S.; Ribeiro, E. L.; Davari, S. A.; Tian, M. K.; Mukherjee, D.; Khomami, B., Hybrid nanocomposites of nanostructured Co3O4 interfaced with reduced/nitrogen-doped graphene oxides for selective improvements in electrocatalytic and/or supercapacitive properties. *Rsc Advances* **2017,** *7* (53), 33166-33176.
117. Davari, S. A.; Hu, S.; Pamu, R.; Mukherjee, D., Calibration-free quantitative analysis of thin-film oxide layers in semiconductors using laser induced breakdown spectroscopy (LIBS). *J Anal Atom Spectrom* **2017,** *32* (7), 1378-1387.
118. Davari, S. A.; Masjedi, S.; Ferdous, Z.; Mukherjee, D., In-vitro analysis of early calcification in aortic valvular interstitial cells using Laser-Induced Breakdown Spectroscopy (LIBS). *J Biophotonics* **2018,** *11* (1).
119. Liang, K.; Ricco, R.; Doherty, C. M.; Styles, M. J.; Bell, S.; Kirby, N.; Mudie, S.; Haylock, D.; Hill, A. J.; Doonan, C. J.; Falcaro, P., Biomimetic mineralization of metal-organic frameworks as protective coatings for biomacromolecules. *Nature Communications* **2015,** *6*, 7240.
120. Davari, S. A.; Masjedi, S.; Ferdous, Z.; Mukherjee, D., Back Cover: In-vitro analysis of early calcification in aortic valvular interstitial cells using Laser-Induced Breakdown Spectroscopy (LIBS)(J. Biophotonics 1/2018). *J Biophotonics* **2018,** *11* (1).
121. Kramida, A., Ralchenko, Yu., Reader, J. and NIST ASD Team NIST Atomic Spectra Database (version 5.3). http://physics.nist.gov/asd
122. Mukherjee, D.; Cheng, M. D., Characterization of carbon-containing aerosolized drugs using laser-induced breakdown spectroscopy. *Applied Spectroscopy* **2008,** *62* (5), 554-562.
123. Mukherjee, D.; Cheng, M. D., Quantitative analysis of carbonaceous aerosols using laser-induced breakdown spectroscopy: a study on mass loading induced plasma matrix effects. *Journal of Analytical Atomic Spectrometry* **2008,** *23* (1), 119-128.
124. Mukherjee, D.; Rai, A.; Zachariah, M. R., Quantitative laser-induced breakdown spectroscopy for aerosols via internal calibration: Application to the oxidative coating of aluminum nanoparticles. *Journal of Aerosol Science* **2006,** *37* (6), 677-695.
125. Yin, Y.; Gao, C.; Xiao, Q.; Lin, G.; Lin, Z.; Cai, Z.; Yang, H., Protein-Metal Organic Framework Hybrid Composites with Intrinsic Peroxidase-like Activity as a Colorimetric Biosensing Platform. *ACS Applied Materials & Interfaces* **2016,** *8* (42), 29052-29061.
126. Liang, K.; Coghlan, C. J.; Bell, S. G.; Doonan, C.; Falcaro, P., Enzyme encapsulation in zeolitic imidazolate frameworks: a comparison between controlled co-precipitation and biomimetic mineralisation. *Chem. Commun.* **2016,** *52* (3), 473-476.
127. Shieh, F.-K.; Wang, S.-C.; Yen, C.-I.; Wu, C.-C.; Dutta, S.; Chou, L.-Y.; Morabito, J. V.; Hu, P.; Hsu, M.-H.; Wu, K. C.-W., Imparting functionality to biocatalysts via embedding enzymes into nanoporous materials by a de novo approach: size-selective sheltering of catalase in metal–organic framework microcrystals. *J. Am. Chem. Soc.* **2015,** *137* (13), 4276-4279.
128. Zhang, K.; Lively, R. P.; Zhang, C.; Koros, W. J.; Chance, R. R., Investigating the intrinsic ethanol/water separation capability of ZIF-8: an adsorption and diffusion study. *The Journal of Physical Chemistry C* **2013,** *117* (14), 7214-7225.
129. Niroomand, H.; Mukherjee, D.; Khomami, B., Tuning the photoexcitation response of cyanobacterial Photosystem I via reconstitution into Proteoliposomes. *Scientific Reports* **2017,** *7* (1), 2492.

130. Sun, C.-Y.; Qin, C.; Wang, X.-L.; Yang, G.-S.; Shao, K.-Z.; Lan, Y.-Q.; Su, Z.-M.; Huang, P.; Wang, C.-G.; Wang, E.-B., Zeolitic imidazolate framework-8 as efficient pH-sensitive drug delivery vehicle. *Dalton Transactions* **2012,** *41* (23), 6906-6909.
131. Dolgopolova, E. A.; Moore, T. M.; Ejegbavwo, O. A.; Pellechia, P. J.; Smith, M. D.; Shustova, N. B., A metal–organic framework as a flask: photophysics of confined chromophores with a benzylidene imidazolinone core. *Chem. Commun.* **2017,** *53* (53), 7361-7364.
132. Dolgopolova, E.; Moore, T.; Fellows, W.; Smith, M.; Shustova, N., Photophysics of GFP-related chromophores imposed by a scaffold design. *Dalton Transactions* **2016,** *45* (24), 9884-9891.
133. Williams, D. E.; Dolgopolova, E. A.; Pellechia, P. J.; Palukoshka, A.; Wilson, T. J.; Tan, R.; Maier, J. M.; Greytak, A. B.; Smith, M. D.; Krause, J. A., Mimic of the green fluorescent protein β-barrel: photophysics and dynamics of confined chromophores defined by a rigid porous scaffold. *J. Am. Chem. Soc.* **2015,** *137* (6), 2223-2226.
134. Petrova, A. A.; Boskhomdzhieva, B. K.; Milanovsky, G. E.; Koksharova, O. A.; Mamedov, M. D.; Cherepanov, D. A.; Semenov, A. Y., Interaction of various types of photosystem I complexes with exogenous electron acceptors. *Photosynth. Res.* **2017,** *133* (1-3), 175-184.
135. Makita, H.; Hastings, G., Modeling electron transfer in photosystem I. *Biochimica et Biophysica Acta (BBA)-Bioenergetics* **2016,** *1857* (6), 723-733.
136. Weng, Y.; Qiu, S.; Ma, L.; Liu, Q.; Ding, M.; Zhang, Q.; Zhang, Q.; Wang, T., Jet-fuel range hydrocarbons from biomass-derived sorbitol over Ni-HZSM-5/SBA-15 catalyst. *Catalysts* **2015,** *5* (4), 2147-2160.
137. Zhang, K.; Lively, R. P.; Zhang, C.; Chance, R. R.; Koros, W. J.; Sholl, D. S.; Nair, S., Exploring the framework hydrophobicity and flexibility of ZIF-8: from biofuel recovery to hydrocarbon separations. *The Journal of Physical Chemistry Letters* **2013,** *4* (21), 3618-3622.
138. Fairen-Jimenez, D.; Moggach, S.; Wharmby, M.; Wright, P.; Parsons, S.; Duren, T., Opening the gate: framework flexibility in ZIF-8 explored by experiments and simulations. *J. Am. Chem. Soc.* **2011,** *133* (23), 8900-8902.
139. Fan, X.; Wang, W.; Li, W.; Zhou, J.; Wang, B.; Zheng, J.; Li, X., Highly porous ZIF-8 nanocrystals prepared by a surfactant mediated method in aqueous solution with enhanced adsorption kinetics. *ACS Applied Materials & Interfaces* **2014,** *6* (17), 14994-14999.
140. Cherubin, A.; Destefanis, L.; Bovi, M.; Perozeni, F.; Bargigia, I.; de la Cruz Valbuena, G.; D'Andrea, C.; Romeo, A.; Ballottari, M.; Perduca, M., Encapsulation of Photosystem I in Organic Microparticles Increases Its Photochemical Activity and Stability for Ex Vivo Photocatalysis. *ACS Sustainable Chemistry & Engineering* **2019**.
141. Niroomand, H.; Pamu, R.; Mukherjee, D.; Khomami, B., Microenvironment alterations enhance photocurrents from photosystem I confined in supported lipid bilayers. *Journal of Materials Chemistry A* **2018,** *6* (26), 12281-12290.
142. Niroomand, H.; Mukherjee, D.; Khomami, B., Tuning the photoexcitation response of cyanobacterial Photosystem I via reconstitution into Proteoliposomes. *Scientific Reports* **2017,** *7*.
143. Melby, L.; Harder, R.; Hertler, W.; Mahler, W.; Benson, R.; Mochel, W., Substituted quinodimethans. II. Anion-radical derivatives and complexes of 7, 7, 8, 8-tetracyanoquinodimethan. *J. Am. Chem. Soc.* **1962,** *84* (17), 3374-3387.
144. Davari, S. A.; Taylor, P. A.; Standley, R. W.; Mukherjee, D., Detection of interstitial oxygen contents in Czochralski grown silicon crystals using internal calibration in laser-induced breakdown spectroscopy (LIBS). *Talanta* **2019,** *193*, 192-198.

145. Ji, Z.; Dong, H.; Liu, M.; Hu, W., Water-controlled synthesis of low-dimensional molecular crystals and the fabrication of a new water and moisture indicator. *Nano Research* **2009,** *2* (11), 857.
146. Nešprek, S.; Kalvoda, L.; Machová, L.; Pfleger, J.; Stevens, G., Two conductive phases of 1, 3-dimethylimidazolium-(TCNQ) 2 complex salt. *Synth. Met.* **1996,** *82* (2), 133-140.
147. Šorm, M.; Nešpůrek, S., The chemical stability of TCNQ-. anion radical salts containing a low-molecular weight and polymer cation. *Acta Polym.* **1985,** *36* (8), 433-439.
148. Oshima, R.; Kumanotani, J., Conducting polypeptide: Poly (l-histidinium 7, 7, 8, 8-tetracyanoquinodimethanide). *J. Polym. Sci., Part A: Polym. Chem.* **1987,** *25* (9), 2343-2350.
149. Wooster, T. J.; Bond, A. M., Ion selectivity obtained under voltammetric conditions when a TCNQ chemically modified electrode is presented with aqueous solutions containing tetraalkylammonium cations. *Analyst* **2003,** *128* (11), 1386-1390.
150. Harris, A. R.; Neufeld, A. K.; O'Mullane, A. P.; Bond, A. M., Characterisation of two distinctly different processes associated with the electrocrystallization of microcrystals of phase I CuTCNQ (TCNQ= 7, 7, 8, 8-tetracyanoquinodimethane). *J. Mater. Chem.* **2006,** *16* (45), 4397-4406.
151. Nafady, A.; Bond, A. M., Redox-Induced Solid− Solid Phase Transformation of TCNQ Microcrystals into Semiconducting Ni [TCNQ] 2 (H2O) 2 Nanowire (Flowerlike) Architectures: A Combined Voltammetric, Spectroscopic, and Microscopic Study. *Inorg. Chem.* **2007,** *46* (10), 4128-4137.
152. Nafady, A.; Bond, A. M.; Bilyk, A.; Harris, A. R.; Bhatt, A. I.; O'Mullane, A. P.; De Marco, R., Tuning the electrocrystallization parameters of semiconducting Co [TCNQ] 2-based materials to yield either single nanowires or crystalline thin films. *J. Am. Chem. Soc.* **2007,** *129* (8), 2369-2382.

APPENDIX

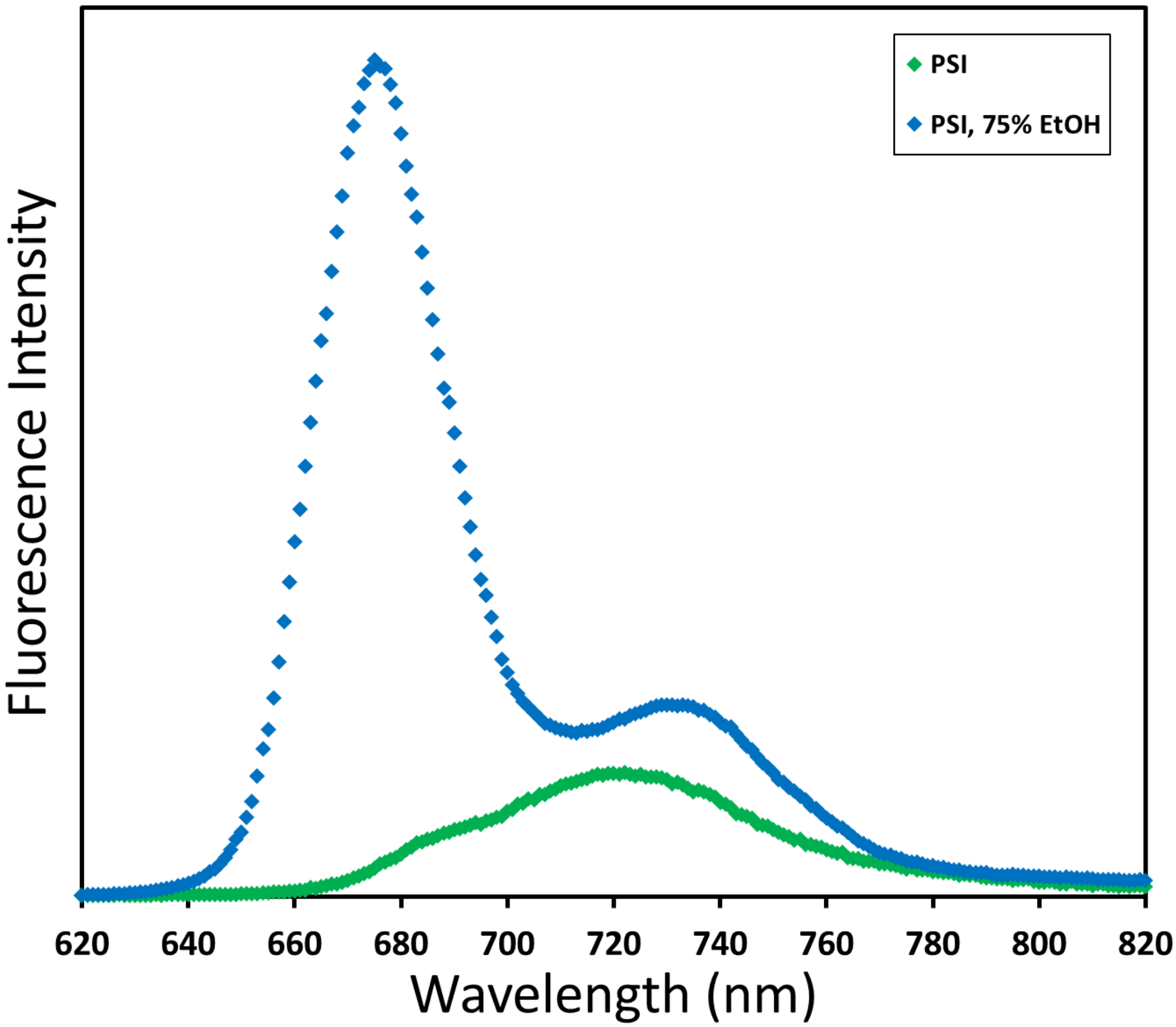

Figure 3.S1. Room temperature fluorescence emission (excitation 440 nm) of PSI in water and PSI denatured in 75% ethanol. The peak shifts from 720 nm (green) to 675 nm (blue).

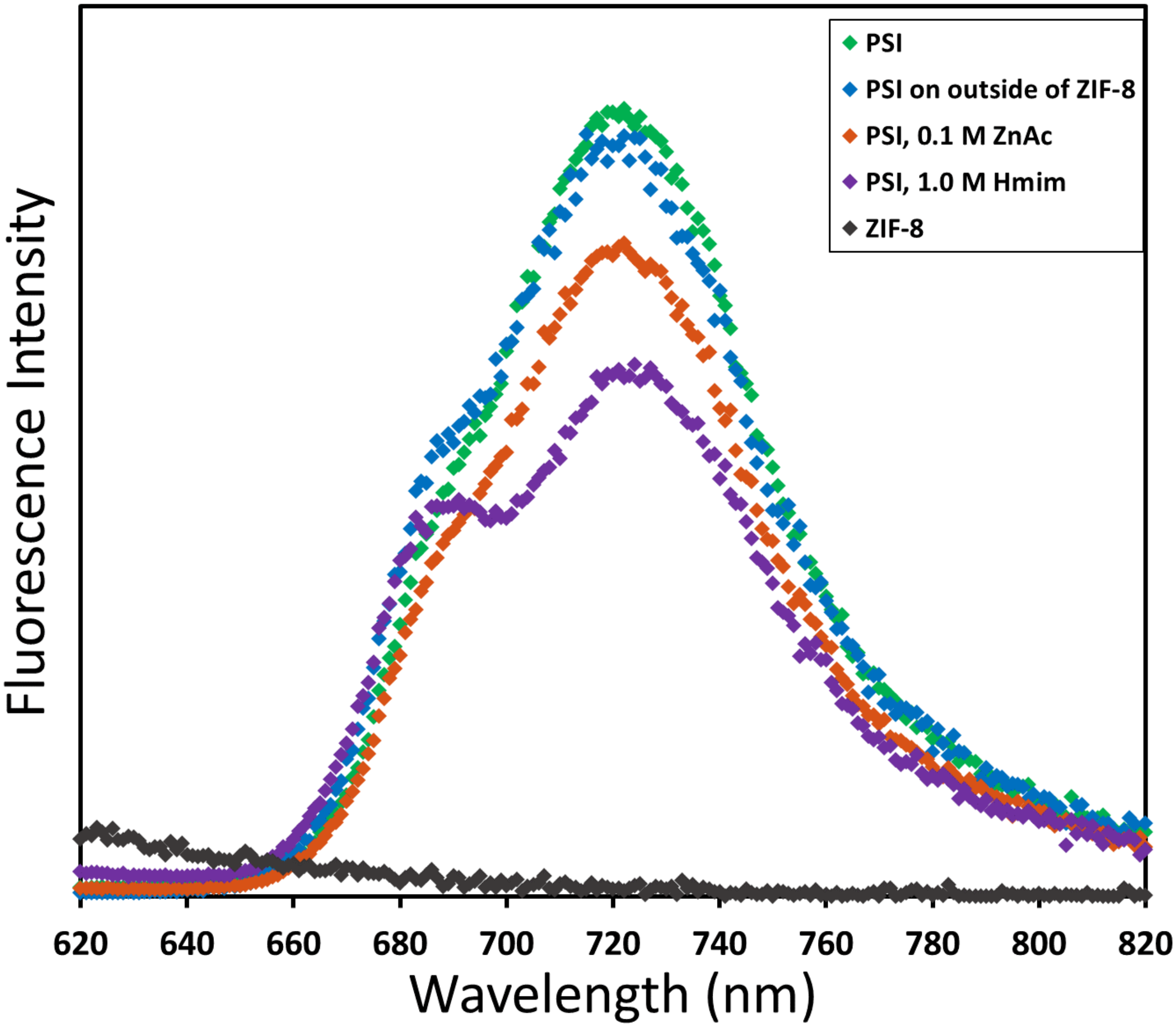

Figure 3.S2. Room temperature fluorescence emission (excitation 440 nm) of various PSI and ZIF-8 samples. ZIF-8 alone (black) has no emission, and PSI bound to ZIF-8 surface (blue) has no shift in emission. PSI in either zinc acetate (orange) or 2-methylimidazole (purple) alone show minor decreases in fluorescence, and the shoulder appearance is due to the high pH of Hmim solution.

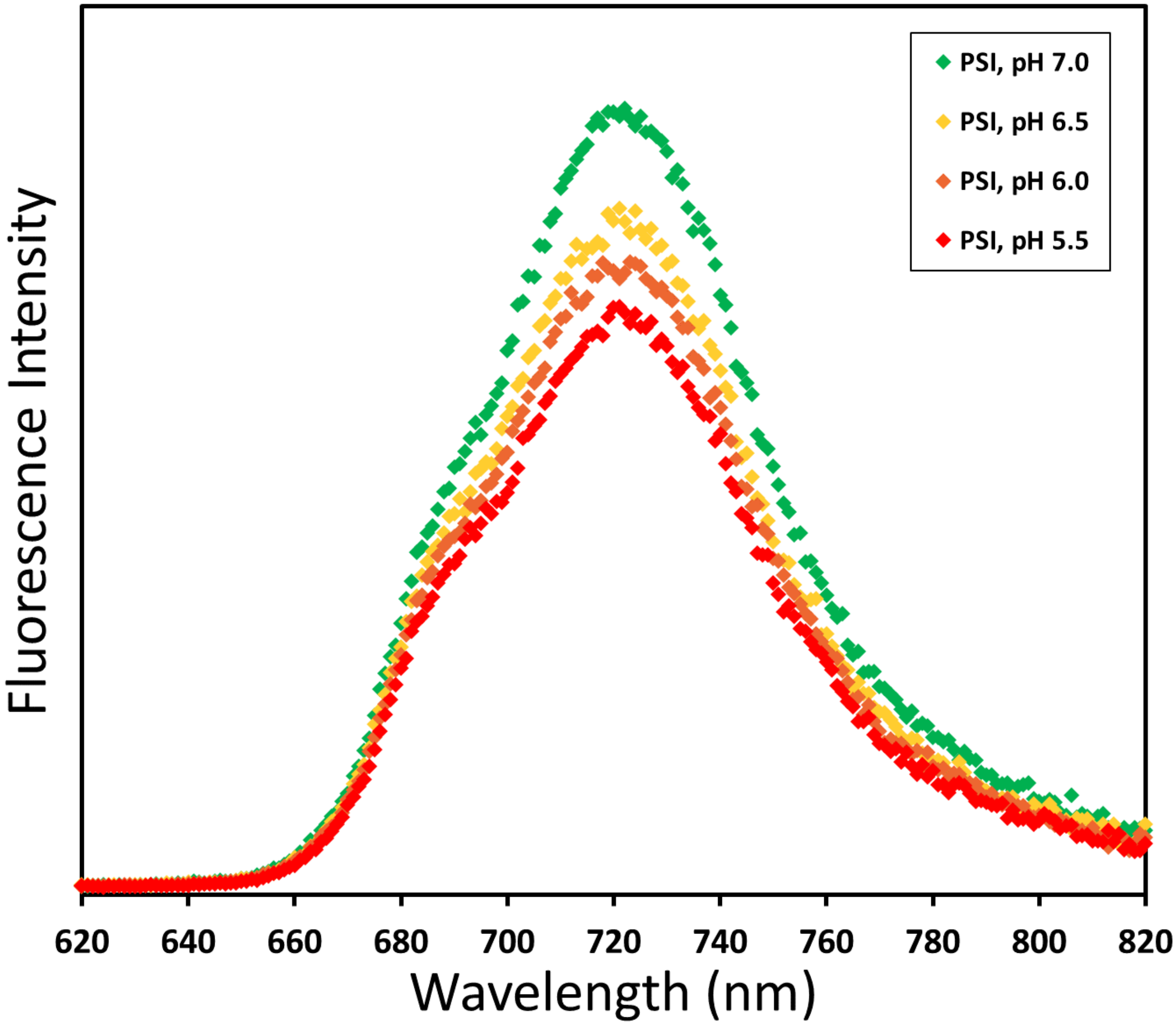

Figure 3.S3. Room temperature fluorescence emission (excitation 440 nm) of PSI in increasingly acidic conditions. The presence of acid does not shift the emission peak, but decreases intensity as the magnesium ions are dechelated from chlorophyll.

Table 3.S1. The characteristic decay times for PSI and PSI@ZIF-8 in the presence of various mediators.

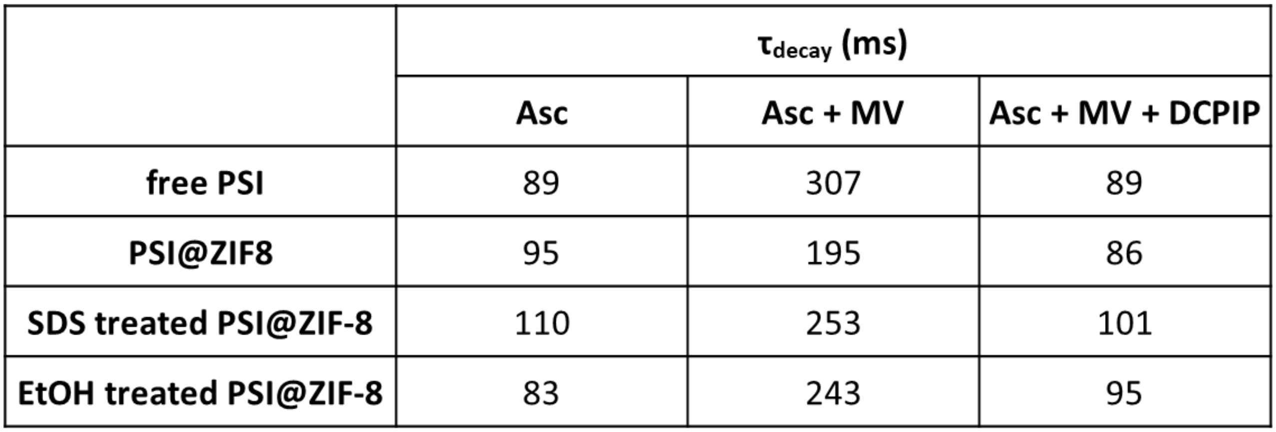

	τ_{decay} (ms)		
	Asc	**Asc + MV**	**Asc + MV + DCPIP**
free PSI	89	307	89
PSI@ZIF8	95	195	86
SDS treated PSI@ZIF-8	110	253	101
EtOH treated PSI@ZIF-8	83	243	95

VITA

Tyler Hamilton Bennett was born in Richmond, VA in 1989 to Martin Bennett and Sharon Madere. In 2011, he received his Bachelor of Science degree in Chemical Engineering from the University of South Carolina. Later, he attended the University of Tennessee, Department of Chemical and Biomolecular Engineering to join Prof. Bamin Khomami’s research group in 2012 to pursue his doctoral degree. His doctoral research has mainly focused on investigations of Photosystem I towards the ultimate end of deepening fundamental understanding of chemical and electrochemical processes and exploring creative avenues towards biohybrid photovoltaic devices.